LUND UNIVERSITY

Induction heating of carbon fibre reinforced polymer composites

Characterization and modelling

Lundström, Fredrik

2022

Induction heating of carbon fibre reinforced polymer composites

Characterization and modelling

FREDRIK LUNDSTRÖM
DIVISION OF PRODUCTION AND MATERIALS ENGINEERING | LUND UNIVERSITY

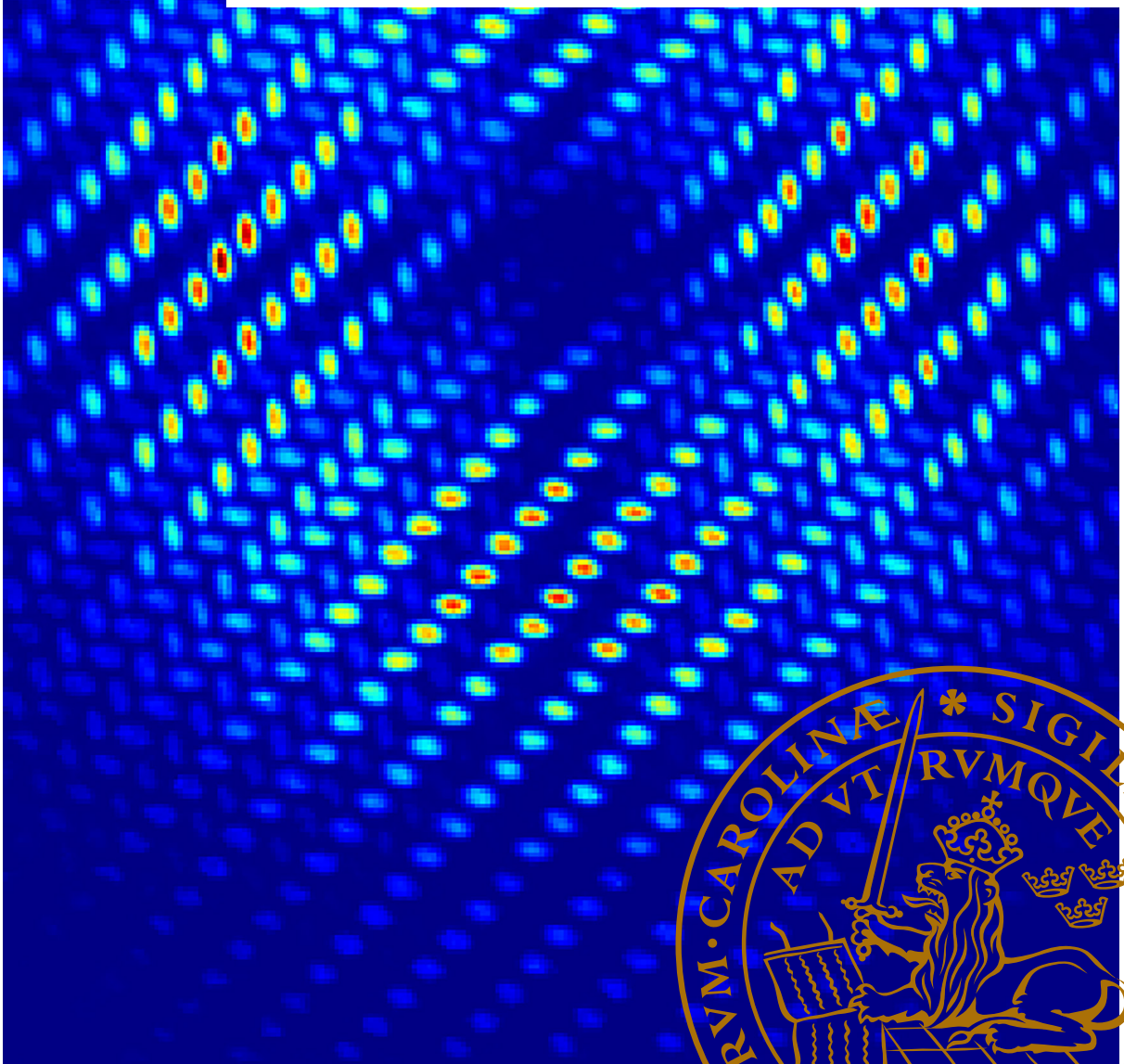

Induction heating of carbon fibre reinforced polymer composites

Induction heating of carbon fibre reinforced polymer composites

Characterization and modelling

Fredrik Lundström

LUND
UNIVERSITY

DOCTORAL DISSERTATION

by due permission of the Faculty of Engineering, Lund University, Sweden.
To be defended at lecture hall KC:A, Kemicentrum, LTH, Naturvetarvägen 14,
Lund. 2022-04-29 at 10:15.

Faculty opponent
Professor Malin Åkermo

KTH Royal Institute of Technology, Stockholm, Sweden

Organization Division of Production and Materials Engineering Faculty of Engineering LUND UNIVERSITY	**Document name** DOCTORAL DISSERTATION
	Date of issue 2022-04-29
Author Fredrik Lundström	Sponsoring organizations: VINNOVA, MISTRA, SSF

Title and subtitle

Induction heating of carbon fibre reinforced polymer composites - Characterization and modelling

Abstract

Carbon fibre reinforced polymers (CFRP) are lightweight materials with great potential due to their high strength and stiffness relative to their weight. This enables weight reduction in, for example, vehicles, which is important in reducing energy consumption. Their high strength and stiffness along the fibre direction also enable the development of new types of construction parts. The manufacturing of thermoset-based CFRP is often a time-consuming process with relatively low energy efficiency. Common manufacturing methods such as resin transfer moulding, compression moulding, and autoclaving use significantly more energy than is needed to cure the CFRP part. This is because the heat is transferred conductively via the part surface from a tool with a large mass. However, other potential heating methods are available. Due to the electrical conductivity of carbon fibres, it is possible to use induction heating. This means that the heat is generated directly within the CFRP part without the need to heat a tool with a large thermal mass. The idea of using this technique to heat CFRP is not new, but the anisotropy of the material means that it is associated with a higher level of complexity than the induction heating of metals.

To make the heat and temperature distribution more predictable, there is a need for better models and knowledge of how the heat is generated and how the temperature is distributed within CFRP during induction heating. In this thesis, different CFRP configurations were characterized and modelled to provide knowledge and methods for predicting the induction heating behaviour of CFRP. The development of the models has resulted in temperature prediction tools, useful for a wide range of fibre volume fractions, and for both woven and cross-ply layups. Methods for characterization of thermal and electrical input parameters to the models were identified and developed. The temperature distributions predicted by the models were proven to be valid.

Keywords: Carbon fibre reinforced polymers, Induction heating, Material characterization, Thermal properties, Electrical conductivity, Numerical modelling

Classification system and/or index terms (if any)

Supplementary bibliographical information		**Language** English
ISSN and key title		ISBN 978-91-8039-199-3 (print) ISBN 978-91-8039-200-6 (pdf)
Recipient's notes	**Number of pages** 150	Price
	Security classification	

Induction heating of carbon fibre reinforced polymer composites

Characterization and modelling

Fredrik Lundström

LUND
UNIVERSITY

Cover: thermal image by Fredrik Lundström

Faculty of Engineering
Department of Mechanical Engineering Sciences
Division of Production and Materials Engineering

ISBN 978-91-8039-199-3 (print)
ISBN 978-91-8039-200-6 (pdf)

Printed in Sweden by Media-Tryck, Lund University
Lund 2022

Acknowledgements

First and foremost I would like to thank my supervisors Mats Andersson and Kenneth Frogner for their guidance and great support during this work.

The work presented in this thesis was carried out at the Division of Production and Materials Engineering at Lund University. The work was primarily carried out within the Sustainable Production Initiative (SPI), financed by VINNOVA.

The work was also partly carried out within the projects EUREKA project E!11717 TOOLS, and LIGHTest, both financed by VINNOVA. Initial financial support was also received from The Swedish Foundation for Strategic Environmental Research (MISTRA) and the Swedish Foundation for Strategic Research (SSF).

Further, I would like to thank Corebon AB for their support and assistance during experiments and measurements.

Finally, I would like to give a special thanks to my family for their support and encouragement.

Abstract

Carbon fibre reinforced polymers (CFRP) are lightweight materials with great potential due to their high strength and stiffness relative to their weight. This enables weight reduction in, for example, vehicles, which is important in reducing energy consumption. Their high strength and stiffness along the fibre direction also enable the development of new types of construction parts. The manufacturing of thermoset-based CFRP is often a time-consuming process with relatively low energy efficiency. Common manufacturing methods such as resin transfer moulding, compression moulding, and autoclaving use significantly more energy than is needed to cure the CFRP part. This is because the heat is transferred conductively via the part surface from a tool with a large mass. However, other potential heating methods are available. Due to the electrical conductivity of carbon fibres, it is possible to use induction heating. This means that the heat is generated directly within the CFRP part without the need to heat a tool with a large thermal mass. The idea of using this technique to heat CFRP is not new, but the anisotropy of the material means that it is associated with a higher level of complexity than the induction heating of metals.

To make the heat and temperature distribution more predictable, there is a need for better models and knowledge of how the heat is generated and how the temperature is distributed within CFRP during induction heating. In this thesis, different CFRP configurations were characterized and modelled to provide knowledge and methods for predicting the induction heating behaviour of CFRP. The development of the models has resulted in temperature prediction tools, useful for a wide range of fibre volume fractions, and for both woven and cross-ply layups. Methods for characterization of thermal and electrical input parameters to the models were identified and developed. The temperature distributions predicted by the models were proven to be valid.

Keywords:

Carbon fibre reinforced polymers, Induction heating, Material characterization, Thermal properties, Electrical conductivity, Numerical modelling

Populärvetenskaplig sammanfattning

Målet att uppnå ett hållbart samhälle är en stark drivkraft för teknisk utveckling. Till exempel är viktreduktion av elektriska fordon en betydelsefull åtgärd för att minska energianvändningen och därmed öka räckvidden. Kolfiberförstärkta plaster, CFRP (carbon fibre reinforced polymer), är en typ av kompositmaterial som är av stort intresse tack vara sin styrka och styvhet i förhållande till sin låga vikt. Kolfiberförstärkt plast består av kolfiberväv som infiltreras med en plastmatris som binder ihop materialet och härdas vid förhöjd temperatur. Idag är CFRP ett vanligt förekommande material i bland annat flygplan, sportbilar och sportutrustning men tillverkningsprocesserna är ofta tidskrävande och kräver mycket manuellt arbete. Sammantaget leder detta till relativt dyra detaljer vilket begränsar dess användning.

För tillverkning av härdplastbaserade CFRP-detaljer utnyttjas metalliska gjutverktyg med stor termisk massa i förhållande till kompositdetaljens massa, bland annat för att åstadkomma en jämn yttemperatur mot detaljen. Detta resulterar dock i långsamma uppvärmningsprocesser och hög energiförbrukning. Det är också vanligt att använda autoklav (ugn med förhöjt tryck) vid tillverkning av CFRP men även denna metod är långsam och energikrävande. För att sänka energiförbrukningen och minska tidsåtgången per detalj, och därmed reducera priset per detalj, krävs det utveckling av nya tillverkningsmetoder.

I stället för att värma upp CFRP-detaljen konduktivt via verktygsytan kan man generera värmen direkt i CFRP-detaljen och därmed undvika uppvärmning av stora verktyg eller ugnar. Detta kan dessutom medföra en jämnare temperaturprofil genom tjockleken. Det faktum att kolfiber är elektriskt ledande innebär att induktionsvärmning kan användas för att generera värmen direkt i detaljen, på samma sätt som med induktionsvärmning av metaller. Induktionsvärmning innebär att man skapar cirkulerande elektriska strömmar i materialet genom att applicera ett alternerande magnetfält. Magnetfältet skapas genom att driva en växelströmström genom en intilliggande spole. CFRP är ett anisotropt material vilket innebär att egenskaperna varierar lokalt inom geometrin och i olika riktningar. Detta innebär att utmaningarna med att applicera induktionsvärmning är betydande jämfört med induktionsvärmning av metaller. För att kunna inducera en cirkulerande ström i en CFRP-detalj krävs det i praktiken att detaljen är uppbyggd av flera fiberriktningar som har elektrisk kontakt med varandra. Den inducerade effektfördelningen, och därmed också temperaturfördelningen, är starkt beroende av faktorer såsom fiberriktningar, elektrisk kontakt mellan fiber och vävtjocklek.

För att kunna utveckla induktionsvärmningstekniken för kompositapplikationer, som till exempel härdning av CFRP detaljer, krävs det en bättre förståelse för hur värmen och temperaturen fördelar sig i materialet vid induktionsvärmning. Det huvudsakliga målet med denna avhandling är att karakterisera elektriska och termiska egenskaper i CFRP samt att utveckla simuleringsmodeller för att kunna förutse och förstå värmegenereringen och temperaturfördelningen i kolfiber vid induktionsvärmning. Arbetet har resulterat i ett antal modeller som bidrar med att öka förståelsen för induktionsvärmning av kolfiberkompositer. Detta kan leda till energieffektivare och snabbare tillverkningsprocesser samt reducerade kostnader.

Appended publications

Paper I — Towards energy efficient heating in industrial processes - Three steps to achieve maximized efficiency in an induction heating system
Siesing L, Lundström F, Frogner K, Cedell T, Andersson M
Procedia Manufacturing, 2018;25:404–411

Paper II — Induction heating of carbon fiber composites: Investigation of electrical and thermal properties
Lundström F, Frogner K, Wiberg O, Cedell T, Andersson M
International Journal of Applied Electromagnetics and Mechanics, 2017;53:S21–S30

Paper III — A numerical model to analyse the temperature distribution in cross-ply CFRP during induction heating
Lundström F, Frogner K, Andersson M
Composites Part B: Engineering, 2020;202:108419

Paper IV — Analysis of the temperature distribution in weave-based CFRP during induction heating using a simplified numerical model with a cross-ply representation
Lundström F, Frogner K, Andersson M
Composites Part B: Engineering, 2021;223:109153

Paper V — A method for inductive measurement of equivalent electrical conductivity in thin non-consolidated multilayer carbon fibre fabrics
Lundström F, Frogner K, Andersson M
Composites Part B: Engineering, 2018;140:204–213

Paper VI — Numerical modelling of CFRP induction heating using temperature-dependent material properties
Lundström F, Frogner K, Andersson M
Composites Part B: Engineering, 2021;220:108982

Paper VII — A resistor network model for analysis of current and temperature distribution in CFRP during induction heating
Lundström F, Frogner K, Andersson M
Submitted to Journal of Composite Materials, March 2022

The author's contributions

Paper I	Lundström wrote the paper jointly with the co-authors and conducted the experiments and modelling work.
Paper II	Lundström planned and wrote the paper. Lundström planned the experimental work jointly with the co-authors and conducted the experimental and modelling work.
Paper III	Lundström conceived the idea, planned and conducted the experimental work, developed the model, performed the simulations and analysis, and wrote the paper.
Paper IV	Lundström conceived the idea, planned and conducted the experimental work, developed the model, performed the simulations and analysis, and wrote the paper.
Paper V	Lundström planned and conducted the experimental work, developed the model, performed the simulations and analysis, and wrote the paper.
Paper VI	Lundström conceived the idea, planned and conducted the experimental work, developed the model, performed the simulations and analysis, and wrote the paper.
Paper VII	Lundström planned and conducted the experimental work, developed the model, performed the simulations and analysis, and wrote the paper.

List of symbols

This list presents the symbols used in this thesis. In some cases a symbol has multiple meanings, as indicated in the list, and in each case, the meaning is understood from the context. The meanings of symbols used in the appended publications are in some cases different from those presented here. This list does not present all the variable subscripts used. The meanings of the subscripts are presented continuously in the thesis. Bold symbols denote vector properties.

A	Area, m^2
$\mathbf{A}$	Magnetic vector potential, T·m
$\mathbf{B}$	Magnetic flux density vector, T
C	Capacitance, F
c_p	Specific heat capacity, J/(kg·K)
d	Thickness, m
$\mathbf{E}$	Electric field vector, V/m
E	Elastic modulus, N/m^2
F	Force, N
f	Frequency, Hz
$\mathbf{H}$	Magnetic field intensity vector, A/m
h	Convective heat transfer coefficient, $W/(m^2 \cdot K)$
I	Current, A
i	1. Imaginary unit
	2. Counter variable
$\mathbf{J}$	Current density vector, A/m^2
J	Current density, A/m^2
L	1. Fibre direction in a Cartesian coordinate system
	2. Inductance, H
l	Length, m
N	Discrete quantity, for example, the number of fabric plies in a CFRP plate
$\mathbf{n}$	Normal vector
P	Resistive power, W
Q	1. Heating power, W
	2. Heating power density, W/m^3

$\mathbf{q}$	Surface heat loss, W
R	1. Electrical resistance, Ω
	2. Radial in-plane fibre direction in a cylindrical coordinate system
T	1. Temperature, K
	2. Transverse in-plane fibre direction in a Cartesian coordinate system
T_g	Glass transition temperature, °C
t	Time, s
V	Voltage, V
w_{sizing}	Weight fraction of sizing in a fibre fabric
X	1. Reactance, Ω
	2. In-plane Cartesian direction x
Y	In-plane Cartesian direction y
Z	1. Impedance, Ω
	2. Through-plate thickness direction in a Cartesian coordinate system
α	Thermal diffusivity, m^2/s
Δ	Difference
δ	1. Skin depth, m
	2. Relative difference operator
	3. Phase lag between stress and strain in DMA measurements
ε	1. Emissivity
	2. Strain
η	Energy efficiency
λ	Thermal conductivity, W/(m·K)
μ	Magnetic permeability, H/m
μ_r	Relative magnetic permeability
μ_0	Magnetic permeability in vacuum, H/m
ρ	Density, kg/m^3
σ	1. Electrical conductivity, S/m
	2. Stefan–Boltzmann constant
τ	Approximation of temperature equalization time, s
ϕ	Fibre volume faction, either given as a fraction 0-1 or as a percentage.

Table of contents

1 Introduction

1.1 Background

The goal of achieving a sustainable society is a strong driving force in the development of lightweight materials and more efficient production methods. For example, weight reduction is an important parameter to increase the range of electric vehicles due to the limited energy storage capacity of their batteries. Carbon fibre reinforced polymers (CFRP) are lightweight composite materials of great interest due to their high strength and stiffness relative to their weight, but also due to the possibility of designing and producing advanced geometries with tailored properties to achieve high stiffness in certain directions. Today CFRP is common in sectors such as aerospace, sports cars, and sports equipment, but the required manufacturing processes are often highly energy-intensive, time-consuming, and labour intensive. This results in relatively expensive parts and limited usage.

Temperature control is important for CFRP manufacturing in general, especially during the curing of thermoset-based CFRP to achieve a fully cured matrix, minimize stress, and control the exothermic reactions. Resin transfer moulding, compression moulding, and autoclaving are examples of established CFRP production methods. Certain composite parts and materials can be processed at a constant tool temperature, but thermal cycling is usually necessary to obtain the required quality. Assuming the latter case, the usual issues related to these methods are their high energy and time consumption. To achieve a uniform and stable temperature profile during moulding, the tool often has a thermal mass significantly larger than that of the part to be manufactured. The heat is conductively transferred from the tool to the CFRP part. A typical curing process begins with a stepwise increase in the temperature. When the part is cured, the temperature needs to be decreased before demoulding to obtain a good surface appearance and avoid warpage. A slow temperature increase is often necessary to achieve a uniform temperature profile throughout the thickness of the CFRP part and to maintain a uniform temperature profile in the tool. Another issue related to the large thermal mass is that a significant part of the energy consumed by the manufacturing is used to increase the temperature of the tool mass; only a small fraction of the energy is absorbed by the curing CFRP part.

“Hot-in, hot-out” compression moulding, in which the temperature of the moulding tool remains constant throughout the process, has the potential to be very time efficient but still relies on large thermal masses to achieve uniform temperature distribution. The start-up time is often long, which can be a problem, especially for production of small batch sizes. In this method, it is common to cool down the CFRP part in an external fixture to avoid warpage, which adds an extra step to the process. In autoclaving, another manufacturing method, the part is placed in a vacuum bag, which is then placed in an autoclave oven. This is a very slow process with relatively high energy consumption.

Instead of heating the CFRP conductively via the surface, the heat could instead be generated volumetrically within the CFRP part using alternative methods. Properly implemented, this would significantly reduce the need for tools with a high thermal mass, significantly reduce cycle times, reduce energy consumption due to the reduced thermal mass, and potentially achieve a more uniform temperature distribution throughout the thickness, especially in thick-walled components, and thus more uniform curing. The reduced cycle times and energy consumption would in turn result in reduced cost per produced part.

Dielectric heating is one potential method that has been investigated by Lee and Springer[1], Thostenson and Chou [2] and Li et al. [3, 4], among others. Typically with a penetration depth; at 2.45 GHz a penetration depth of 2 mm in unidirectional CFRP, observed by Kwak et al. [5]. The main challenge would be to integrate this technique into a press tool and to achieve uniform heating. Ultrasonic heating is another heating method, but it is limited in scale and is best suited for local heating, for example, in joining applications. The electrical conductivity of carbon fibres also enables resistive heating by driving current through the material, as investigated by Kim et al. [6] and Athanasopoulos et al. [7, 8]. However, instead of connecting electrodes to the CFRP, which works only for simple geometries, it could be heated by inducing currents in the fibres, as investigated and analysed by, for example, Miller et al. [9], Fink et al. [10], and Yarlagadda et al. [11].

Today, induction heating is a well-established technique for heating metals. Heat treatment of metals [12, 13] and domestic cooktops, [14, 15] are examples of common applications of induction heating. The heat is generated directly inside the object, enabling high heating efficiency and rapid temperature increase. Figure 1.1 depicts the current density distribution during the induction heating of a copper plate. Also, the induction heating of CFRP could significantly reduce cycle times, which would be valuable in, for example, the continuous manufacturing of CFRP, in which the heat conduction time may be a bottleneck. The idea of using this technique to heat CFRP is not new, but the anisotropy of the material means that it is associated with a higher

level of complexity than the induction heating of metals. For example, the formation of circulating currents is very much dependent on the electrical contact between different fibre directions and, as observed and modelled by Yu et al. [16], the resistivity in different directions is a function of various micromechanical properties such as waviness and applied pressure. An overview of different applications is presented by Bayerl et al. [17]. One example of an existing application is welding and melting of thermoplastic-based CFRP parts as investigated by Rudolf et al. [18], Becker et al. [19-21], Grouve et al. [22, 23], and Moser [24]. Other examples of applications are post-curing of thermoset parts as investigated by Bettelli [25] and curing of thermoset adhesives as investigated by Frauenhofer et al. [26]. The low electrical conductivity of CFRP relative to metals, and the fact that CFRP is non-magnetic, allows for a large skin depth, which permits volumetric heating throughout the thickness, in contrast to magnetic steel, in which the skin depth is extremely small. Nevertheless, the introduction of induction heating entails new challenges. The anisotropy of CFRP makes the prediction of local current paths and temperature distribution patterns a significant challenge. Therefore, knowledge and simulation tools for the prediction of the current and temperature distribution will be central to developing induction heating technology in the field of carbon fibre composites.

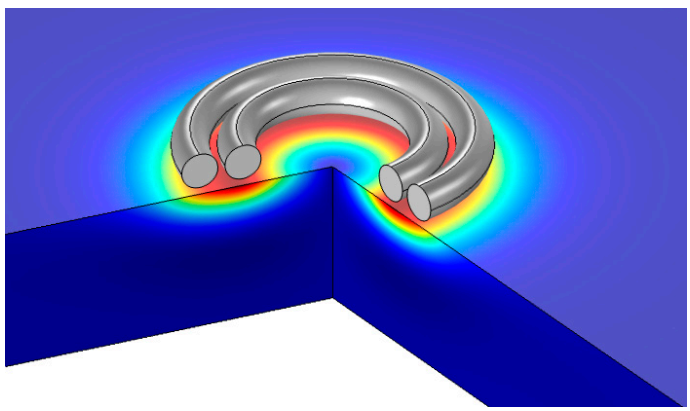

Figure 1.1. As an illustration of the induction heating technique, this figure shows a cutaway illustration of the current density distribution induced in a 20 mm thick copper plate. The coil has two turns and is made of solid copper wire with a diameter of 5 mm. The excitation frequency of the current is 300 Hz. Reprinted from Comsol Multiphysics [27].

1.2 Objectives

Developing the technique and applications for induction heating of CFRP requires a better understanding of the induced power distribution and of the material parameters that influence induction heating. This is formulated in objectives 1–3, below. From a longer-term perspective, beyond the scope of this work, the goal is to implement direct induction heating of CFRP in industrial processes. Therefore, objective 4 is formulated to evaluate the future potential of the technique and to highlight technical challenges.

Objective 1: Explain how different composite configurations such as fibre type, layup, weave type, and fibre volume fraction affect the induced heating distribution and temperature distribution during induction heating of CFRP.

Objective 2: Develop and experimentally validate simulation models for predicting the induced power distribution and temperature distribution during the induction heating of CFRP. The goal is to strive for a high level of simplification of the representation of the composite, i.e. different levels of macroscopic representation of the microscopic structure.

Objective 3: Identify and develop methods for characterizing the electrical and thermal properties required as inputs to simulation models. Analyse the properties concerning variations in the composite configuration to explain the connection between induction heating behaviour and the composite parameters.

Objective 4: Evaluate induction heating as a possible processing method for CFRP and identify related problems and challenges.

1.3 Scope and limitations

The focus of this work is on development of models for prediction of temperature distribution in CFRP during induction heating for the purpose to understand the heating mechanisms. The characterization of materials is limited to electrical and thermal properties to be used in the models. Coil geometries are limited to axisymmetric configurations. The study is limited to continuous PAN fibres arranged in bidirectional fibre layups. The investigation includes dry fibre stacks and CFRP composites with epoxy matrix. The development of the induction heating system a such is not covered.

1.4 Methodology

This work comprises model development, the characterization of input parameters, and finally a comparison between simulated and measured temperature distributions. The work has been an iterative process, alternating between characterization and modelling, to analyse the induction heating behaviour of CFRP and to enable prediction of the induced power distribution and the temperature distribution. The methodology for the work presented in chapter 3-5, which constitutes the main part of this thesis, can be divided into the three steps presented in the bullet list below. Details of the technical methods are presented in chapter 4.

- Modelling and simulation
- Characterization of thermal and electrical properties
- Evaluation of the simulation results by means of thermographic measurements

1.5 Contributions of the appended publications

In the list of appended publications, the papers are arranged in a logical order with respect to their contributions to the thesis, rather than by their publication dates. Paper I [28] mainly serves as background to the design of the coil setup. Paper II [29] serves as a pre-study of how different fibre and composite properties affect the induction heating behaviour. The work presented in the subsequent studies was designed and conducted based on the knowledge gained from the study presented in Paper II. Paper III and IV presents how induction heating of cross-ply and woven CFRP can be simulated using a 3D FEM model. Then a higher level of simplification is introduced in Paper V and VI, by using an 2D-axisymmetric representation in a FEM model. Paper VII uses a combination of 2D and 3D modelling in order to achieve an intuitive and effective simulation model for prediction of heat generation and temperature on tow size level. The modelling and characterization chapters 3, 4 and 5 are based mainly on the work presented in Paper III [30], Paper IV [31], Paper V [32], Paper VI [33], and Paper VII.

2 Theory

2.1 Carbon fibre reinforced polymers

Carbon fibre reinforced polymers (CFRP) are composite materials consisting of carbon fibres as the reinforcing material and a polymer, either thermoset or thermoplastic, as the matrix material. CFRP composites are known for their high strength and stiffness relative to their weight. A large variety of carbon fibres exist with a wide range of mechanical, thermal, and electrical properties. The carbon fibre filaments are produced from a precursor material, for example, polyacrylonitrile (PAN), rayon, or mesophase pitch. PAN is the most common such material, while fibres based on mesophase pitch are typically more expensive but with very high stiffness. Mesophase pitch fibres are known for their high electrical conductivity and high thermal conductivity compared with PAN fibres. Carbon fibres are available both as continuous fibre bundles (tows) or short fibres. Continuous fibres are available on bobbins as is, in different weave configurations, multiaxial fabrics, or as unidirectional plies (UD). Carbon fibres are also available pre-impregnated with the polymer matrix, denoted "pre-preg".

2.2 CFRP manufacturing methods

There are various methods for producing CFRP that can be categorized into discrete and continuous manufacturing methods. The work presented here deals only with varieties of discrete, or sometimes called batch manufacturing methods, which are briefly described below:

Resin transfer moulding (RTM): The dry fibres are placed in a closed mould; liquid polymer is forced into the mould by atmospheric or elevated pressure and then cured. This requires a resin with very low viscosity, so this method is only suited for low-viscous thermosets, and not thermoplastics. Before injecting the matrix material, the air is evacuated from the cavity to improve the infiltration process. In the work presented in this thesis, the resin transfer moulding process was always vacuum assisted and elevated pressure (7 bar) was used to achieve good infusion of the resin

into the fibre structure. Figure 2.1 presents a schematic illustration of a resin transfer moulding tool.

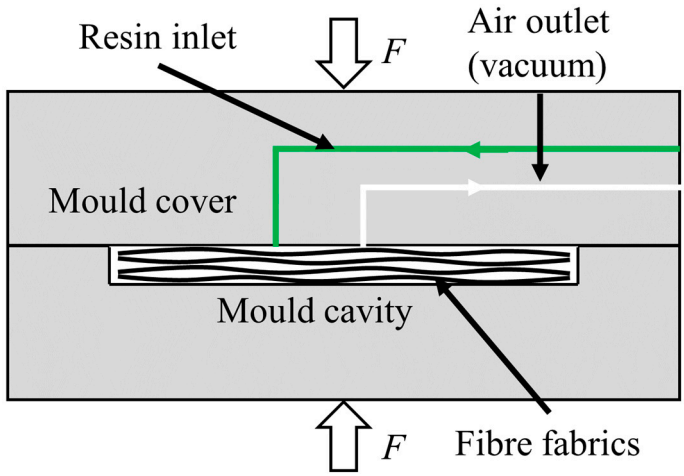

Figure 2.1. Schematic illustration of resin-transfer moulding for CFRP manufacturing.

Compression moulding: First the moulding materials, both fibres and matrix material, are placed in the mould cavity. Pressure is then applied and the temperature is controlled in order to cure the material. This method is typically used for curing pre-impregnated carbon fibre fabrics, denoted "pre-preg". A thermoset-based pre-preg is partially cured during manufacturing in order to simplify the handling. A variant of the method is "hot-in, hot-out"-compression moulding in which the tool is already preheated when the material is placed in the cavity. Figure 2.2 shows a schematic illustration of a compression moulding tool.

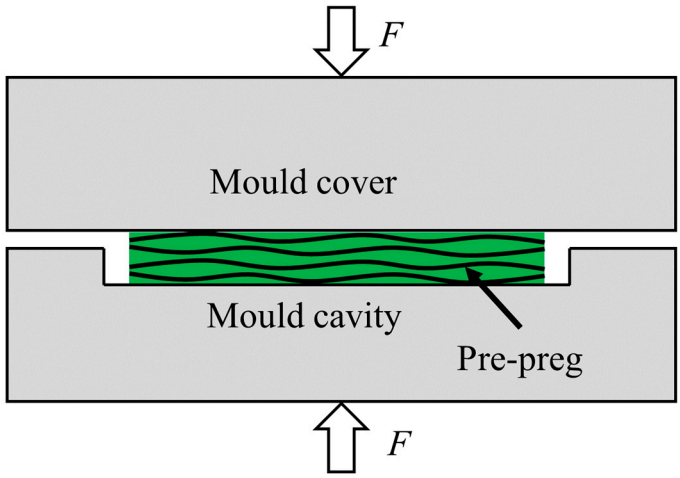

Figure 2.2. Schematic illustration of the compression moulding of carbon fibre pre-preg for CFRP manufacturing.

2.3 Induction heating theory

Induction heating is a non-contact heating method most commonly used for heating magnetic steel due to the potentially high heating efficiency. Examples of well-established applications are domestic induction cooktops and heat treatment of steel alloys. To increase the heating efficiency, the coil can be embedded in a soft magnetic flux-concentrating material, which increases the coupling of the magnetic field to the workpiece. The heat is generated within the workpiece by induced circulating currents, commonly denoted "eddy currents". An alternating current is driven through the induction coil, which gives rise to an alternating magnetic field surrounding the coil according to Ampere's law. According to Faraday's law of induction, a variation in a magnetic field will induce an electric field, which in turn gives rise to a current proportional to the electrical conductivity of the material, or to a displacement current in a dielectric material. In most cases, the heat will be generated due to resistive losses in the material, but other heating mechanisms also exist. In a ferromagnetic material, magnetic hysteresis will also contribute to the heating, although this is not a dominant factor in most applications. Another possible mechanism during the induction heating of CFRP is dielectric heating, as observed by Fink et al. [10], which is also of minor importance in most applications. Figure 2.3 shows a schematic illustration of possible current paths and heating mechanisms in CFRP. This figure illustrates a simple case with four carbon fibres (or carbon fibre tows), two aligned with the *x*-axis and two aligned with the *y*-axis, enabling a current loop if the crossing fibres are electrically

connected with each other. The contact between perpendicular fibres may be either resistive, illustrated by the junction resistance R_j, or capacitive, illustrated by the junction capacitance C_j. An alternating magnetic field in the z direction, B_z, induces voltages over the fibres according to Faraday's law of induction, which means that a circulating current will be formed in the fibres via the junction resistances and capacitances. This results in three possible origins of heating: resistive heating along the fibre resistance R_{fibre}; resistive heating in the junction resistance R_j; and dielectric heating in the junction capacitance C_j.

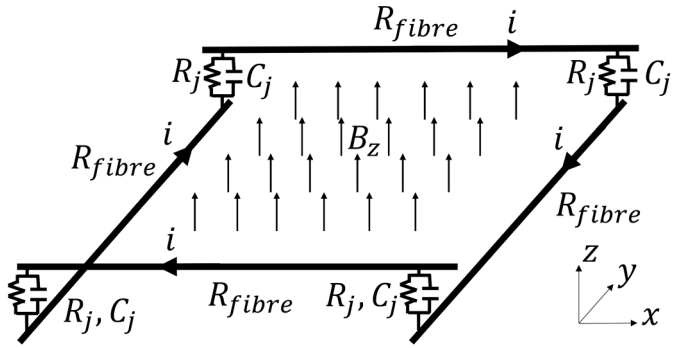

Figure 2.3. Illustration of a possible current path in CFRP with crossing fibres or fibre tows when applyng an alternating magnetic field, B_z. The crossing tows are connected through the junction resistance R_j and the junction capacitance C_j. Reprinted from Paper V.

The skin effect is a key concept in induction heating. When a solid wire conducts a direct current, the current density will be uniformly distributed, but in the case of an alternating current, the alternating magnetic field will give rise to induced internal currents. This results in a higher current density closer to the surface of the conductor and a lower current density at the centre of the conductor. The current density distribution follows equation (2.1), where d is the distance from the surface into the wire, and δ is the skin depth, which is defined as the distance from the surface where the current density has decreased to $1/e$ (~0.37) of the surface current density, J_s. The skin depth depends on the conductor material according to equation (2.2), where σ is the electrical conductivity, μ is the magnetic permeability, and f is the frequency of the sinusoidal alternating current.

$$J(d) = J_s e^{-\frac{(1+i)d}{\delta}} \tag{2.1}$$

$$\delta = \sqrt{\frac{1}{\pi f \sigma \mu}} \tag{2.2}$$

The proximity effect is another phenomenon related to alternating currents. Figure 2.4 (a) shows the relative current density distribution generated by a two-dimensional finite element simulation of two solid copper conductors close to an aluminium workpiece. 20 kHz sinusoidal alternating currents of equal magnitude and direction are driven through the conductors. The skin effect can be seen in the copper conductors as a concentration of the current closer to the conductor surface. The two wires will induce currents in each other in directions opposing each other. This opposing current will be stronger at the surface closest to the opposite conductor, observed as a reduced current density closer to the other conductor and a stronger current density on the opposite side. This phenomenon is known as the proximity effect. The same effect means that the current density will be stronger in the part of the conductor close to the workpiece, since the induced current in the workpiece will have a phase shift, according to Faraday's law of induction. It is clear that the skin effect and proximity effect result in a significant reduction of the effective current-carrying cross-sectional area of the conductors, causing high losses. Therefore water-cooled copper tubes are commonly used instead of solid copper wires, since the inner part is not effectively used as conductor in any case. To increase the effective conductive area, a litz wire may be used. A litz wire consists of multiple small-diameter strands, individually insulated and twisted so that the current is forced to be uniformly distributed in all strands. This is illustrated in Figure 2.4 (b) using a homogeneous representation of the Litz wire.

Although the fill factor (i.e., the cross-sectional area occupied by copper strands) is only about 50%, the effective current conducting area will be larger than in solid copper wire, reducing resistive losses and thereby the need for cooling.

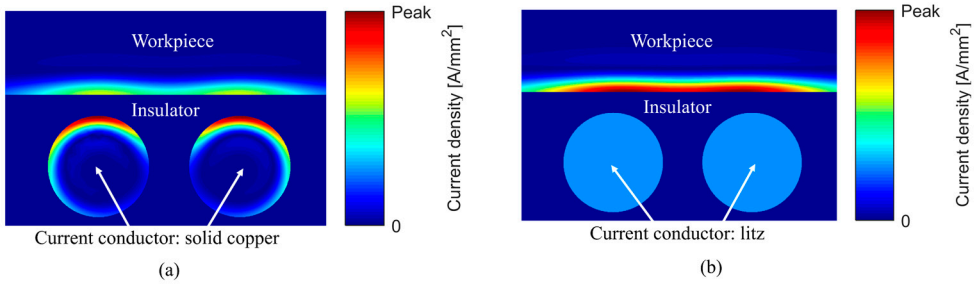

Figure 2.4. Illustration of skin effect and proximity effect. (a) The result of a two-dimensional finite element simulation of the current density distribution when two solid copper conductors with the same current direction are placed side by side with an aluminium workpiece above. (b) The same geometry but with the solid copper conductors replaced with litz wire. The litz domains are modelled using a homogeneous equivalent representation of a litz wire, without modelling each strand individually. The wires have a diameter of 6 mm. The simulationsrings are performed innthe software FEMM [34] Reprinted from Paper I.

2.4 Induction heating system

Figure 2.5 shows a schematic illustration of an induction heating system. A variable frequency drive (VFD) generates the alternating coil current. The VFD is connected to an impedance matching transformer in order to amplify current I_p (the primary winding current) of the transformer to I_s (the secondary winding current), driven through the coil. The coil has a resistance R and an inductance L, and its impedance Z is calculated according to equation (2.3); the reactance X depends on the inductance L according to equation (2.4). To optimize the system, it is desirable to minimize the reactive part of the impedance, since it is the resistive part that will generate the heating power. The reactive part opposes the induced current. The inductive reactance is reduced by connecting capacitor C in series with the coil. The reactance of the capacitor is expressed according to equation (2.5). The total reactance of the system is expressed according to equation (2.6). The capacitor C should be selected according to equation (2.7) in order to eliminate the reactive part of the impedance.

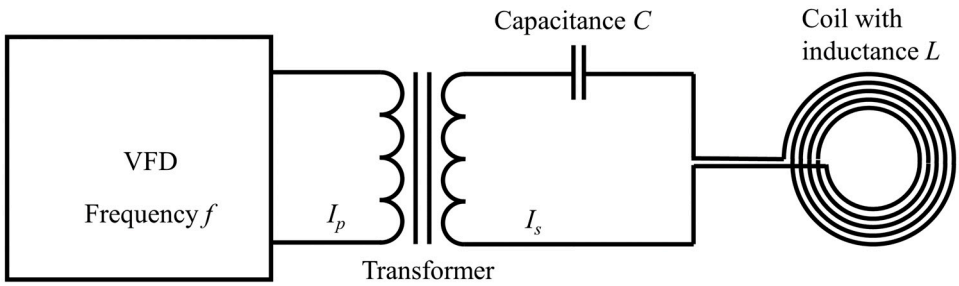

Figure 2.5. A schematic illustration of an induction heating system that includes a variable frequency drive (VFD) for generating the alternating current, a transformer, a resonant capacitor, and an induction coil.

$$Z = R + iX \tag{2.3}$$

$$X_L = 2\pi f L \tag{2.4}$$

$$X_C = -\frac{1}{2\pi f C} \tag{2.5}$$

$$X = X_C + X_L \tag{2.6}$$

$$f = \frac{1}{2\pi\sqrt{LC}} \tag{2.7}$$

3 Modelling

This chapter presents the developed models for predicting the heating power and temperature distribution during the induction heating of CFRP. The models are limited to represent the induction heating coil and the CFRP plate, so the frequency inverter, resonant capacitor, and transformer are omitted from the analysis. Three different models are presented, denoted Model I, Model II, and Model III. The coil current is always sinusoidal. The induction heating measurements are performed at approximately 60 kHz. The characterizations of all the material input parameters are presented in chapter 4.

3.1 Governing equations

An alternating current is driven through the induction coil, giving rise to an alternating magnetic field surrounding the coil according to Ampere's law. Ampere's law can be expressed in differential form, equation (3.3), which indicates that the curl of the magnetic field intensity **H** is proportional to the current density **J**. At significantly higher frequencies than used in this work it may also be necessary to consider the electric displacement field. An alternating magnetic field will give rise to an alternating electric field, according to Faraday's law of induction. This is expressed in differential form in equation (3.2). In a purely resistive material, the induced electric field will give rise to a current density according to Ohm's law (3.4). Equation (3.5) states the relationship between the magnetic field intensity **H** and the magnetic flux density **B**. Gauss's law for magnetism, equation (3.1), states that the divergence of **B** is always zero, which means that **B** is a solenoidal vector field and thus no magnetic monopoles can exist. The presented models only consider resistive losses, computed according to equation (3.6). Equations (3.1)–(3.3) are three of Maxwell's four equations. One of the four equations, Gauss's law, is not presented, since it is not relevant to induction heating problems in the frequency range used here. Gauss's law, which should not be confused with Gauss's law for magnetism, describes how the distribution of electric charges relates to the electric field. Material parameters used in the governing equations are: electrical conductivity σ, magnetic permeability μ, thermal conductivity λ, specific

heat capacity c_p, and density ρ. The resulting temperature distribution field is governed by the heat equation (3.7). In the presented models, the electromagnetic problem was solved using the finite element method (FEM) and the temperature distribution was computed using either FEM or the finite difference method.

$$\nabla \cdot \mathbf{B} = 0 \tag{3.1}$$

$$\nabla \times \mathbf{E} = -\frac{\partial \mathbf{B}}{\partial t} \tag{3.2}$$

$$\nabla \times \mathbf{H} = \mathbf{J} \tag{3.3}$$

$$\mathbf{J} = \sigma \mathbf{E} \tag{3.4}$$

$$\mathbf{B} = \mu_0 \mu_r \mathbf{H} \tag{3.5}$$

$$Q = \frac{\mathbf{J}^2}{\sigma} \tag{3.6}$$

$$\frac{\partial T}{\partial t} = \alpha_x \frac{\partial^2 T}{\partial x^2} + \alpha_y \frac{\partial^2 T}{\partial y^2} + \alpha_z \frac{\partial^2 T}{\partial z^2} + \frac{Q}{\rho c_p} \tag{3.7}$$

The electromagnetic problem is an open boundary problem that is modelled by assigning the magnetic insulation condition, equation (3.8), to the open boundary of the air domain. The magnetic vector potential **A** is defined according to equation (3.9), where **n** is the normal vector to the boundary.

$$\mathbf{n} \times \mathbf{A} = 0 \tag{3.8}$$

$$\mathbf{B} = \nabla \times \mathbf{A} \tag{3.9}$$

The CFRP domain has been assigned convective and radiative boundary conditions according to equations (3.10) and (3.11), where h is the convective heat transfer coefficient, A is the surface area with the temperature T, ε is the emissivity of the

surface, σ is the Stefan–Boltzmann constant, and T_0 is the temperature of the surrounding air. For the case of a small temperature difference between the object and the surrounding air and the absence of forced air convection, it may be a good approximation to set both the convective power $\mathbf{q_c}$ and radiative power $\mathbf{q_r}$ to zero. In Paper III (Model I), radiative and convective heat losses were disregarded and thus set to zero due to the small temperature difference. In the subsequent papers (Papers IV, VI, and VII), the convective heat transfer coefficient h was set to 10 W/m^{2}K, which was also used by Wasselynck et. [35]. This is a reasonable value for the natural convection of a horizontal surface according to the findings of Al-Arabi and El-Riedy [36] and Khalifa [37, 38].

$$\mathbf{q_c} = hA(T - T_0) \tag{3.10}$$

$$\mathbf{q_r} = A\varepsilon\sigma(T^4 - T_0^4) \tag{3.11}$$

3.2 Induction coil design

The purpose of this work is to explain and model the power distribution and temperature distribution in CFRP materials exposed to electromagnetic induction, rather than to optimize the temperature uniformity. Therefore, the induction coil design was chosen to reduce the complexity of simulation and manufacturing, resulting in a circular coil design. If isotropic material data are used, representative simulations can be performed using a two-dimensional axisymmetric model; for three-dimensional modelling, symmetries can be used to reduce the computations. The flat CFRP plates are typically made noticeable larger than the coil to avoid edge effects and to ensure that the same heating pattern is obtained independently of whether the plates are round or square.

To systematize and simplify the comparisons of temperature distribution, the same circular pancake coils were used in all studies investigating the temperature distribution (except for Paper II), and all the CFRP plates have the same outer dimensions 170 × 170 mm (except in the pre-study presented in Paper II and the dry fabric pieces used in Paper V). Figure 3.1 shows the 14-turn induction coil made for the thermographic experiments. It is made of a litz wire consisting of 500 individually insulated copper strands with individual diameters of 0.1 mm. By using litz instead of solid copoper conductors the power losses in the conductor can be reduced significantly as

demonstrated in Paper I. Another advantage with a litz-coil is that it is less frequency dependent, which is advantageous during modelling, as discussed in chapter 4. The mentioned coil and setup were used in the studies presented in Papers III, IV, VI, and VII.

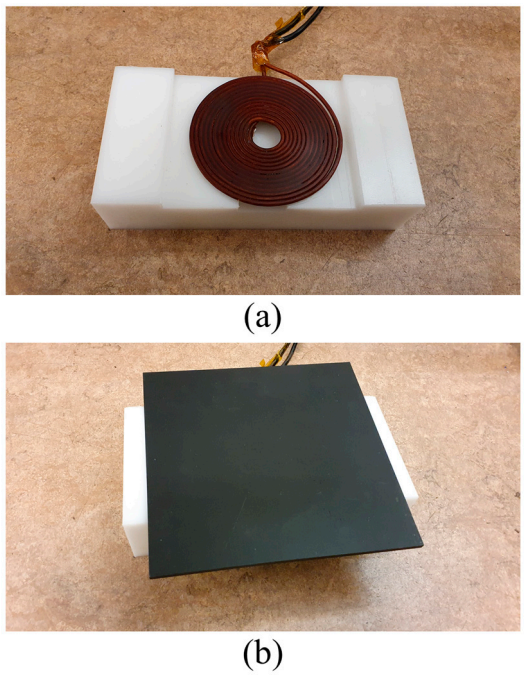

Figure 3.1. (a) The 14-turn induction coil placed in a coil holder to obtain a fixed distance between coil and CFRP plate. (b) A CFRP plate placed above the induction coil. Reprinted from Paper VI.

3.3 Temperature equalization

The simulation models are based on different levels of homogeneous anisotropic representations of the fibre composite. For example, a unidirectional fibre ply is considered a homogeneous and anisotropic domain in Model I. Both the electrical and thermal properties are represented with tensors or scalar values, meaning that local variations caused by non-uniformities in the fibre distribution cannot be included. All models represent simplifications of real CFRP materials, and thereby all the models depend to a certain degree on thermal equalization on a local scale. To analyse and compare different cases it is appropriate to discuss the temperature equalization time. The heat equation in one dimension, equation (3.12), can be solved using the finite

difference method FTSC (forward time centred space), resulting in equation (3.13), where $T(i, t)$ is the temperature at position i at time t. Assuming that the temperature is approximately the same on both sides of the peak according to Figure 3.2, the equation can instead be written according to (3.14), where ΔT_{peak} is the height of the temperature peak relative to its surrounding temperature. The time Δt to equalize a major part of the temperature difference ΔT can be approximated according to equation (3.15). Further on, the temperature equalization time, according to this one-dimensional approach, will be denoted with the symbol τ, defined according to equation (3.16), giving a rough estimate of the time to equalize a major part of the temperature difference ΔT over the distance Δz. This reasoning together with temperature measurements is used to describe and discuss the models.

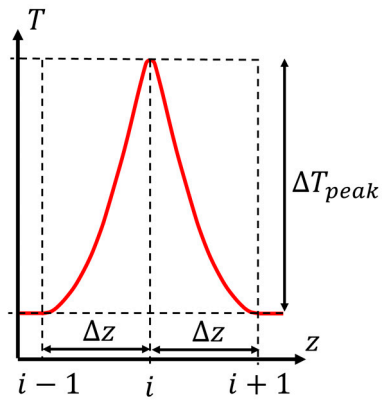

Figure 3.2. Illustration of a temperature peak ΔT_{peak} and the variables used in the heat equation for determining the approximation of the time τ to equalize a the major part of the thermal energy in a local temperature peak.

$$\frac{\partial T}{\partial t} = \alpha_z \frac{\partial^2 T}{\partial z^2} \tag{3.12}$$

$$\frac{T(i, t + \Delta t) - T(i, t)}{\Delta t} = \alpha_z \frac{T(i + 1, t) - 2T(i, t) + T(i - 1, t)}{\Delta z^2} \tag{3.13}$$

$$\frac{T(i, t + \Delta t) - T(i, t)}{\Delta t} = \alpha_z \frac{2\Delta T_{peak}}{\Delta z^2} \tag{3.14}$$

$$\frac{\Delta T_{peak}}{\Delta t} \approx \alpha_z \frac{2\Delta T_{peak}}{\Delta z^2} \Rightarrow \Delta t \approx \frac{\Delta z^2}{2\alpha_z} \tag{3.15}$$

$$\tau(\alpha_z, \Delta z) = \frac{\Delta z^2}{2\alpha_z} \tag{3.16}$$

3.4 Model I: 3D finite element model of cross-ply CFRP

3.4.1 Description of the model

In Paper III it is proposed that each unidirectional ply in cross-ply CFRP can be represented by a domain whose thermal and electrical properties are represented by scalars or tensors. It is reasonable to assume that this will provide a good representation of a cross-ply CFRP in which the fibres are uniformly distributed in the unidirectional layers. A three-dimensional finite element model was built using the software Comsol Multiphysics. Each unidirectional ply is represented by a homogeneous domain with the density ρ, the specific heat capacity c_p, the electrical conductivity tensor σ, and the thermal conductivity tensor λ. The electrical conductivity tensor is according to equation (3.19) for plies with the fibre direction along the *x*-axis and according to equation (3.20) for plies with the fibre direction along the *y*-axis. The thermal conductivity is according to equation (3.21) in plies with the fibre direction along the *x*-axis and according to equation (3.22) in plies with the fibre direction along the *y*-axis. The electrical conductivity and thermal conductivity are defined along the three orthogonal directions, i.e., L – along-fibre direction, T – transverse-fibre direction in plane, and Z – through the plate thickness, Figure 3.3.

The described tensor representation means that the value of σ_Z is constant through the thickness, and that there is no specific contact zone between the layers. This means that the dielectric coupling and the dielectric heating that may occur in resin domains between fibres cannot be represented by this model. However, as observed in the study by Becker et al. [39], the contribution of dielectric heating is negligible compared with the heating due to resistive contact resistance between crossing tows. In Paper III, plates with different thicknesses of unidirectional layers were built by stacking unidirectional plies in the same direction (depicted in Figure 4.1); therefore, the words “ply” and “layer” are disguised in this work. The mesh distribution through the thickness within plies and layers is

illustrated in Figure 3.3. Due to the high heat generation gradients close to the interface between crossing layers (shown in the result section) a higher mesh density is used, highlighted as light red and light green domains in the layer domains adjacent to a layer with perpendicular fibre direction. Only balanced and bidirectional CFRP plates were modelled and therefore symmetry conditions could be exploited, meaning that only a quarter of the whole geometry was modelled, Figure 3.3. The symmetry surfaces are assigned the magnetic insulation boundary condition, equation (3.8) and the thermal insulation boundary condition, i.e. equation (3.10) with the h set to 0 W/m^{2}K.

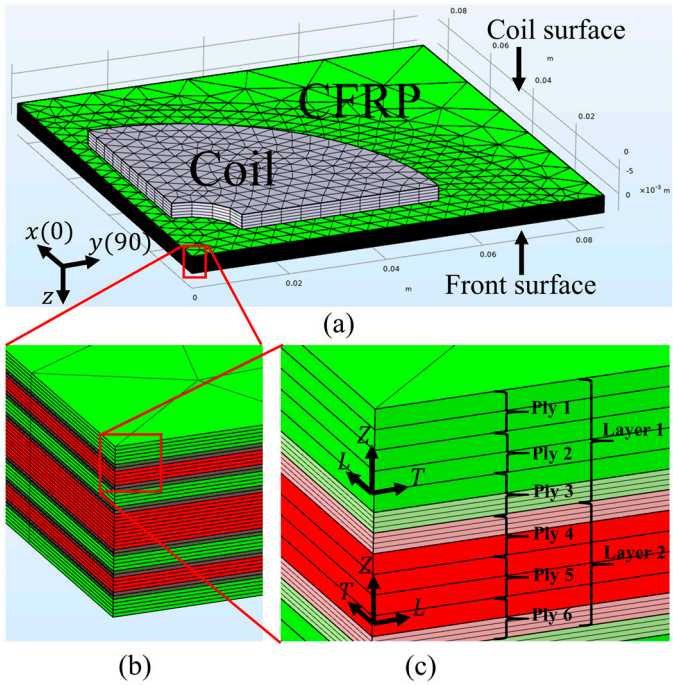

Figure 3.3. The geometry and mesh distribution of the finite element model representing the coil and CFRP plate. (a) The coil and CFRP domains. One quarter of the full geometry is modelled due to symmetry condictions. The coil and CFRP domains are surrounded by an electrically non-conductive air domain. The specific CFRP plate modelled in this case is plate 24-8 (the notations of the different plates are presented in chapter 4). (b) A close-up of the layer domains. (c) A close up of subfigure (b). Reprinted from Paper III.

The finite element model consists of an electrical part and a thermal part. In Paper III, only material properties measured at room temperature were used (in the temperature range 21-23 °C), which means that the electromagnetic problem and the thermal problem can be solved in sequence. In the first step, the current density field is computed according to Maxwell's equations and then the temperature distribution field is computed using the heat equation (3.7) based on the induced power distribution extracted from the electromagnetic simulation. A mesh convergence analysis is

described in Paper III. The current is uniformly distributed in the coil using a multi-turn coil domain, approximating the behaviour of a litz wire. The thicknesses of plies and layers are calculated according to equations (3.17) and (3.18) respectively, where d_{CFRP} denotes the thickness of the CFRP plate, d_{ply} denotes the ply thickness, and d_{layer} denotes the thickness of the layers.

$$d_{ply} = \frac{d_{CFRP}}{N_{plies}} \tag{3.17}$$

$$d_{UD} = \frac{d_{CFRP}}{N_{layers}} \tag{3.18}$$

$$\sigma_x = \begin{pmatrix} \sigma_L & 0 & 0 \\ 0 & \sigma_T & 0 \\ 0 & 0 & \sigma_Z \end{pmatrix} \tag{3.19}$$

$$\sigma_y = \begin{pmatrix} \sigma_T & 0 & 0 \\ 0 & \sigma_L & 0 \\ 0 & 0 & \sigma_Z \end{pmatrix} \tag{3.20}$$

$$\lambda_x = \begin{pmatrix} \lambda_L & 0 & 0 \\ 0 & \lambda_T & 0 \\ 0 & 0 & \lambda_Z \end{pmatrix} \tag{3.21}$$

$$\lambda_y = \begin{pmatrix} \lambda_T & 0 & 0 \\ 0 & \lambda_L & 0 \\ 0 & 0 & \lambda_Z \end{pmatrix} \tag{3.22}$$

3.4.2 Cross-ply representation of woven CFRP

Woven CFRP has a more complex geometry than does cross-ply CFRP. One approach is to represent the woven geometry in full detail, as done by Fu et al. [40]. To simplify the modelling of such composites, it is proposed in Paper IV that the induction heating of a woven CFRP plate can be simulated using the model for cross-ply CFRP. It is proposed that each woven fabric ply can be represented as a cross-ply CFRP according to

Figure 3.4, with the thickness of the equivalent unidirectional layers being calculated according to equation (3.23), where d_{ply} is the total thickness of a woven ply and d_{UD} denotes the thickness of the unidirectional plies in the cross-ply representation. Using the cross-ply representation model for woven fabric CFRP assumes that the temperature between crossing tows within a ply equalizes rapidly (approximated by equation (3.16)), in relation to the heating time. The simplified representation of a woven fabric is inserted in the numerical model, depicted in Figure 3.5 with four stacked fabric plies resulting in eight equivalent unidirectional perpendicular layers. The electrical conductance (inverse of resistance) between tows is quantified using the through thickness electrical conductivity σ_Z, characterized in the same way as for cross-ply CFRP.

$$d_{UD} = \frac{d_{ply}}{2} \tag{3.23}$$

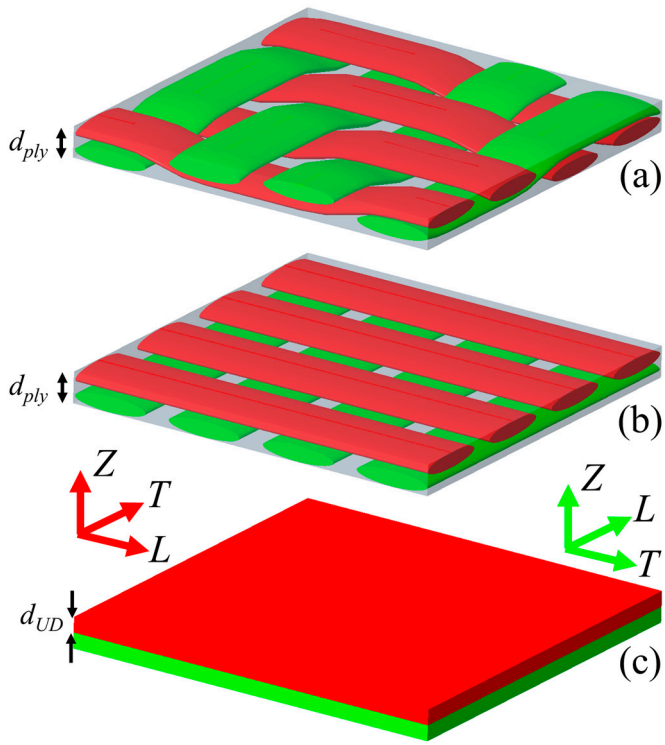

Figure 3.4. This figure shows how one twill-woven ply is represented with two unidirectional perpendicular layers. (a) A representative volume element of a piece of twill-woven fabric. (b) The woven fabric is simplified so that tows with the same fibre direction are placed on the same side. (c) The tows in subfigure (b) are represented by two homogeneous and anisotropic layers to be simulated in the three-dimensional cross-ply model presented in Paper III. Reprinted from Paper IV.

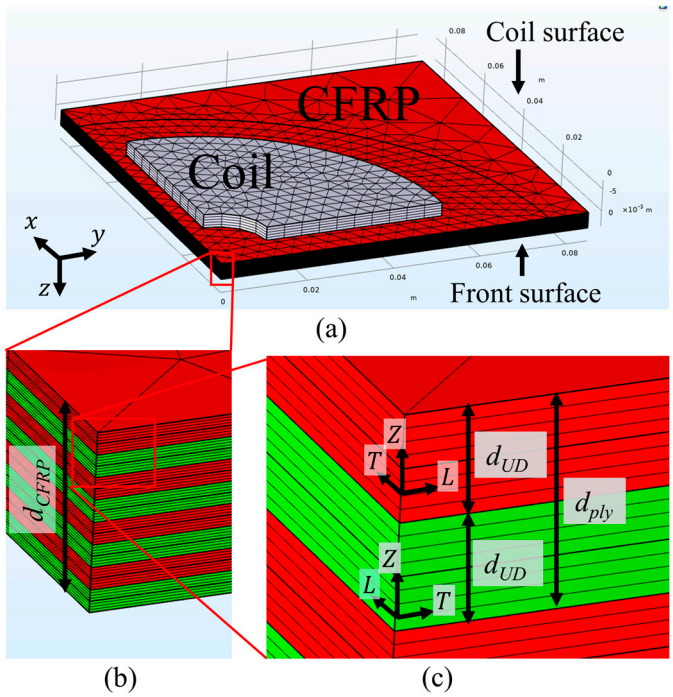

Figure 3.5. (a) The coil domain and CFRP domains surrounded by an air domain; this figure shows the cross-ply representation for 4 twill plies, consequently reresented by 8 unidirectional plies. (b) Close-up of the layer domains. (c) Close-up of subfigure (b). Reprinted from Paper IV.

3.5 Model II: Axisymmetric finite element model of CFRP

As shown in Papers III and IV, when using a circular coil parallel to the CFRP plate, the induced temperature distribution approaches a more circular pattern as the fibre volume fraction increases and the layer thickness decreases, i.e., similar to the behaviour of an isotropic material subjected to induction heating. This makes it reasonable that the modelling of such a setup could be significantly simplified using an axisymmetric finite element model, as described and implemented in Paper VI using the FEM-software software Comsol Multiphysics. The axisymmetric representation is also used in Papers II and V, but only with the electromagnetic part (implemented using the FEM-software FEMM 4.2 [34] and without examining the heat and temperature distributions. Figure 3.6 shows the geometry and mesh distribution of the axisymmetric finite element model. The electrical conductivity is represented by an equivalent scalar

value, which is described in chapter 4. Such a representation is only valid when the coil current is parallel with the CFRP plate and the induced currents circulate in the plane. As in the 3D model the density and heat capacity are represented by scalars while the thermal conductivity is represented by a radial component λ_R and a through thickness component λ_Z. In this model, temperature-dependent properties were also used, as presented in chapter 4.

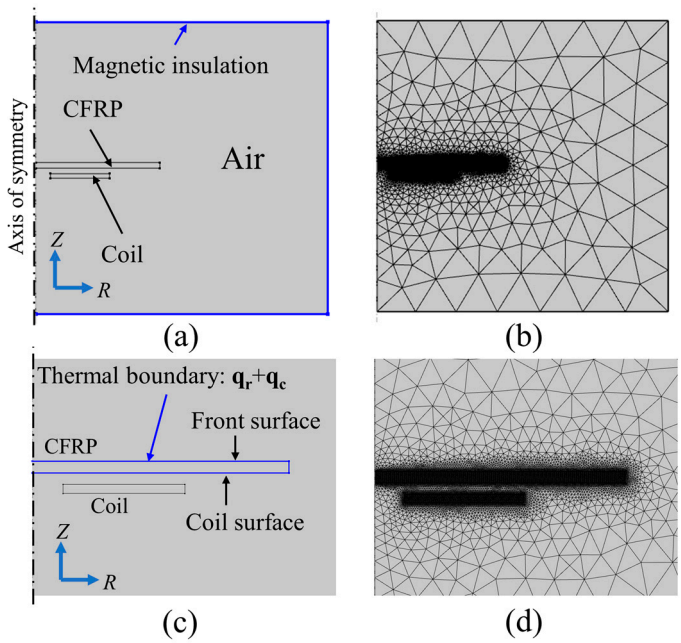

Figure 3.6: (a) The geometry of the 2D axisymmetric finite element model model, indicating the boundary condition of the magnetic insulation electromagnetic domain (blue boundary line). (b) The mesh of the whole geometry. (c) Close-up of the coil and CFRP domains, indicating the thermal boundary condition applied to the CFRP domain (blue boundary line of the CFRP domain). (d) The mesh of the close-up view. Reprinted from Paper VI.

3.6 Model III: Resistor network model

In Paper VII, a simulation model is proposed that uses a resistor network model for computing the induced power distribution on the local tow size level. The electromagnetic part of the axisymmetric model (Model II) is used to compute the induced electrical field E. Voltages acting over the discrete resistors are calculated from the distribution of the induced electric field. Employing Kirchhoff's circuit laws, a linear equation system can be established, thus computing the current flowing in each resistor. Since the through thickness distribution of the electromagnetic field is

computed in the axisymmetric FEM model the current distribution in each ply can be solved separately, thus significantly reducing the size of the equation system. During induction heating with an axisymmetric coil, it is assumed that the induced electric field will be approximately circular. Since the electrical part of the model is represented by resistors dielectric coupling and dielectric losses between crossing fibres are not modelled but could easily be added. Figure 3.7 shows how a piece of twill-woven fabric ply is discretized into square domains, and Figure 3.8 shows how the discrete elements of the fabric are represented by a network of resistors, as explained in detail in Paper VII. The resulting equations and how they are organized in an equation system are also presented in detail in Paper VII. The characterization of the resistances and the thermal properties are described in chapter 4.

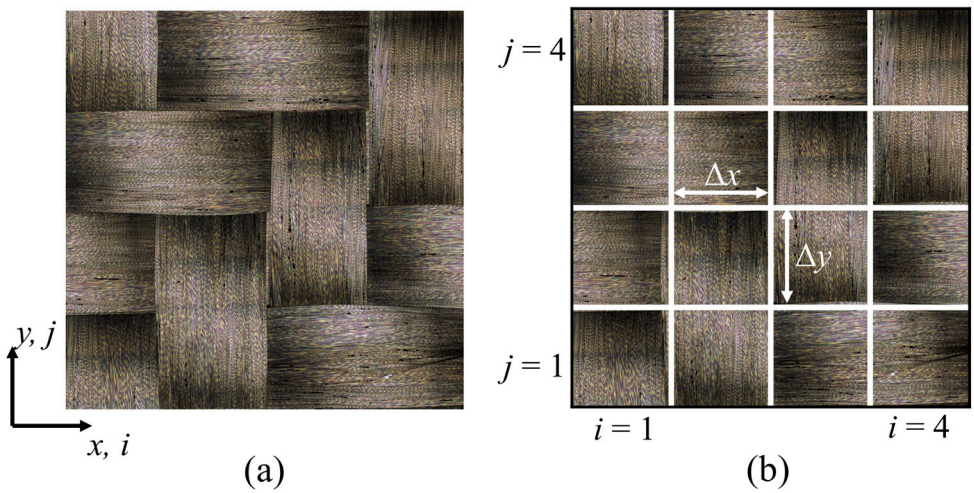

Figure 3.7. (a) Photography of a twill-woven carbon fibre fabric. (b) The woven fabric ply is discretized into square elements, consisting of two perpendicular pieces of carbon-fibre tow. Reprinted from Paper VII.

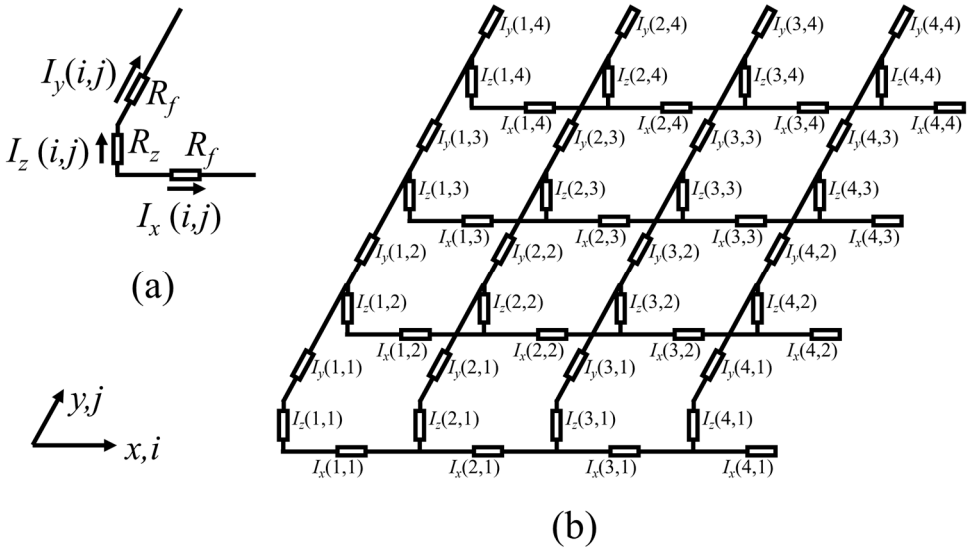

Figure 3.8. (a) One element is represented by the perpendicular resistances R_f (along fibre directions *x* and *y*) and the contact resistance R_z connecting the tows. (b) The resulting resistor network of 4 × 4 elements. Reprinted from Paper VII.

The next step is to compute the temperature distribution. This is accomplished by solving the heat equation using the finite difference method. For this purpose, the woven CFRP must be discretized. Figure 3.9 shows how a piece of woven CFRP is discretized into volume elements and how these are arranged in the case of multiple adjacent fabric plies, in this case 4 twill-plies. The induced heating power in each volume element is determined according to the current in the resistors associated with each volume element, described in Paper VII, which also presents the computation of the heat conduction between the volume elements.

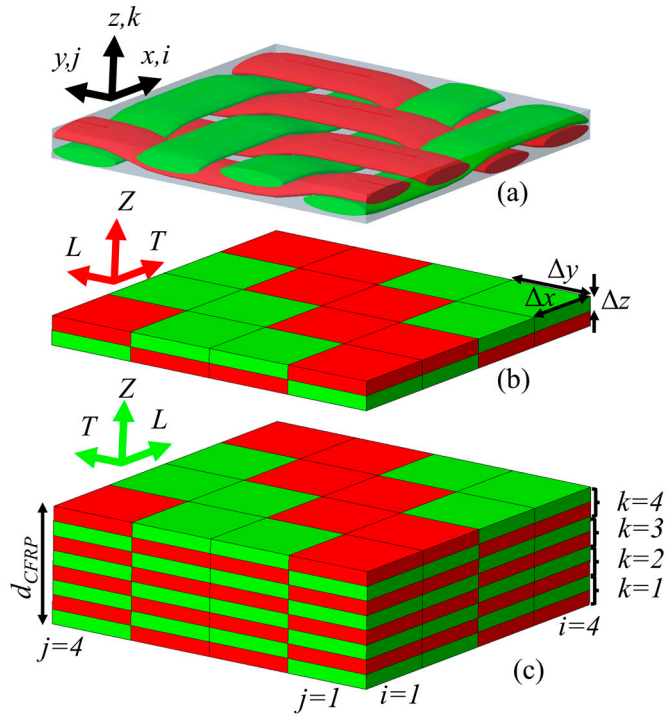

Figure 3.9. (a) A three-dimensional illustration of a twill-woven fabric. The colors red and green are used to indicate different fibre directions. (b) The woven structure is discretized into volume elements, used in the thermal part of the model; green volume elements represent tows with fibres aligned with the *x*-axis and red volume elements represent tows with the fibres aligned with the *y*-axis. (c) Multiple adjacent plies are represented using the discrete elements. Reprinted from Paper VII.

4 Material characterization

To validate the developed simulation models, several different cross-ply and woven CFRP plates were manufactured. CFRP plates were manufactured for two purposes: measurement of model input parameters, and for the thermographic induction heating experiments to be compared with the simulation results. Material parameters that need to be characterized are: electrical conductivity, thermal conductivity, specific heat capacity and density. This chapter presents the CFRP plates and samples manufactured for the mentioned purposes, and how the electrical and thermal properties were characterized. The results of the comparison between simulated and measured temperature distributions are presented in chapter 5.

4.1 Materials

The work presented in Paper II was conducted as a pre-study to identify parameters influencing the induction heating behaviour. The induction heating behaviour of a selection of different CFRP plates with different fibre types, fabric types, and layup arrangements was studied. More systematic studies were performed and presented in the subsequent publications (Papers III, IV, V, VI, and VII). The results presented in the pre-study, Paper II, indicated that the fibre volume faction, as well as the fabric type, layup, and fibre type, has a significant influence on the temperature distribution during induction heating. Due to the huge difference in thermal conductivity between the pitch-based fibre type (~200 W/(m·K)) and the PAN-based fibre type (~7 W/(m·K))), the temperature equalization is of course significantly faster in the pitch-based CFRP plate. To limit the scope of the subsequent studies (Papers III, IV, V, VI, and VII), it was decided to use only PAN-based fibres, by far the most common carbon fibre type. Due to their low thermal diffusivity, resulting in slow in-plane temperature equalisation, the distribution of the induced heating power becomes more critical, so this fibre type was also found to be more interesting to investigate.

CFRP plates were manufactured using resin transfer moulding. Both cross-ply CFRP plates based on unidirectional fibre sheets and woven CFRP plates were manufactured.

Table 4.1 presents the data on the epoxy matrix material used in all plates, and Table 4.2 presents data on the three different fibre fabrics used. The high weight fraction of binder material and sizing (14%) in the Mitsubishi TR50S fabric is due to the fact that the fabric is unidirectional. In a non-woven fabric, the fibres must be kept together in some way; in this case via a binder and polymer fibres, which can be observed in the microscopy images (Figure 4.1).

Table 4.1. Data on the epoxy matrix material. The thermal properties, presented in Paper IV, were measured using Laser Flash Analysis.

Property	
Epoxy resin	Olin D.E.N. 425 Epoxy Novolac
Epoxy curing agent	DOW D.E.H. 650 Epoxy Curing Agent
Density of cured epoxy, ρ_m	1204 kg/m^3
Thermal diffusivity of cured epoxy, α_m	0.156 mm^2/s
Specific heat capacity of cured epoxy, c_p	1360 kJ/(kg·K)
Thermal conductivity of cured epoxy, λ_m	0.255 W/(m·K)

Table 4.2. Data on the fibre fabrics based on three different fibre types; the values are specified by the manufacturers of fibre and fabric.

Fibre type	**Mitsubishi TR50S**	**Hexcel HexTow AS4**	**Toray T700S**
Fabric type	Unidirectional	Twill	Twill
Fabric ply area weight, ρ_A [kg/m^2]	0.1	0.6	0.6
Number of fibres per tow	Not applicable	12000	12000
Fibre density, ρ_f [kg/m^3]	1820 [41]	1790 [42]	1800 [43]
Thermal conductivity along fibres, λ_f	Not available	6.83 W/(mK) [42]	0.0224 Cal/cm·s·°C [43]
Fibre diameter [µm]	Not available	7.1 [42]	7 [43]

4.1.1 Cross-ply CFRP

To validate the three-dimensional cross-ply simulation model presented in Paper III, cross-ply plates with different fibre volume fractions and different layup sequences were manufactured for thermographic measurements during induction heating. Data on the manufactured plates are presented in Table 4.3. Unidirectional layers of different thicknesses were created by stacking multiple fabric plies in the same direction to enable investigation of how the ply thickness affects the heating power and temperature distribution during induction heating. Therefore, in the context of cross-ply CFRP, the words “layer” and “ply” have different meanings in this thesis. To create a layer thicker than one ply, multiple fabric plies with the same fibre direction were stacked before consolidation. The layup sequence of plies is symmetrical in all plates, except for plate 40-10. The layup in all plates is balanced, i.e., the number of *x*-directional plies equals

the number of *y*-directional plies. An even number of fabric plies was used in all plates, which means that in the plates with a symmetrical layup the two inner layers must have the same fibre directions. After manufacturing, the edges of the plates were cut away, so all plates have the final dimensions of 170 × 170 mm. The plates were named using the following notation: N_{plies}-N_{layers}, where N_{plies} represents the number of unidirectional fibre plies and N_{layers} represents the number of unidirectional layers. For example, a plate built up from 24 fabric plies divided into four equally thick unidirectional layers will be denoted 24-4.

Table 4.3. Data on the cross-ply CFRP plates. The plates were manufactured from unidirectional fibre sheets made of the Mitsubishi TR50S fibres. Adapted from Paper III.

Plate ID	Number of fabric plies, N_{plies}	Number of layers, N_{layers}	Layup sequence of plies	Plate thickness, d_{CFRP} [mm]	Fibre volume fraction, φ
24-4	24	4	$[0_6,90_6]_S$	3.62	0.29
24-8	24	8	$[(0_3,90_3)_2]_S$	3.43	0.30
24-12	24	12	$[(0_2,90_2)_3]_S$	3.60	0.30
24-24	24	24	$[(0,90)_6]_S$	3.58	0.30
32-4	32	4	$[0_8,90_8]_S$	3.65	0.37
32-8	32	8	$[(0_4,90_4)_2]_S$	3.48	0.39
32-16	32	16	$[(0_2,90_2)_4]_S$	3.60	0.39
32-32	32	32	$[(0,90)_8]_S$	3.61	0.39
40-4	40	4	$[0_{10},90_{10}]_S$	3.67	0.49
40-10	40	10	$[(0_4,90_4)_2]_S,90_4,0_4$	3.51	0.49
40-20	40	20	$[(0_2,90_2)_5]_S$	3.63	0.49
40-40	40	40	$[(0,90)_{10}]_S$	3.63	0.50

To characterize the thermal and electrical conductivity in specific directions relative to the fibre, i.e., the along-fibre or transverse fibre direction, it was necessary to manufacture CFRP samples with only one fibre direction. The equipment used for measuring the thermal diffusivity (Laser flash analysis) required samples 2 mm thick in the measurement direction and with a square cross-section of 10 × 10 mm normal to the measurement direction. A moulding tool with a cavity thickness of 20 mm was manufactured in order to obtain CFRP plates from which the characterization samples could be extracted.

Table 4.4 shows data on the 20 mm plates. Different number of plies were used to obtain different fibre volume fractions. These plates are denoted using the same convention as for the thinner cross-ply CFRP plates presented in Table 4.1. Plates 136-1, 178-1, and 220-1 thus consist of only one layer, i.e., only one fibre direction, and are intended for the extraction of samples for measuring electrical and thermal properties in the three orthogonal directions. Plates 136-136, 178-178, and 220-220

are intended for measuring conductivity through the thickness in cross-ply CFRP, to be compared with unidirectional case.

Table 4.4. Data on the CFRP plates intended for the characterization of thermal and electrical properties. These are 20 mm thick to allow extraction of multiple measurement samples in all directions. Adapted from Paper III.

Plate ID	Number of fabric plies, N_{plies}	Number of layers, N_{layers}	Layup sequence of plies
136-1	136	1	$[0_{136}]$
178-1	178	1	$[0_{178}]$
220-1	220	1	$[0_{220}]$
136-136	136	136	$[(0,90)_{68}]$
178-178	178	178	$[(0,90)_{89}]$
220-220	220	220	$[(0,90)_{110}]$

The fibre structure of each plate was inspected using optical microscopy. Cross-sectional images of the fibre structure of the thin cross-ply plates (~3.6 mm) are presented in Figure 4.1 and of the thick plates (20 mm) are presented in Figure 4.2. It was observed that the fibres are not uniformly distributed, especially in the plates with the lowest fibre volume fraction (~0.3). Thus, there is deviation from the homogeneous model, especially in plates with a low fibre volume fraction, in which the inhomogeneities are most noticeable. The plates have approximately the same thickness, so fewer plies result in a lower fibre volume fraction. In the models, the following notation is used to indicate direction in the unidirectional layers: L – along-fibre direction, T – transverse-fibre direction in plane, and Z – transverse fibre direction through the thickness. The directions are highlighted in a microscopy image of plate 40-10 in Figure 4.1 and in the unidirectional plates in Figure 4.2.

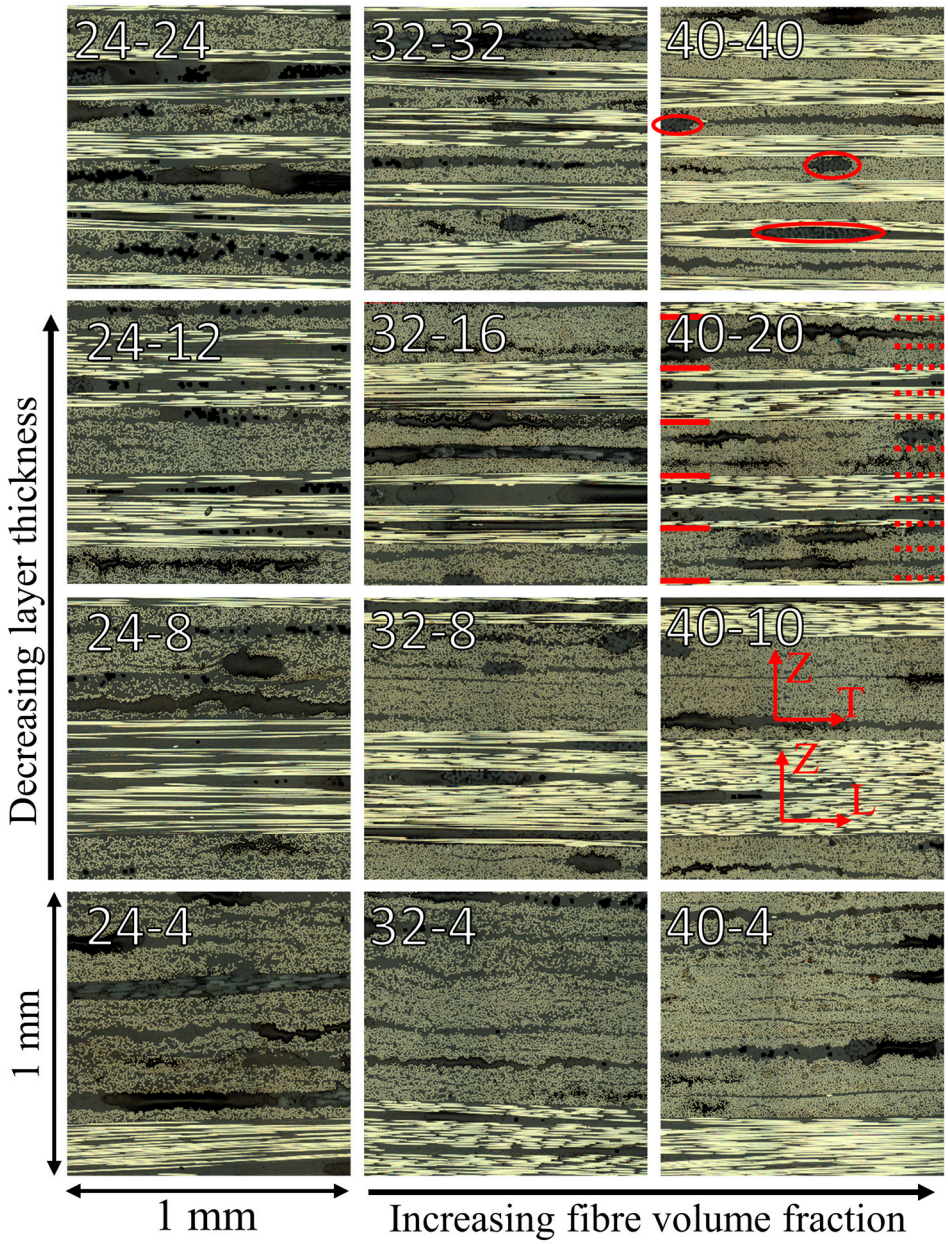

Figure 4.1. Microscopy images of the through-thickness fibre distribution in the cross-ply plates. In plate 40-20, the interfaces between unidirectional layers are marked with solid red lines and the interfaces between fabric plies are marked with dashed red lines. In 40-40, regions with polymer fibres are circled. In 40-10, directions *Z*, *L*, and *T* are indicated. The purpose of the polymer fibres in a ply is to hold the parallell carbon fibres together. Reprinted from Paper III.

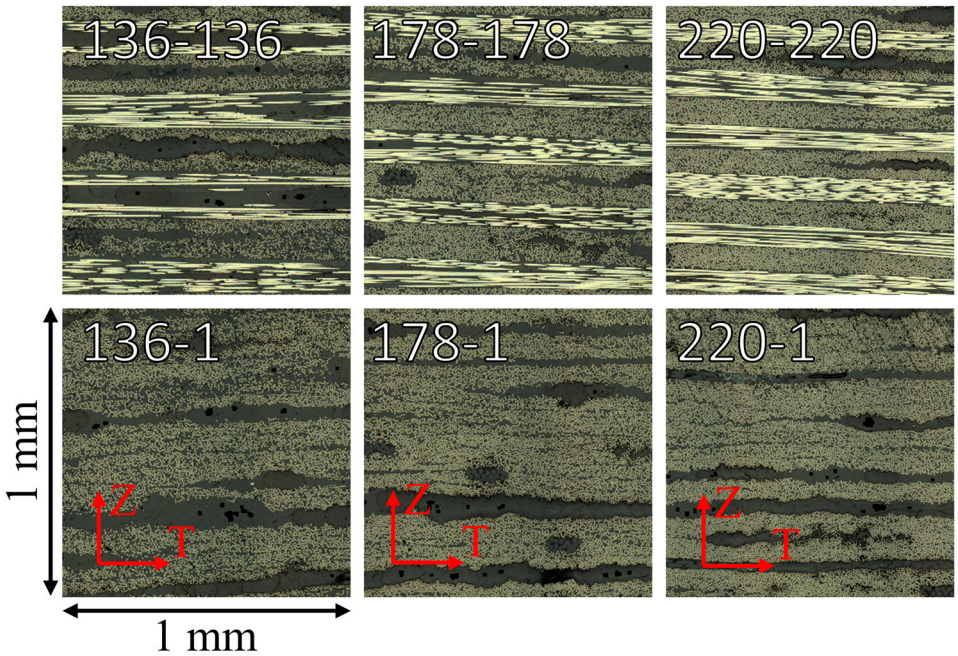

Figure 4.2. Microscopy images of the through-thickness fibre distribution in the thick cross-ply plates (seeTable 4.4). Reprinted from Paper III.

4.1.2 Woven CFRP

In Papers IV, VI, and VII, woven CFRP plates were used instead of cross-ply CFRP. Data on the manufactured plates are presented in Table 4.5. The fibre fabric used is twill-woven Hexcel HexTow AS4. For measurement of the in-plane thermal properties, plates were glued together; this procedure is described below in the section about laser flash analysis.

Table 4.5. Data on the twill-woven CFRP manufactured plates. This table presents how the plates are denoted in this thesis and in the articles where they were originally presented.

Plate ID	Plate ID notation in Paper IV	Plate ID notation in Paper VI	Plate ID notation in Paper VII	Number of plies, N_{plies}	Plate thickness, d_{CFRP} [mm]	Fibre volume fraction, φ
Twill-4plies-1	Plate 1	Not used	Plate 1	4	3.56	0.36
Twill-5plies-1	Plate 2	Not used	Not used	5	3.49	0.46
Twill-6plies-1	Plate 3	Not used	Not used	6	3.64	0.53
Twill-7plies-1	Plate 4	Not used	Not used	7	3.59	0.63
Twill-8plies-1	Plate 5	Plate 1	Plate 2	8	3.88	0.67
Twill-8plies-2	Not used	Plate 2	Not used	8	3.88	0.67
Twill-8plies-3	Not used	Plate 3	Not used	8	3.73	0.69

Microscopy images of the fibre structure in the twill woven CFRP plates are presented in Figure 4.3. As in the case of cross-ply plates, it is observed that a lower fibre volume fraction leads to a structure with more distinct resin-rich domains between the fibre tows.

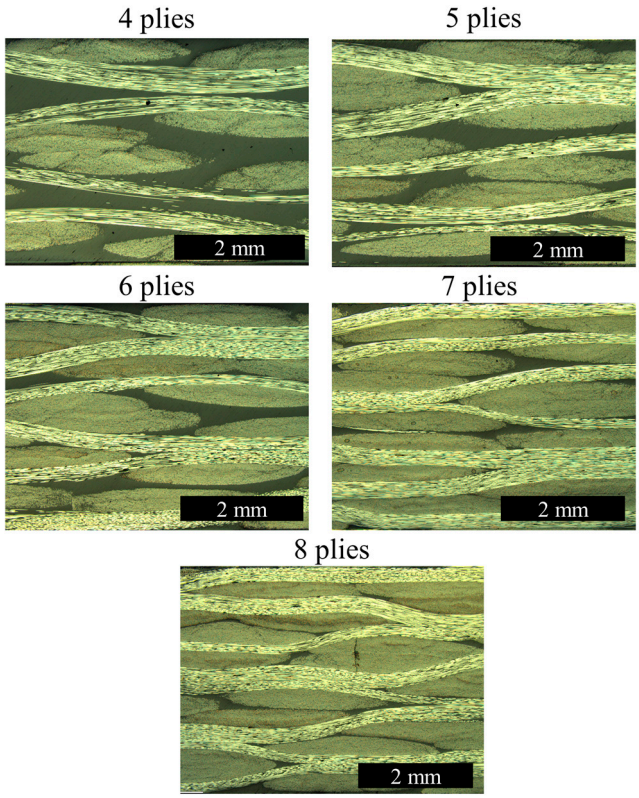

Figure 4.3. Microscopy images of the through-thickness fibre distribution in woven-based CFRP samples with different numbers of plies. Reprinted from Paper IV.

4.1.3 Dry-woven fabric

For the measurement of equivalent electrical conductivity in dry-woven fibres (Paper V), the fabric based on T700S fibres from Toray was used.

4.2 Density and fibre volume fraction

The sample density was measured as input to the LFA measurements and for determining the fibre volume fraction of each sample. The density of the composite ρ_c was measured according to ISO standard 1183-1:2012. The density was calculated according to equation (4.1), where m_A is the mass of the sample, m_L is the apparent weight of the sample when immersed in water, and ρ_L is the density of water. The fibre volume fraction ϕ of the samples were then calculated according to equation (4.2), where ρ_f is the density of the fibre and ρ_m is the density of the matrix material. The fibre sizing material and the binder material has approximately the same density as the epoxy matrix material. Alternatively, the fibre volume fraction can also be determined according to equation (4.3), where N_{plies} is the number of fabric plies, ρ_{A} is the area weight of a fabric ply, w_{sizing} is the weight fraction of sizing in the fabric, and ρ_f is the density of the carbon fibre.

$$\rho_c = \frac{m_A \cdot \rho_L}{m_A - m_L} \tag{4.1}$$

$$\phi = \frac{\rho_c - \rho_m}{\rho_f - \rho_m} \tag{4.2}$$

$$\phi = \frac{N_{plies} \cdot \rho_A \cdot (1 - w_{sizing})}{\rho_f \cdot thickness} \tag{4.3}$$

4.3 Four-terminal sensing of electrical conductivity

Model I is represented by homogeneous domains where the electrical conductivity is represented by a tensor. Four-terminal sensing can be used for measuring the electrical conductivity of a material on the macroscopic level in different directions, according to equation (4.4), where R is the measured resistance, l is the distance between the measurement electrodes, and A is the cross-sectional area normal to the current direction. A current I is driven through a sample with a constant cross-section and the voltage V is measured with two separate probes so as not to measure the contact resistance between the voltage electrode and specimen. Figure 4.4 shows the setup for measuring the directional electrical conductivity in CFRP samples. This setup, for

measuring direction-dependent electrical conductivity in consolidated CFRP, was only used for measuring the electrical conductivity in the T direction σ_T, with the result shown in Figure 4.5 (Paper III). Very high dispersion can be observed, because fibre distribution variations in the material are significant, but it may also depend on the difficulty of clamping the electrodes to the sample with a uniform contact pressure and thus not utilizing the entire cross-sectional area to conduct the current. However, as observed by Mizukami and Watanabe [44], the transverse in-plane component has a negligible influence on the resistance of the induction coil, thus negligible influence on the induced power and therefore is not a critical parameter during induction heating of cross-ply CFRP. Therefore, the value of σ_T was set to zero in the studies concerning three-dimensional modelling of woven CFRP (Papers IV and VII).

$$\sigma = \frac{l}{R \cdot A} \tag{4.4}$$

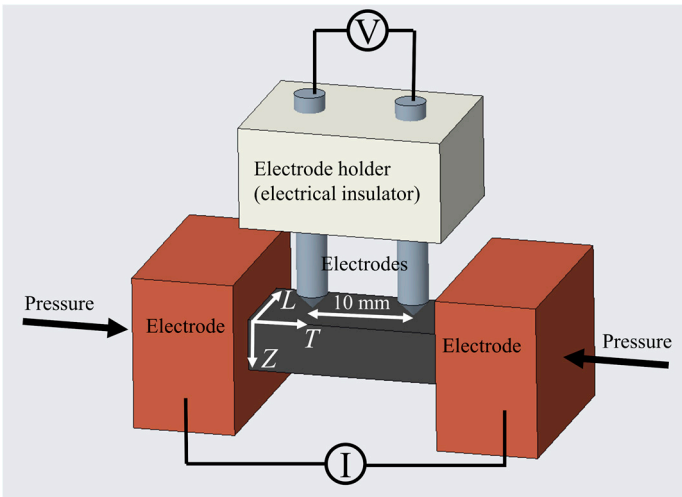

Figure 4.4. Illustration of the setup for characterization of direction-dependent electrical conductivity in consolidated CFRP samples, using four-terminal sensing. This figure shows the conductivity component σ_T being measured. The sample is attached between two copper electrodes. Reprinted from Paper III.

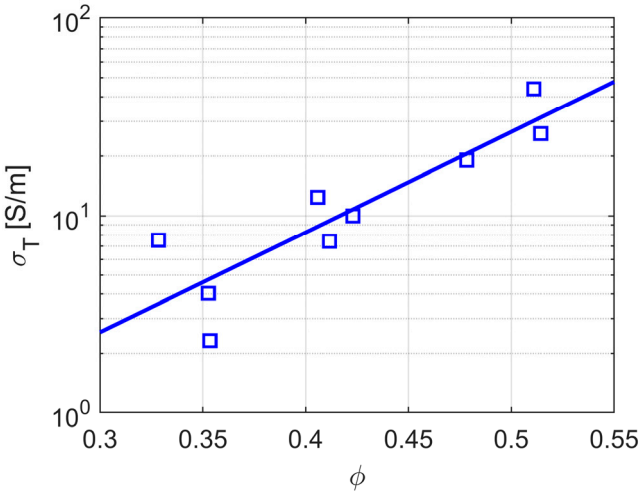

Figure 4.5. Measured values of σ_T versus the fibre volume fraction ϕ. The measurements were performed on samples extracted from 136-1, 178-1, and 220-1; three samples were extracted from each plate. Reprinted from Paper III.

The electrical conductivity along the fibre direction, σ_L is significantly higher than in the transverse direction σ_T. Therefore, measuring the electrical conductivity component, σ_L, requires relatively long samples to obtain a measurable resistance. Since the electrical conductivity along the fibre direction in CFRP follows the rule of mixtures, the resistance can instead be measured on a dry fibre tow or unidirectional fibre sheet with a known number of fibres and known cross sectional area. Figure 4.6 shows an illustration of the setup for measuring the resistance along the fibre direction in fibre tows and unidirectional fabric plies. The fibre diameters are known from the datasheet and thus the fibre conductivity σ_f can be calculated based on the measured resistance and the cross sectional area, according to equation (4.4). The macroscopic electrical conductivity component σ_L can then be determined according to equation (4.5). This approach is also used to determine the value of σ_L in a woven structure (Paper IV). In Model III (Paper VII), the discrete resistance along a tow R_f is used instead of the electrical conductivity. The through-thickness electrical conductivity σ_Z was measured using the inductive method presented in chapter 4.4. Table 4.6 shows the measured values of the electrical conductivity along the fibre direction.

$$\sigma_L = \phi\sigma_f \tag{4.5}$$

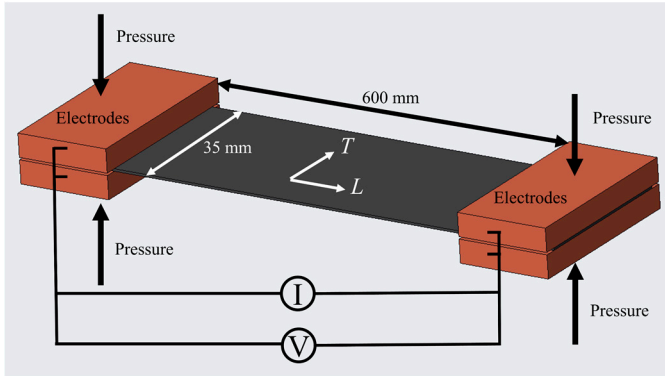

Figure 4.6. Illustration of the setup for measurement of resistance along-fibre direction in dry fabric specimens. Reprinted from Paper III.

Table 4.6. Longitudinal fibre conductivity, σ_f.

Fibre type	σ_f [kS/m]
TR50S	64.3, Paper III
AS4	63.2, Paper IV

4.4 Inductive characterization of electrical conductivity

4.4.1 Coil resistance

The total power loss in the induction heating system (coil and CFRP plate) is proportional to the measured coil resistance R_{coil} according to equation (4.6), where I is the effective coil current (root mean square). The total power loss P_{tot} accounts for resistive losses within the coil conductor itself. If an alternating coil current is applied, alternating currents will be induced in the CFRP plate, according to Faraday's law of induction. Consequently, the power loss P_{tot} constitutes the sum of all power losses within the coil conductor, P_{litz}, and in the CFRP plate, P_{CFRP}, equation (4.7). Therefore, if the internal loss P_{litz} is known in advance, the induced power P_{CFRP} can be determined from the measured coil resistance R_{coil}. As described in chapter 2, the resistance of a solid copper coil depends greatly on the frequency, due to the skin and proximity effects, both of which are related to the proximity between conductors and the proximity to the workpiece. A coil based on litz wire is significantly less frequency dependent and less dependent on the proximity to the workpiece, due to the twisting of the wire and the small diameter compared to the frequency dependent skin depth. As shown by Acero et al. [45, 46], the change in P_{litz} due to the proximity between coil and workpiece

is insignificant compared to the induced loss P_{CFRP}. Those studies were performed in the frequency range 1 kHz to 1 MHz and with litz-strand diameters in the range 0.2-0.5 mm. In the studies presented in this thesis an even smaller strand diameter, 0.1 mm, was used at the relatively low frequency 60 kHz. Thus, P_{litz} can be determined in advance by measuring the coil resistance R_{coil0} with no workpiece nearby and then P_{CFRP} can be determined according to equation (4.10) where ΔR is calculated according to equation (4.9). R_{coil} and R_{coil0} must be measured at the same frequency. If materials with non-linear magnetic permeability, such as flux concentrators, are not present the coil impedance will be independent of the amplitude of the coil current, so the internal loss P_{CFRP} can be determined for an arbitrary coil current based on a single coil resistance measurement of R_{coil} and R_{coil0} at the frequency of interest. As demonstrated in Paper I, a magnetic flux concentrator may increase the heating efficiency even more. However, by not using flux concentrators, there is a linear relationship between coil current and magnetic flux density that simplifies the model. In this work, the Hameg HM-8118 LCR meter was used for frequency-dependent coil impedance measurements. The heating efficiency can be calculated according to equation (4.11). It is worth emphasizing that this efficiency only includes the coil and CFRP plate and does not consider losses in the rest of the system, for example, in the frequency inverter. The linear relationship between the induced power and the coil resistance was employed to inversely compute different electrical conductivity components, as described in subsequent sections. Characterization of changes in frequency dependent coil resistance is also used in different kinds of non-destructive eddy current methods, for example, as used by Xu et al. [47], Bouloudenine et al. [48], and Naidjate et al. [49].

$$P_{tot} = R_{coil} I^2 \tag{4.6}$$

$$P_{tot} = P_{litz} + P_{CFRP} \tag{4.7}$$

$$P_{litz} = R_{coil_0} I^2 \tag{4.8}$$

$$\Delta R = R_{coil} - R_{coil_0} \tag{4.9}$$

$$P_{CFRP} = P_{tot} - P_{litz} = \Delta R I^2 \tag{4.10}$$

$$\eta = \frac{P_{CFRP}}{P_{tot}} = \frac{\Delta R}{R_{coil}} \tag{4.11}$$

4.4.2 Through-thickness electrical conductivity (Model I)

As input to Model I, the electrical conductivities in the *T*-direction and *L*-direction were characterized using a four-probe method, as previously described; however, for determining the electrical conductivity tensor component σ_Z, the four-probe method is difficult to use due to difficulties attaching the sample to the electrodes. The through-thickness electrical conductivity σ_Z in the three-dimensional finite element model (Model I) was instead determined inductively, according to Mizukami and Watanabe [44], by iterating the simulation, i.e., varying the value of σ_Z until the simulated coil resistance ΔR_s equalled the simulated coil resistance ΔR_m, according to equation (4.12). Figure 4.7 shows how the simulated value ΔR_s depends on the value of σ_Z for each of the cross-ply CFRP plates. For each case, the measured coil resistance ΔR_m is presented as a dashed line to show where the simulated value equals the measured value.

$$\Delta R_s(\sigma_Z) = \Delta R_m \tag{4.12}$$

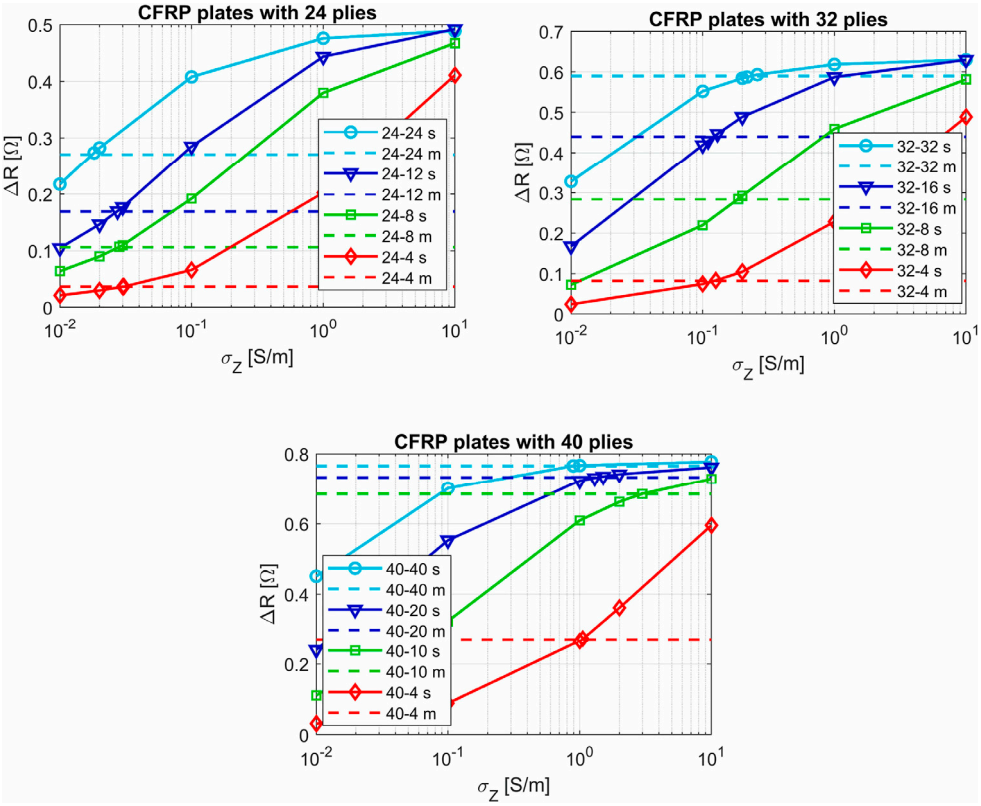

Figure 4.7. The simulated coil resistance increase ΔR_s as a function of σ_Z for each cross-ply plate. The measured coil resistance ΔR_m is presented for each plate to illustrate where the simulated value equals the measured value, thus the determined value of σ_Z. The distance between coil and CFRP plate was 0.5 mm diring tese measurements. Reprinted from Paper III.

Figure 4.8 presents the determined values of σ_Z as a function of the fibre volume fraction ϕ for all the cross-ply plates. It was found that σ_Z follows an exponential relationship with the fibre volume fraction but with a significant dispersion. Senghor et al. [50] also found that the transverse electrical conductivity depends exponentially on the fibre volume fraction. Due to the high dispersion, the measured value for each plate was used and not the corresponding value extracted by regression. The purpose of the regressions presented for the relationship between σ_Z and ϕ is therefore to highlight the exponential relationship; they are not for use in the numerical model.

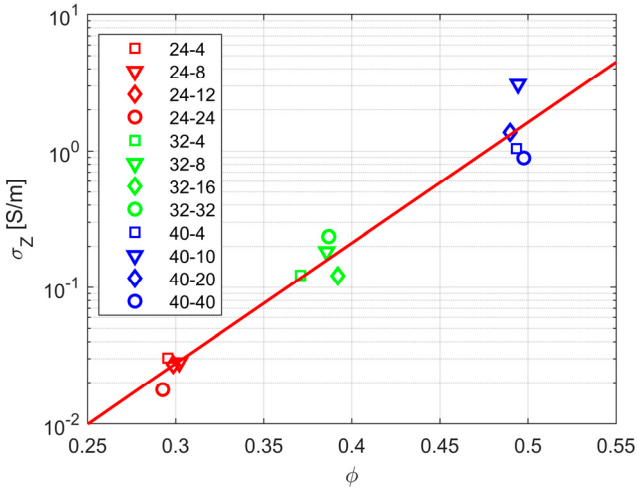

Figure 4.8. Values of σ_Z as a function of the fibre volume fraction ϕ. Reprinted from Paper III.

As proposed in Paper IV, the three-dimensional cross-ply finite element model can be used to represent a woven CFRP; the value of σ_Z can then be determined in the same way as for a cross-ply CFRP, although it should be emphasized that this is an equivalent homogeneous representation of the discrete electrical conductance between tows. The measured values from the five plates presented in Paper IV are shown in Figure 4.9 as blue squares. For the purpose of comparison, the values of σ_Z from Figure 4.8 are also shown, as red circles. Despite the high dispersion, it is clear that the value of σ_Z is higher in the woven CFRP than in the cross-ply plates, possibly due to the larger contact area between crossing tows in a fabric than in a cross-ply layup, observed by Rudolf et al. [18] or possibly due to higher local contact pressure between fibres in different directions.

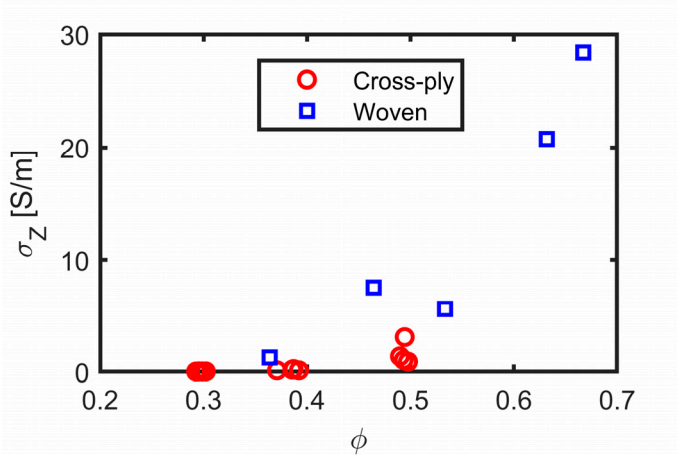

Figure 4.9: Comparison between σ_Z in cross-ply and in woven CFRP. Red circles: cross-ply CFRP plates (the same as shown in Figure 4.8. Blue squares: woven CFRP plates.

4.4.3 Equivalent electrical conductivity (Model II)

In the axisymmetric Model II, the CFRP structure is modelled as a homogeneous and isotropic material from the electromagnetic perspective. This representation presupposes low electrical resistance between crossing fibres, so that the material behaves like an isotropic material from an induction heating perspective, when inducing currents circulating in-plane. The equivalent electrical conductivity is characterized by measuring the coil resistance increase due to the presence of the adjacent CFRP plate and then comparing it with the simulated coil resistance, analogous to the approach to determining the through-thickness electrical conductivity, σ_Z, presented in the previous section. In Paper II, the equivalent electrical conductivity was determined by minimizing the goal function, equation (4.13), based on a range of frequencies, i.e., the least square method. It is also possible to perform the optimization with respect to both the coil resistance and coil inductance, as in Paper V; however, as observed in Paper V, the change in coil inductance due to changes in equivalent electrical conductivity is marginal, which is also supported by Mizukami and Watanabe [44], so only the coil resistance was used in the subsequent Paper VI. If the optimization is performed with respect to the coil resistance increase, ΔR, and at only one frequency, the optimization problem simply concerns finding the equivalent electrical conductivity σ_e for which equation (4.14) is satisfied, analogous to equation (4.12) for determining σ_Z.

$$\sum_{n}^{N_f} \left(\Delta R_s(\sigma_e, f_n) - \Delta R_m(f_n)\right)^2 \tag{4.13}$$

$$\Delta R_s(\sigma_e) = \Delta R_m \tag{4.14}$$

In the study presented in Paper VI, the temperature dependence of the equivalent electrical conductivity was characterized. The coil setup with the CFRP to be characterized was mounted in a convection oven and the frequency-dependent coil resistance was measured at different stationary temperature levels, and thus the temperature-dependent equivalent electrical conductivity could be determined. The temperature dependence of the coil resistance R_{coil0} (without adjacent workpiece) was also measured in order to compensate for the temperature dependence of the litz wire resistance. The result is shown in Figure 4.10; the left subfigure shows the temperature dependence of ΔR and the right subfigure shows the resulting temperature dependence of the equivalent electrical conductivity σ_e. Equations for the regressions are presented in Paper VI. The noticeable higher values of ΔR_m and σ_e for plate Twil-8plies-3 are due to the higher fibre volume fraction in this plate.

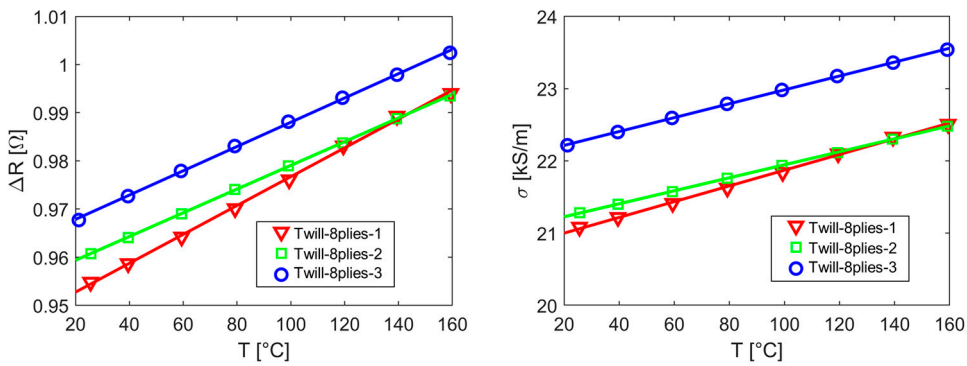

Figure 4.10. Adapted from Paper VI in which the plates are denoted: plate 1, plate 2, and plate 3. Left subfigure: the measured coil resistance ΔR_m. Right subfigure: equivalent electrical conductivity σ_e as a function of temperature in the woven fabric plates.

4.4.4 Equivalent electrical conductivity in dry weave (Model II)

Paper V describes a method for characterizing equivalent electrical conductivity σ_e in non-consolidated dry fibre fabric, for example to predict the electrical conductivity before consolidation and to predict how it will depend on the applied pressure. A coil

is embedded in a non-magnetic and electrically non-conductive cylinder so that the coil resistance ΔR_m can be measured simultaneously as a uniform pressure is applied to the fabric. Figure 4.11 shows a cutaway drawing, illustrating the principle with an embedded coil adjacent to a twill-woven fabric ply. By applying pressure to the plastic cylinder with the embedded coil, the perpendicular tows will establish better electrical conductance with one another, which will be seen as a change in measured frequency dependent coil resistance ΔR_m and consequently a higher value of σ_e.

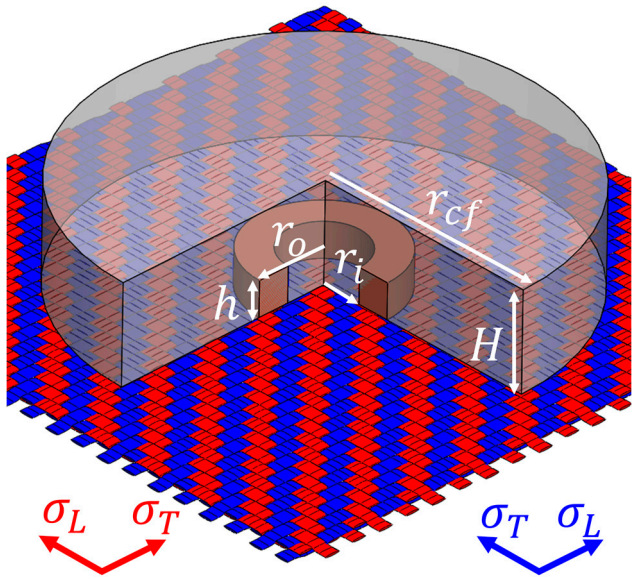

Figure 4.11. Cutaway drawing of an embedded coil placed adjacent to a twill-woven fabric ply. Tows in different directions are shown in red or blue to highlight the perpendicular fibre directions. The in-plane electrical conductivity components in each direction are highlighted. Reprinted from Paper V.

Figure 4.12 shows the setup used to apply pressure to the fibre fabric while measuring the frequency dependent coil resistance. The parts close to the coil and fabric need to be electrically non-conductive and non-magnetic, so they are made of the glass fibre composite G11. Paper V investigates how the equivalent electrical conductivity depends on changes in the thickness of the stacked fabrics and applied pressure. The thickness of the stacked fabrics is measured by linear variable differential transformers measuring the distance between the surrounding G11 pieces (green parts), and thus the fibre volume fraction can be calculated according to equation (4.3).

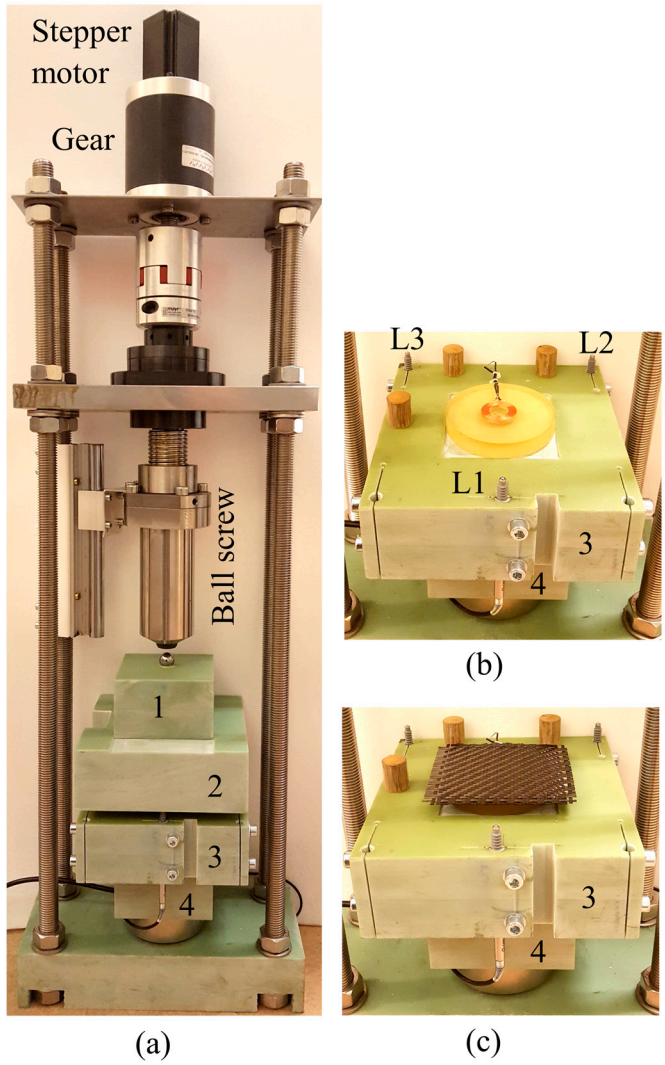

Figure 4.12. (a) Press setup for measuring the equivalent electrical conductivity of carbon fibre fabric during pressure application. (b) The embedded coil placed in the press setup. (c) Dry twill-woven fabric plies stacked above the coil. Reprinted from Paper V.

Measurements were performed with two different embedded coils of different size, shown in Figure 4.13. The measurements were performed by slowly increasing the pressure. Dry twill-woven fabric plies based on T700S-type fibres from Toray were used to evaluate the method. It was observed that the value of the equivalent electrical conductivity σ_e depends on the coil size when measured on the same CFRP fabric having a low fibre volume fraction (see Figure 4.14). As the fibre volume fraction

increases the equivalent electrical conductivity converges for the two measurement coils. In Paper V, it is proposed that the equivalent electrical conductivity σ_e can be approximated according to equation (4.15) where σ_f is 62.5 kS/m [43]. In Figure 4.14, the curve based on equation (4.15) is denoted σ_0. The convergence for the value of σ_e obtained with the two coils at higher fibre volume fraction levels indicates that the axisymmetric representation works better as the fibre volume fraction increases and the resistance between crossing tows decrease. This also agrees with the findings in Paper III and IV, i.e., that the heating pattern becomes more axisymmetric as the fibre volume fraction increases. Paper V only considers the determination of an equivalent electrical conductivity σ_e but the proposed setup could as well be used for determination of the σ_Z in dry fabric, according to the approach presented in Paper IV. It should be noted that the infiltration and consolidation process may change the fibre contact resistance.

$$\sigma_e = \frac{\phi \sigma_f}{2} \tag{4.15}$$

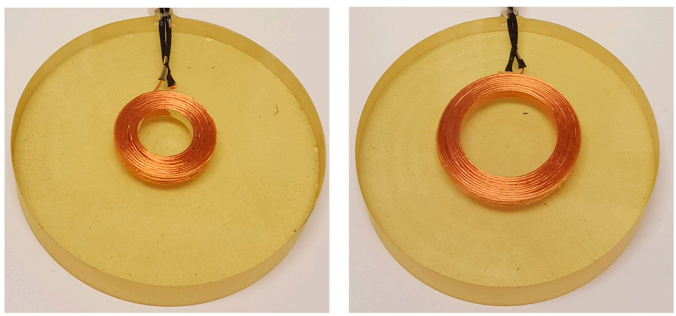

Figure 4.13. Embedded measurement coils. The coils are made of litz wire consisting of 30 strands with individual diameters of 0.1 mm. Both coils have 108 turns. (a) coil 1: Embedded coil with inner radius 8.2 mm, outer radius 14.7 mm, and height 7.3 mm. (b) coil 2: Embedded coil with inner radius 14.9 mm, outer radius 21.6 mm, and height 7.1 mm. Reprinted from Paper V.

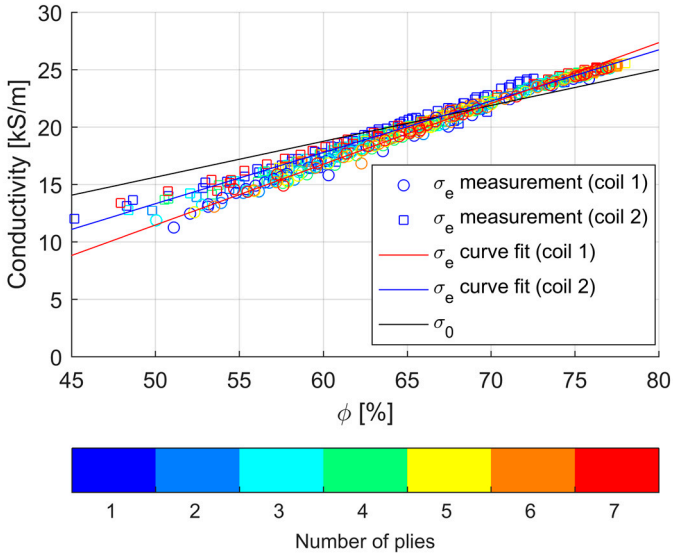

Figure 4.14. Equivalent electrical conductivity σ_e in dry-woven fabric based on T700S-type fibres from Toray. Reprinted from Paper V.

4.4.5 R_z in the resistor network model (Model III)

The equivalent electrical conductivity in the axisymmetric model is computed according to the method described in Paper VI. The radial distributions of the electric field for the different plies are then extracted from the 2D axisymmetric FEM. Figure 4.15 shows the simulated electric field distribution in plate Twill-4plies-1. The extracted electric field is then applied over the in-plane directional resistors as described in Paper VII. The value of R_f is determined from the measurement of the AS4-fibre presented in Table 4.6. The value of R_z is computed inversely according to equation (4.16) using the same approach as for computation of σ_Z. The characterized values of the equivalent electrical conductivity σ_e and R_z are presented in Table 4.7.

$$\Delta R_s(R_z) = \Delta R_m \tag{4.16}$$

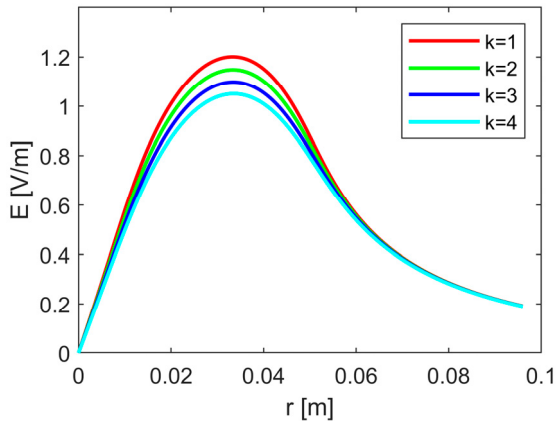

Figure 4.15. From the axisymmetric model, the electric field is extracted for each ply, with the highest value in the ply closest to the coil (ply number k = 1). This figure presents the extracted electric field for plate Twill-4plies-1. Reprinted from Paper VII.

Table 4.7. Measured coil resistance and characterized values of electrical conductivity and resistance when modeling two different twill woven CFRP plates using Model III: R_{coil0}=0.0321 Ω. Reprinted from Paper VII.

Plate ID	R_{coil} [Ω]	ΔR_m [Ω]	σ_e [S/m]	R_z [Ω]
Twill-4plies-1	0.42	0.39	9744	10.2
Twill-8plies-1	0.77	0.74	20902	1.12

4.5 Thermal diffusivity and specific heat capacity

4.5.1 The LFA method

Laser flash analysis (LFA) is a method developed by Parker et al. [51] for measuring thermal diffusivity α and specific heat capacity c_p. Using the density ρ of the sample, the thermal conductivity λ is calculated according to equation (4.17). Figure 4.16 shows the measurement setup within the equipment. The sample is placed in a sample holder within a furnace chamber, which makes it possible to conduct the measurements at different temperatures. During a diffusivity measurement, the bottom surface of the sample is exposed to a light flash pulse with the energy per area unit q [J/m^2] and at the same time the temperature transient of the upper surface is detected using an infrared temperature sensor. Figure 4.17 shows a typical temperature curve of the upper surface after exposing the bottom surface to a light flash. The diffusivity is calculated according to equation (4.18), where d is the thickness of the sample and $t_{1/2}$ is the time it takes for the top surface temperature to reach half of the temperature increase ΔT_{max}, as indicated

in Figure 4.17. The temperature increase ΔT_{max} depends on the pulse energy q and the material properties according to equation (4.19). By measuring the temperature increase of a reference sample with known specific heat capacity using the same pulse energy q the specific heat capacity of the sample can be calculated according to equation (4.20), where the subscripts *s* and *r* stands for sample respective reference sample. Prior to the measurement, the samples must be painted with a thin layer of graphite in order to get the same emissivity.

$$\lambda = \alpha \rho c_p \tag{4.17}$$

$$\alpha = 0.1388 \cdot \frac{d^2}{t_{1/2}} \tag{4.18}$$

$$\Delta T_{max} = \frac{q}{\rho d c_p} \tag{4.19}$$

$$c_{p_s} = \frac{\rho_r d_r c_{p_r} \Delta T_{max_r}}{\rho_s d_s \Delta T_{max_s}} \tag{4.20}$$

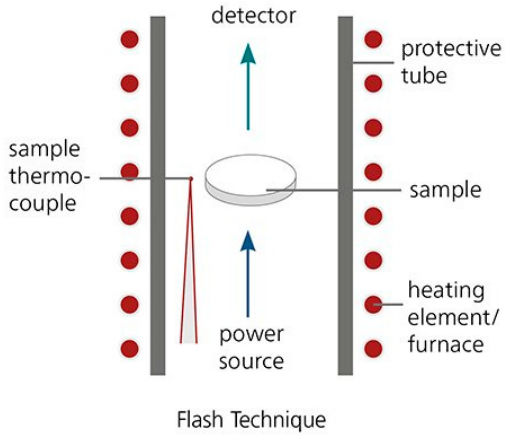

Figure 4.16. Illustration of the measurement setup during laser flash analysis for measuring temperature-dependent diffusivity. When the sample has reached the reference temperature, the sample is exposed to a light flash and the temperature of the upper surface is measured using an infrared sensor. Reprinted from NETZSCH [52].

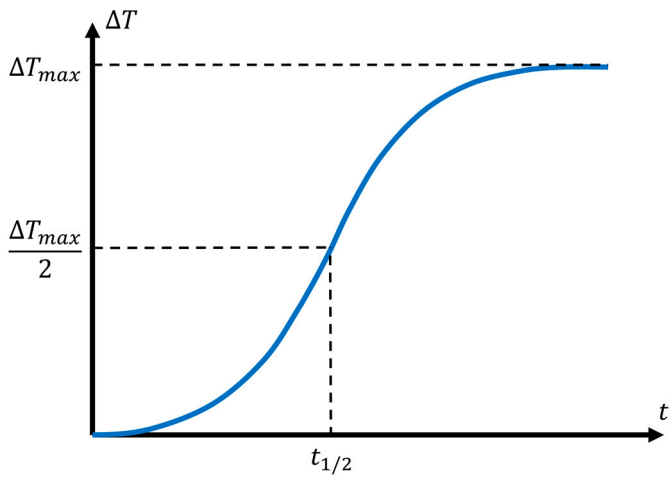

Figure 4.17. How the temperature of the upper surface increases with time *t* after the sample has been exposed to a light flash. The diffusivity is determined from this curve according to equation (4.18).

4.5.2 Characterization of CFRP using the LFA method

The LFA-method was developed for isotropic and homogeneous materials but has also been shown to be useful for direction-dependent measurements in anisotropic and inhomogeneous materials, as observed by Joven and Minaie [53]. For LFA measurements, the LFA 467 HT HyperFlash device from NETZSCH was used. The sample size required by this equipment is significantly larger than the fibre and tow size, which means that a macroscopic mean value will be measured. The characterized direction-dependent values can thus be incorporated directly into the homogeneous representations used in the different models. For the measurements in this work, a square sample holder was used. This holder requires the sample to have a square surface of 10 × 10 mm normal to the measurement direction and a thickness of 2 mm. For the woven CFRP plates, the sample extraction procedure is illustrated in Figure 4.18. The figure shows how LFA samples are extracted for measuring the thermal diffusivity in the three orthogonal directions, i.e., x, y, and z, of the woven CFRP plates.

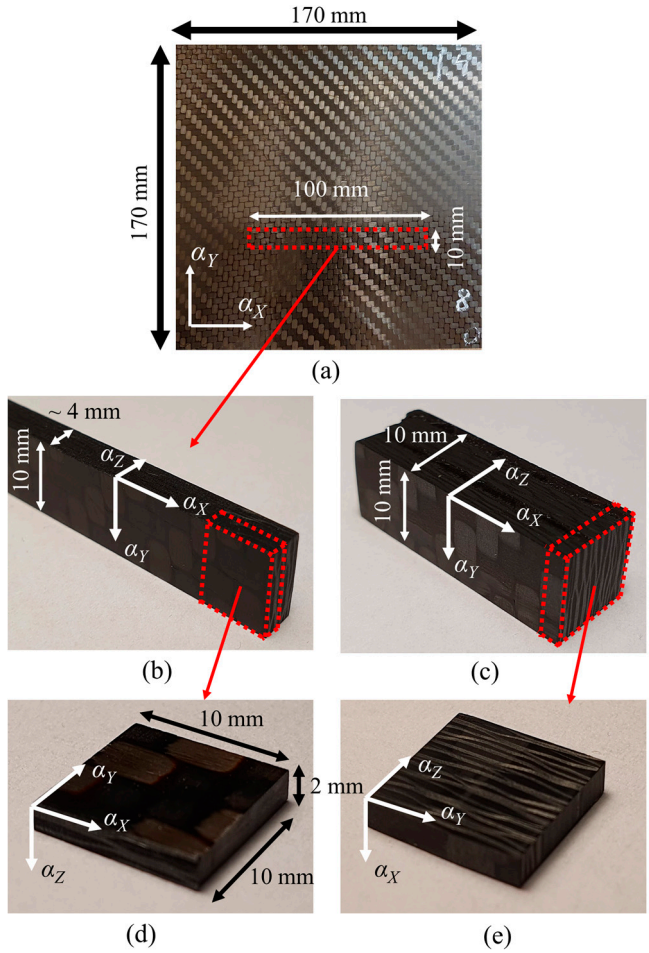

Figure 4.18. Extraction of LFA samples in different directions of woven CFRP. (a) One of the twill-woven plates. (b) A CFRP bar cut from the CFRP plate. The thermal diffusivity components α_Z, α_X, and α_Y are highlighted. The red dotted lines emphasize the contours of an LFA sample to be cut for the purpose of measuring the thermal diffusivity component α_Z. (c) The resulting CFRP bar after gluing together three bars cut from the CFRP plate. The bar is ground to have a 10 × 10-mm cross-section. The contours of an LFA sample for the measurement of α_X are shown by dotted red lines. (d) The resulting α_Z sample. (e) The resulting α_X sample. Reprinted from Paper IV.

Figure 4.19 shows the values of α_Z and α_T measured in the unidirectional samples and corresponding regressions with respect to the fibre volume fraction. To characterize the in-plane components T and L, samples were extracted from the unidirectional plates 136-1, 178-1, and 220-1. For measurement in the z-direction, the cross-ply plates 136-136, 178-178, and 220-220 were also used to investigate how the through-thickness thermal diffusivity was affected by the ply layup. The values measured on the unidirectional samples are denoted α_Z [0] and the values measured on the cross-ply

samples are denoted α_Z [0/90]. No noticeable difference can be observed between α_Z [0] and α_Z [0/90], so the linear regression for α_Z is based on both α_Z [0] and α_Z [0/90]. It is also observed that α_T is noticeably higher than α_Z, which might depend on the fact that the fibre plies are separated by large resin-rich regions, which is not the case in the T-direction. As observed in Figure 4.19, linear regressions are suitable to represent both α_Z and α_T, but in a broader fibre volume fraction range a non-linear relationship is more likely in the transverse-fibre direction, according to Rolfes and Hammerschmidt [54], Pietrak and Wisniewski [55], and Bard et al. [56].

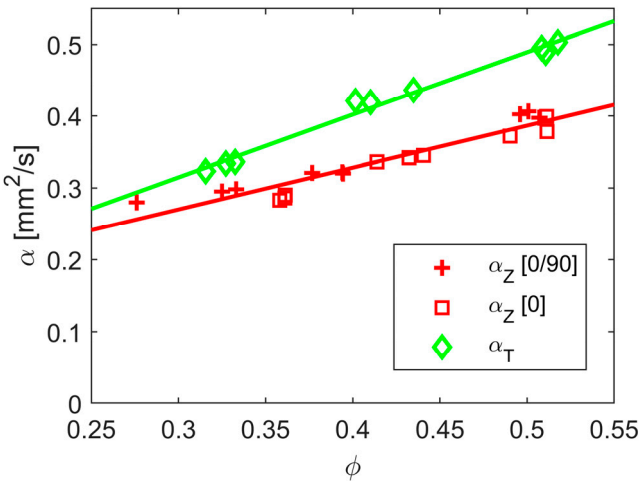

Figure 4.19. Thermal diffusivity components α_T and α_Z measured by LFA. Regressions: $\alpha_T = 0.8723\phi + 0.05293$ (green line) and $\alpha_Z = 0.5812\phi + 0.09571$ (red line). The measurements were conducted at 23°C. Reprinted from Paper III.

Figure 4.20 shows the measured values of α_L versus the fibre volume fraction, including the linear regression. Figure 4.21 shows the measured values of the specific heat capacity and the linear regression with respect to the fibre volume fraction. The regressions presented in Figure 4.19, Figure 4.20, and Figure 4.21 were used in Model I (Paper III).

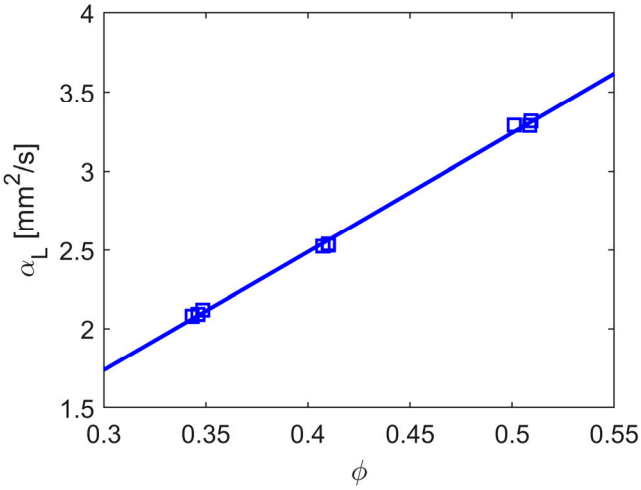

Figure 4.20. Thermal diffusivity component α_L measured by LFA. Regression: $\alpha_L = 7.52\phi - 0.5187$. The measurements were conducted at 23°C. Reprinted from Paper III.

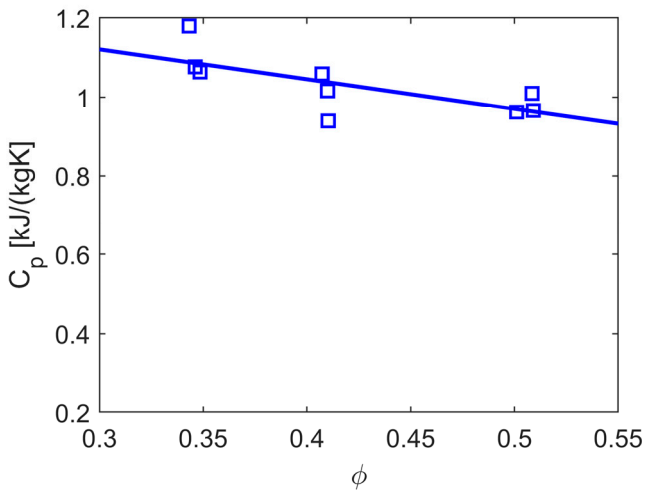

Figure 4.21. Heat capacity c_p measured by LFA. Regression: $c_p = -0.7565\phi + 1.348$. The measurements were conducted at 23°C. Reprinted from Paper III.

Figure 4.18 shows how the LFA samples were extracted from the woven CFRP plates. Due to the perpendicular fibre direction, it is impossible to measure either of the in-plane directions *T* or *L* directly from the samples. Since the composite is balanced, the *x*- and *y*-directional properties will equal each other on the macroscopic level, so the in-plane diffusivity in either *x*- or *y*-direction is further denoted α_X and the through-

thickness diffusivity is denoted α_Z. From the mentioned diffusivity components, the corresponding thermal conductivity components λ_X and λ_Z are calculated according to equation (4.17). To use Model I to predict the induction heating behaviour of the woven CFRP, it was necessary to approximate the thermal conductivity components λ_L and λ_T of the equivalent unidirectional layers, based on the measured value of λ_X. In the cross-ply representation of a woven CFRP ply the value of λ_L can be calculated according to the rule of mixtures relationship presented in equation (4.21), since the fibre conductivity λ_f and the matrix conductivity λ_m are known (see Table 4.1 and Table 4.2), as proposed in Paper IV. Due to the balanced bidirectional fibre layup the value of λ_X constitutes a mean value of λ_L and λ_T according to equation (4.22). Thus, the value of λ_T can be determined based on the measured value of λ_X and the value of λ_L, as proposed in Paper IV. The same approach was in Model III (Paper VII).

In the axisymmetric Model II, the thermal conductivity is represented by a radial component λ_R and a z-component λ_Z. This simplified representation requires that the radial thermal diffusivity is approximately independent of the in-plane direction. In CFRP with a high fibre volume fraction this is reasonable due to the expected rapid heat equalization between crossing tows within a ply, discussed in Paper VI. Thus, λ_R can be assigned the measured value of λ_X according to equation (4.23). This reasoning agrees with Zhang et al.[57], who found that the deviation of thermal conductivity between different in-plane directions of a woven CFRP was less than 5%. The mentioned study, Zhang et al.[57], was performed on woven CFRP samples made of the PAN fibre type T300 and an epoxy matrix, with a fibre volume fraction of 60 %, i.e. similar to the woven CFRP used in this thesis.

$$\lambda_L = \phi\lambda_f + (1-\phi)\lambda_m \tag{4.21}$$

$$\lambda_X = 0.5\lambda_L + 0.5\lambda_T \tag{4.22}$$

$$\lambda_R = \lambda_X \tag{4.23}$$

Figure 4.22 shows the measured diffusivities α_X and α_Z and the specific heat capacity c_p for the woven CFRP plates. In this case, the properties were measured with respect to both the fibre volume fraction and the temperature, in the 23–160°C range, for use in the temperature-dependent model (Model II). Equations for all the regressions in Figure 4.22 are presented in Paper VI. As in the characterization of unidirectional CFRP plates, there is a noticeable dispersion in the measurements of the specific heat

capacity. However, this is difficult to avoid when using the LFA method for measuring c_p, as was also observed by Joven and Minaie [53]. The solution is to do a large number of measurements to achieve a more reliable mean value. The in-plane component α_X shows a linear relationship to the fibre volume fraction which is not surprising since the dominant in-plane component λ_L has a linear relationship to the fibre volume fraction, also observed for the unidirectional samples (Figure 4.20). For the α_Z component, an exponential regression was used. Bard et al.[56] also observed an exponential relationship transverse the fibre direction. For both the diffusivity components and specific heat capacity, linear relationships to the temperature were observed.

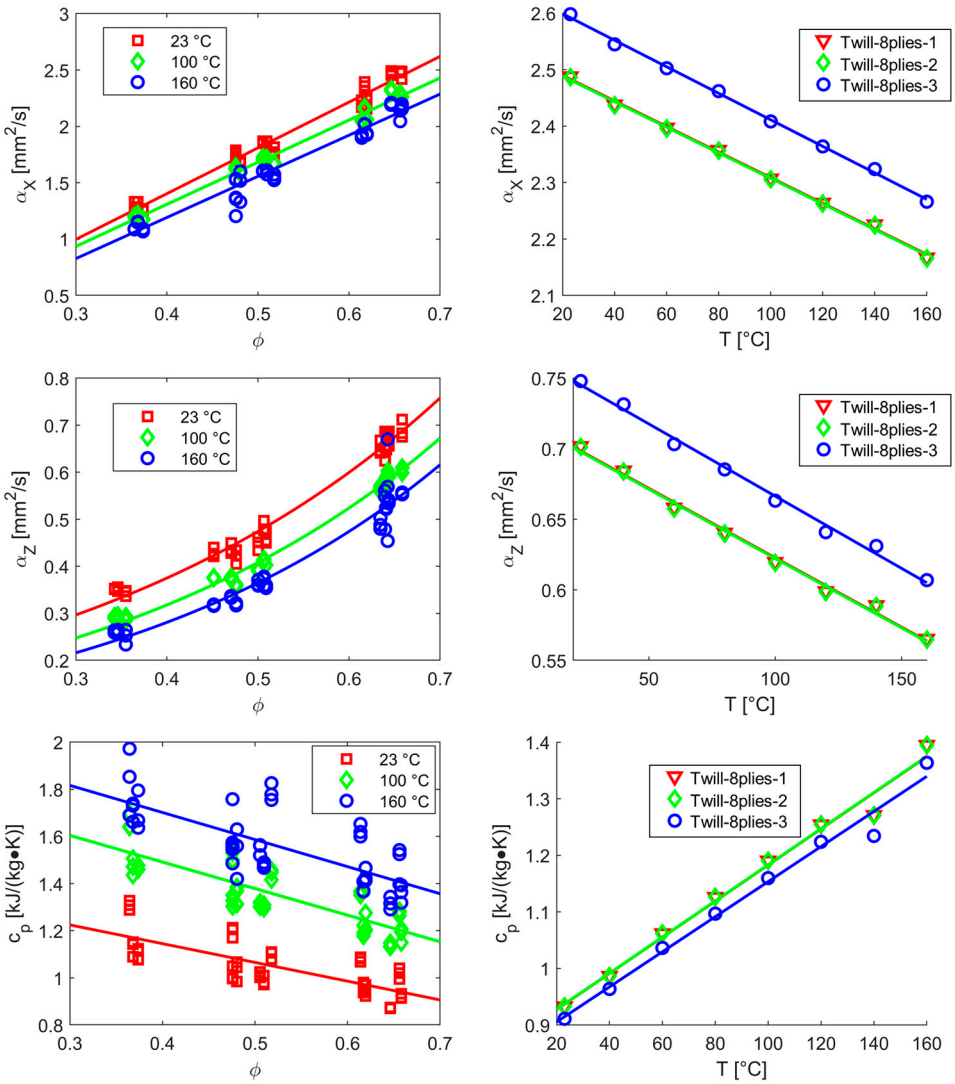

Figure 4.22. Thermal diffusivity and specific heat capacity for the twill-woven CFRP plates. The left-hand subfigures show the thermal properties as a function of the fibre volume fraction at three different temperatures. The right-hand subfigures show the thermal properties as a function of the temperature. The points are interpolated from the regressions presented in the left-hand subfigures. The equations for the regressions are presented in Paper VI. Adapted from Paper VI.

5 Temperature distribution during induction heating

Thermographic measurements were made during induction heating experiments and compared with the simulated temperature distributions. The temperature distribution is presented as the temperature increase ΔT from the starting temperature T_0 (approximately 21°C), according to equation (5.1). In some of the comparisons, the relative difference between the simulated and measured peak temperatures are presented, which is defined according to equation (5.2), where $\Delta T_{s\_max}(t)$ and $\Delta T_{m\_max}(t)$ are the simulated and measured surface peak temperatures, respectively, at time t from the initiation of induction heating. Each comparison of the surface temperature distribution is presented as a pair with a common temperature scale.

$$\Delta T = T - T_0 \tag{5.1}$$

$$\delta T_{max}(t) = \frac{\left|\Delta T_{s_{max}}(t) - \Delta T_{m_{max}}(t)\right|}{\Delta T_{m_{max}}(t)} \tag{5.2}$$

5.1 Characterization of temperature distribution

5.1.1 Temperature measurement methods

Two temperature measurement methods were used during the induction heating of CFRP: thermocouples and thermography.

5.1.1.1 Thermocouples

Temperature measurement with a thermocouple is based on the thermoelectric effect. Thermocouples could be integrated in the CFRP structure in order to measure the

internal temperature distribution, but since thermocouples are electrically conductive, the temperature may be affected by the induction heating, partly because the thermocouple itself will be heated by the induction and partly because the induced current may disturb the signal receiver. Integration of thermocouples may also disturb the electrical contact surfaces between fibres and thus influence the induction heating behaviour. By using a sufficiently small thermocouple, the influence of direct induction heating is negligible in most cases. With a careful arrangement of the setup, twisted pair cables, proper shielding, and a thermocouple transducer that is not very sensitive to disturbances, reliable measurements are feasible, although they might be challenging.

5.1.1.2 Thermography

This method is used to measure the temperature distribution of a surface. The heat loss due to the thermal radiation $\mathbf{q}_r$ from a surface is described by the Stefan–Boltzmann law, equation (3.11).

5.1.2 Experimental setup for thermographic measurement

The temperature distribution was measured using the FLIR T-540 thermographic camera. The setup for thermographic recording is shown in Figure 5.1. The coil is the same as presented in Figure 3.1. The effective value of the coil current was measured with the Rogowski coil PEM CWT. The coil current was generated by a frequency inverter connected to the induction coil according to the illustration in Figure 2.5. No flux concentrator was used, thus simplifying the modelling of the setup. Before thermographic measurements, the surfaces of the CFRP plates were painted matte black to obtain a surface with known emissivity and to reduce reflections from the surrounding environment. The internal temperature gradients could not be measured, since the presence of internal temperature sensors would distort the induction heating. The validation of the simulation models is based on thermographic recordings of the surface temperature distribution on the CFRP plates.

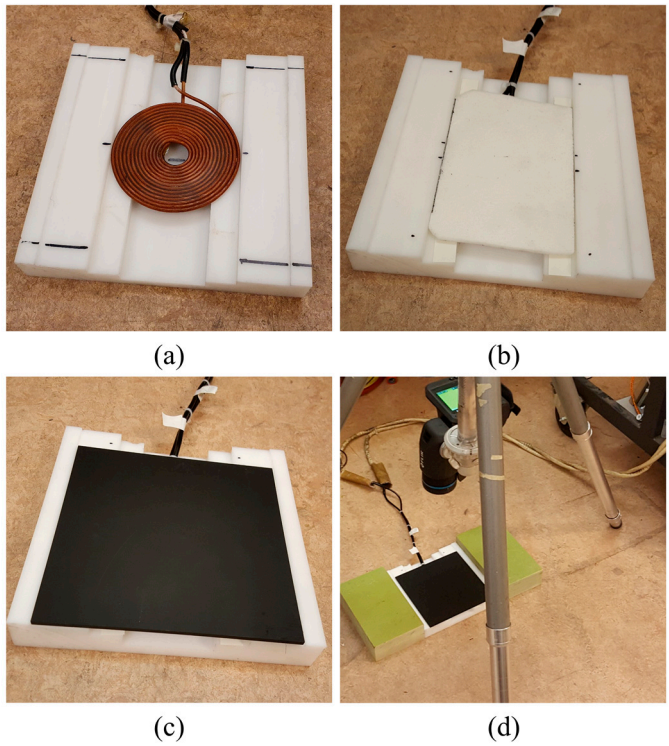

Figure 5.1. Experimental setup for thermographic recording during induction heating. (a) The 14-turn induction coil (the same coil as shown in Figure 3.1) placed in the coil holder. (b) A thermal insulation sheet placed above the coil in order to minimize conductive heating from the ressistive losses in the coil. (c) A black-painted CFRP plate placed above the coil. (d) The surface of the CFRP plate is recorded using a thermographic camera during induction heating. Reprinted from Paper III.

During the induction heating experiments, the CFRP plate surface opposite the coil is denoted the “front surface” and the surface closest to the coil is denoted the “coil surface”, as illustrated in Figure 5.2.

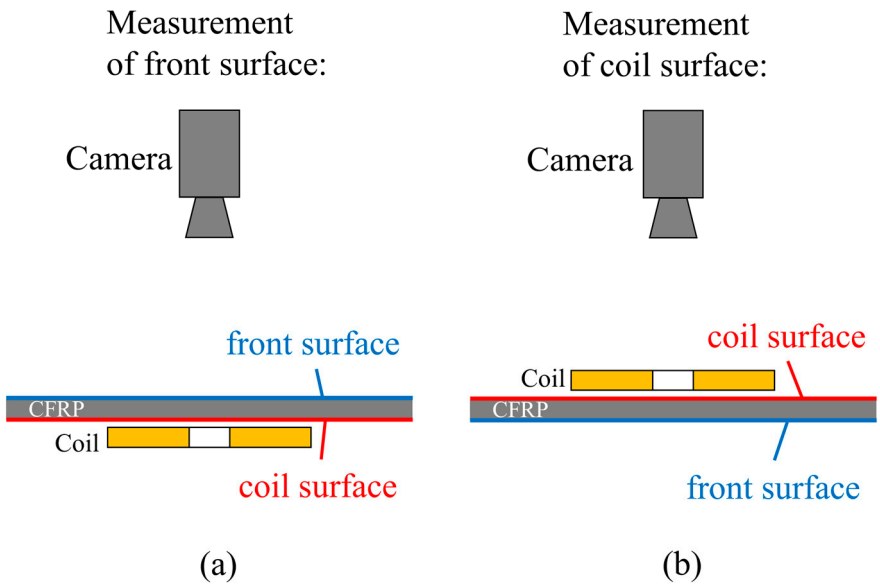

Figure 5.2. Schematic illustration of the experimental setup for recording the CFRP plate surface temperature distribution during induction heating. (a) Illustration of the setup when recording the "front surface" temperature. (b) Illustration of the setup when recording the "coil surface" temperature. The coil surface of the plate cannot be recorded until the coil has been removed. Reprinted from Paper VII.

5.1.3 Emissivity measurement

To characterize the emissivity ε, thermocouples were glued to one surface of an aluminium cuboid, and then the surface was painted with the same black paint as used for the CFRP plates. The cuboid, shown in Figure 5.3 (a), was heated in an oven to a uniform temperature just above 120°C, after which it was removed from the oven to room temperature conditions. The thermal radiation emitted by the surface was recorded by the thermographic camera, simultaneously as the thermocouple temperatures were recorded. Figure 5.3 (a) shows the painted surface of the aluminium cuboid with the mounted thermocouples. Figure 5.3 (b) shows a thermographic image of the surface. The high thermal diffusivity of aluminium enables the maintenance of a uniform temperature distribution on the surface. The positions of the thermocouples are indicated in the thermographic image. The emissivity was determined so that the mean temperature T_{IR} of the highlighted square region between the thermocouples agreed with the thermocouple measurements. Figure 5.4 shows the temperature curves measured by the two thermocouples and the values of T_{IR} based on different emissivity settings between 0.91 and 0.95. Since the thermographic temperature curve corresponding to an emissivity of 0.93 (blue curve) lies between the two thermocouple

curves, it is reasonable to state that the emissivity is approximately 0.93. This value was used in Papers IV, VI, and VII. During the work with Paper III, the emissivity was determined to be 0.95.

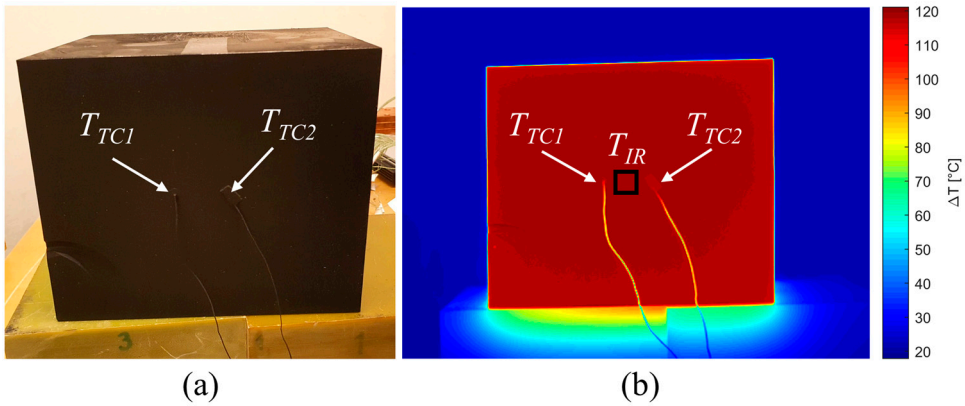

Figure 5.3. The setup for measuring the emissivity ϵ. (a) A photography of the painted aluminium cuboid showing the positions of the mounted thermocouples. (b) A thermographic image of the painted surface showing the thermocouple measurement points. The corresponding thermographic temperature to be compared with the thermocouple-measured temperature is calculated as the mean temperature value within the the black square (T_{IR}) indicated between the two thermocouple positions.

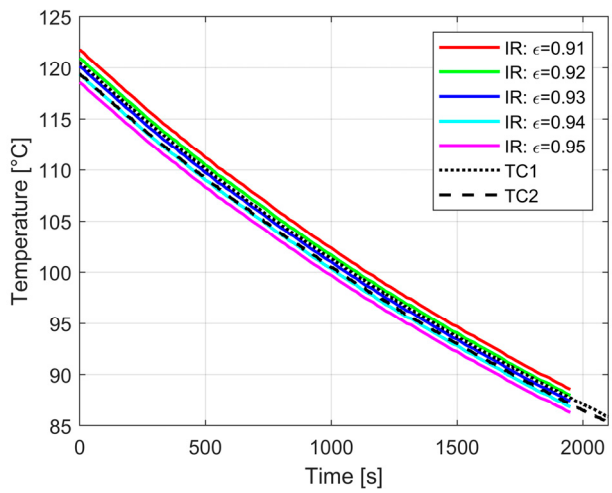

Figure 5.4. Based on the recorded thermal radiation five different temperature curves were calculated based on five emissivity values (0.91-0.95). The temperatures measured by the thermocouples are presented as a dotted and a dashed line. The emissivity 0.93 resulted in a temperature curve with best agreement with the mean value temperature measured by the thermocouples.

5.2 Input power and heating efficiency

The input power P_{CFRP} induced in a CFRP plate during induction heating can be calculated from the frequency dependent coil resistance ΔR_m and the coil current according to equation (4.10). The value of the coil resistance ΔR_m at the heating frequency for each plate are presented in Table 5.1 and Table 5.2. The frequency 60 kHz was used in all cases except for the heating of plate 24-4 and 32-4. In those two cases high current levels (140 and 80 A) were necessary to compensate for the low value of ΔR_m. A consequence of the high current levels was that the VFD automatically adjusted the frequency downwards to try to find a frequency closer to resonance. The level of the coil resistance R_{coil0} (coil resistance when no conductive plate is near the coil) in the range 50-60 kHz was 0.032 Ω. These values were used to determine the coil current required to achieve a certain input power P_{CFRP}. Also the heating efficiency according to equation (4.11) is presented. Temperature dependent material properties were only used in Model II. Therefore, during validation of Model I (Paper III and IV) a temperature increase below ΔT = 30°C (from room temperature) was aimed for in order to be able to neglect temperature dependencies of the materials. The results from Paper VI showed that within such a moderate temperature increase the temperature dependence is not significant.

Table 5.1. Heating frequency, measured ΔR of the coil and calculated heating efficiency for the cross-ply CFRP plates. The distance between coil and CFRP plate is 4 mm.

Plate ID	Frequency [kHz]	ΔR_m [Ω] at the specified frequecy	Heating efficiency η (equation (4.11))
24-4	54	0.02	0.36
24-8	60	0.08	0.72
24-12	60	0.13	0.80
24-24	60	0.21	0.87
32-4	58	0.06	0.65
32-8	60	0.22	0.87
32-16	60	0.34	0.91
32-32	60	0.45	0.93
40-4	60	0.21	0.87
40-10	60	0.51	0.94
40-20	60	0.54	0.94
40-40	60	0.57	0.95

Table 5.2. Heating frequency, measured ΔR of the coil and calculated heating efficiency for the twill woven plates. The distance between coil and CFRP plate is 3.8 mm.

Plate ID	Frequency [kHz]	ΔR [Ω]	Heating efficiency η (equation (4.11)
Twill-4plies-1	60	0.39	0.93
Twill-5plies-1	60	0.52	0.95
Twill-6plies-1	60	0.58	0.95
Twill-7plies-1	60	0.68	0.96
Twill-8plies-1	60	0.74	0.96
Twill-8plies-2	60	0.73	0.96
Twill-8plies-3	60	0.73	0.96

5.3 3D finite element model (Model I)

5.3.1 Cross-ply CFRP

During the induction heating experiments with the cross-ply plates, the coil current in each case was selected to achieve an input power P_{CFRP} of approximately 400 W. In each case the heating duration was 2 s. The input power was gradually ramped up to the stationary reference level, as shown in Paper III. The measured current curve for each case was used in the simulation. The coil current and input power for each case is presented in Table 5.3.

Table 5.3. Stationart coil current and corresponing input power P_{CFRP} during the induction heating experiments with the cross ply plates, Paper III.

Plate ID	Coil current [A] (stationary level)	P_{CFRP} [W] (stationary level)
24-4	140	354
24-8	74	444
24-12	57	421
24-24	45	429
32-4	80	377
32-8	45	441
32-16	36	439
32-32	31	435
40-4	45	425
40-10	29	432
40-20	29	458
40-40	28	446

To explain the measured and simulated temperature distributions, first the simulated temperature and heat distributions in one of the cross-ply CFRP plates are analysed and discussed. Figure 5.5 shows the simulated front surface temperature of plate 40-4 at the time of 6 s. The induction heating duration was 2 s; thus the image represents

the surface temperature distribution 4 s after heating completion. To explain the pattern of the temperature distribution, it is necessary to understand how the induced current circulates inside the plates. For this purpose, Figure 5.6 shows the internal power distributions and temperature distribution for the three cross-sectional planes indicated with dashed red lines in Figure 5.5. The upper row of images in Figure 5.6 shows the induced power distribution Q [W/m^3] and the second and third row show the temperature distribution ΔT at 2.1 s (just after induction heating completion) and at 6 s respectively. In each of the cross section images the cross section between the unidirectional layers are marked with white dashed lines. The two outer layers are x-directional (fibres along the x-axis) with the electrical and thermal conductivity tensors, σ_x and λ_x (equation (3.19) and (3.21)) and the two inner layers are y-directional with the electrical and thermal conductivity tensors, σ_y and λ_y (equation (3.20) and (3.22)).

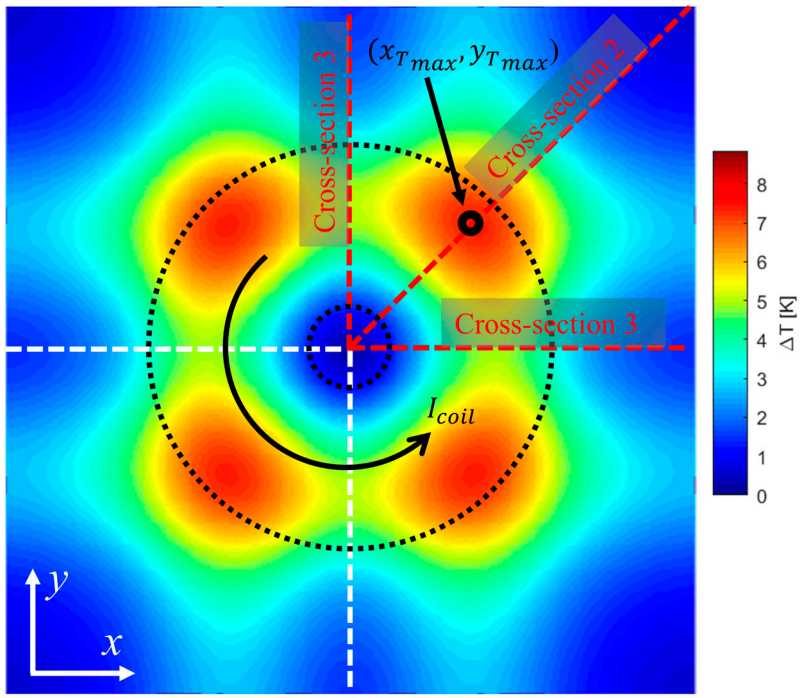

Figure 5.5. Simulated front surface temperature distribution of plate 40-4 at the 6 s timestamp. The heating duration is 2 s, with an effective coil current of 45 A (stationary level) and a frequency of 60 kHz. The temperature is presented as the temperature increase ΔT from the start temperature T_0. The vertical and horisontal dahsed lines indicate the symmetry planes and the black dotted circles indicate the inner and outer outlines of the induction coil. The black circle arrow indicates the coil current direction. The red dashed lines indicate the cross-sectional planes for which the internal distributions are plotted in Figure 5.6.

The coil, parallel with the plate, induces a circulating electric field that gives rise to a circulating current. The induced current passes normal to the vertical and horizontal

symmetry lines, shown in Figure 5.5. Since the induced current wants to take the path of least resistance, the current mainly flows in the two inner *y*-directional layers when it passes through plane 1 and in the two outer *x*-directional layers when it passes through plane 3. This results in a concentration of heating power in the two outer layers of cross section 3 and in the inner layers of cross section 1. In order to obtain the circulating path of least resistance, the current therefore needs to pass between *x*-directional and *y*-directional layers in each quadrant. Due to the low electrical conductivity along the *z*-axis, σ_Z, this transition results in a higher heat dissipation, resulting in the four surface temperature peaks observed in Figure 5.5, one in each quadrant. The position of the temperature surface maximum in the upper right quadrant is denoted (x_{Tmax}, y_{Tmax}, z_{Tmax}). The white vertical arrows in the images of cross section 2 indicate the line along which the internal heat and temperature distribution is presented in Figure 5.7.

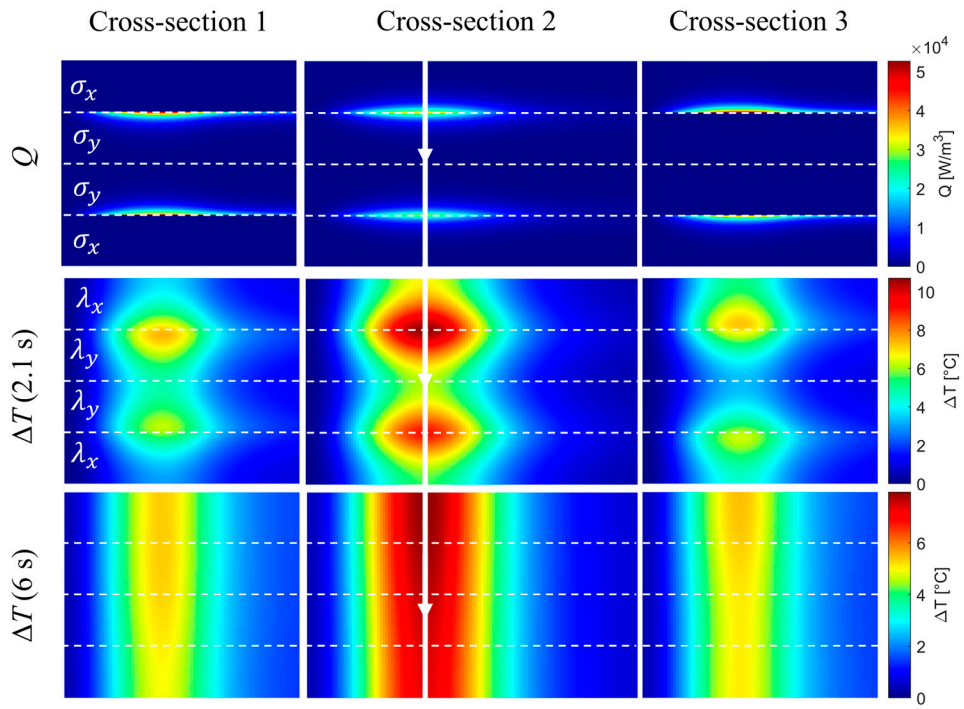

Figure 5.6. Simulated through-thickness power distribution and temperature distribution at two timestamps (2.1 s and 6 s) for three cross-sections of plate 40-4. The cross section between unidirectional layers are marked with white dashed lines. The two outer layers are x-directional and the two inner are y-directional. The electrical and thermal conductivity tensors for each of the four layers are indicated in the left subfigures. The power density *Q* is calculated for the effective coil current 1 A while the temperatures are calculated for the coil current 45 A.

To compare the simulated internal gradients of all the plates, the temperature distribution and induced power distribution through the thickness (z-direction) of each plate were presented for the vertical line at the in-plane position (x_{Tmax}, y_{Tmax}), i.e., along the white arrow indicated in cross-section 2 in Figure 5.6. The results are presented in Figure 5.7. For each plate, the relative power distribution Q/Q_{max} is presented (Q_{max} is the peak value along the line). Also, the temperature distributions at the 2.1 s, 4 s, and 6 s timestamps are presented. The vertical black lines indicate the interfaces between the unidirectional layers. As shown in Figure 5.6 and Figure 5.7, the induced power is highly concentrated at the interfaces between the perpendicular crossing unidirectional layers. In the thick-layer plates the induced heating power becomes concentrated in a few interfaces, but in the thin-layer plates, the induced heating power will be distributed among many interfaces through the thickness. No heat generation peak is present between the two inner layers since they have the same fibre direction. In summary, the heat generation is highly concentrated to the layer interfaces but the temperature equalizes rapidly within and between layers.

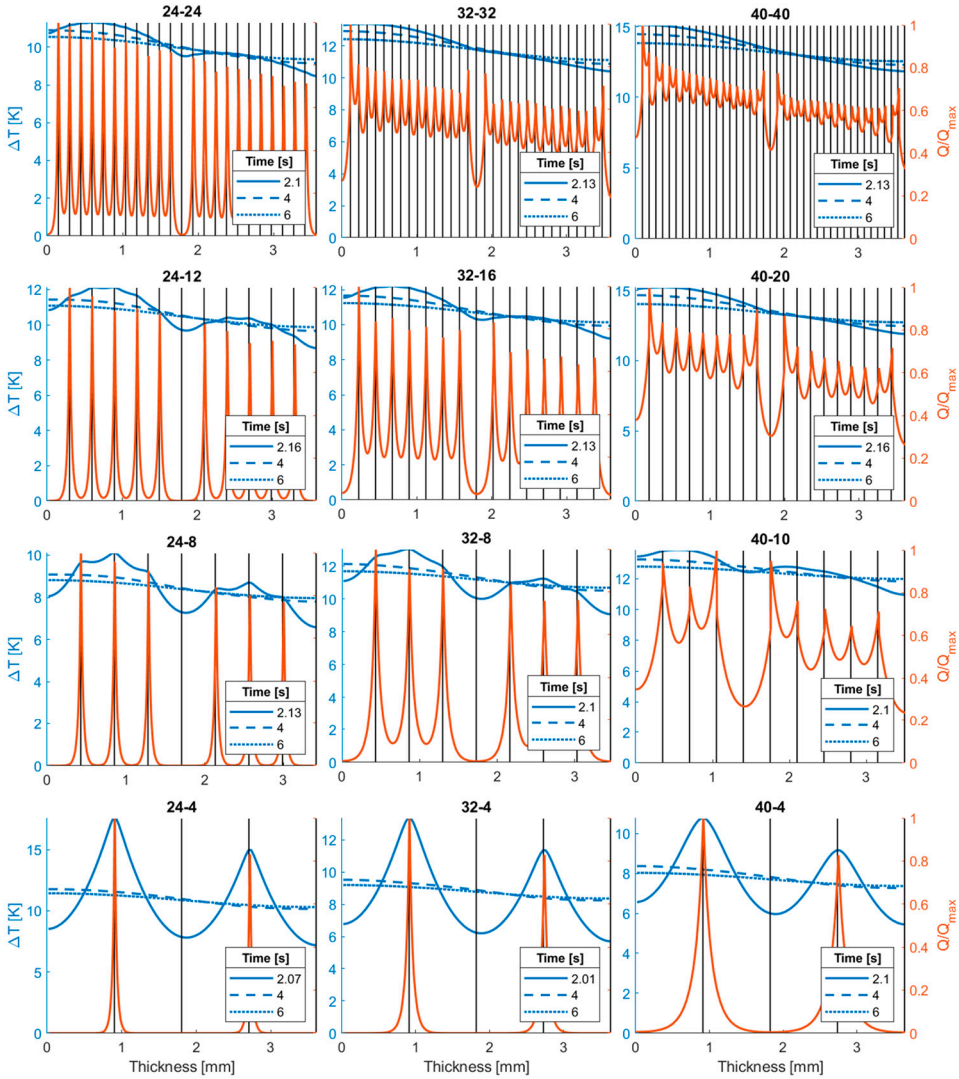

Figure 5.7. Simulated internal power distribution and temperature distribution thorugh thickness at (x_{Tmax}, y_{Tmax}). The red curves presents the relative power distribution Q/Q_{max} (Q_{max} is the peak value along the line). The blue curves presents the temperature distribution at three different timestamps. Adapted from Paper III.

The simulation results presented in Figure 5.6 and Figure 5.7 are based on a simulation model with a homogeneous layer representation of the composites structure and it is therefore difficult to assess the magnitude of the internal heat generation peaks. However, due to the small width of the peaks, and the short distance between them, the temperature variations within the layers equalizes rapidly. Equation (3.16) presents an approximation of the time for a temperature difference to significantly equalize over

a certain distance in one dimension. A one-dimensional analysis is a reasonable approximation when analysing the through thickness temperature gradients. As can be seen in Figure 5.7 the largest distance between a local heat generation maximum and minimum is the thickness of a layer d_{UD}; in the two inner layers and in the outer layers.

Table 5.4 presents a comparison of the temperature equalization time τ over the distance d_{UD}. The distance d_{UD} was selected to compute a worst case, in the centre of the plates; most of the temperature maximums and minimums are separated only by a distance of $d_{UD}/2$, se Figure 5.7. The value of τ presented in the middle column is based on the value of α_Z presented in Figure 4.19 (cross-ply CFRP) and Figure 4.22 (woven CFRP), which is the macroscopic values obtained from the LFA measurements. However, due to local variations in the fibre distribution the thermal diffusivity may be significantly lower locally between two fibre tows. Therefore, a worst case scenario is also presented where the temperature equalization time is calculated based on the diffusivity of the matrix material α_m. No matter if the temperature equalization time is calculated based on α_Z or α_m it is observed that most of the plates have equalization time τ significantly under 1 s over the distance d_{UD}; only plates with the thickest layers (for example 24-4 with a layer thickness of approximately 1 mm) have equalization times above 1 s.

Table 5.4. This table presents a comparison of the approximate temperature equalization time between two unidirectional layers or tows, according to equation (3.16), for the distance d_{UD}. The centre column presents the temperature equalization time τ based on the macroscopic fibre volume fraction dependent value of α_Z presented in Figure 4.19 (cross-ply plates) and Figure 4.22 (twill plates). The right column presents the value of τ for the worst case when no fibres are present and the diffusivity equals the diffusivity of the matrix material α_m.

Plate ID	$\tau(\alpha_z, d_{UD})$	$\tau(\alpha_m, d_{UD})$
24-4	1.54 s	2.63 s
24-8	0.34 s	0.59 s
24-12	0.17 s	0.29 s
24-24	0.04 s	0.07 s
32-4	1.34 s	2.67 s
32-8	0.30 s	0.61 s
32-16	0.08 s	0.16 s
32-32	0.02 s	0.04 s
40-4	1.10 s	2.71 s
40-10	0.16 s	0.40 s
40-20	0.04 s	0.11 s
40-40	0.01 s	0.03 s
Twill-4plies-1	0.29 s	0.64 s
Twill-5plies-1	0.14 s	0.39 s
Twill-6plies-1	0.09 s	0.30 s
Twill-7plies-1	0.05 s	0.21 s
Twill-8plies-1	0.04 s	0.19 s
Twill-8plies-2	0.04 s	0.19 s
Twill-8plies-3	0.04 s	0.17 s

The value of the temperature equalization time τ over a certain distance Δz can be used to estimate the relative severeness of local temperature peaks during induction heating. Figure 5.8 illustrates a number of temperature peaks in one dimension, z. We are interested in approximating the stationary magnitude of ΔT_{peak} at a certain local input power density Q_{ind} [W/m^3], in relation to the surrounding temperature increase during induction heating. In this calculation we assume a periodic pattern where each T_1 domains is surrounded by T_2-domains and each T_2 domain is surrounded by T_1 domains. The problem is simplified so that the temperatures T_2 and T_1 are represented with domains with the thickness Δz. According to the heat equation, discretized, the heating power per volume unit flowing into the T_1-domain is according to equation (5.3), i.e. the conductive heat transfer to the domain due to the temperature difference ΔT_{peak}, illustrated in Figure 5.8. The heat power per volume unit flowing into the T_2-domains is according to equation (5.4), i.e. the induced power Q_{ind} minus the heat power flowing in to the neighbouring T_1-domains due to the heat conduction. When the amplitude of ΔT_{peak} has reached a certain level, Q_1 will equal Q_2 according to equation (5.5), thus the temperatures T_1 and T_2 will increase with the same rate, resulting in a constant value of ΔT_{peak}. Thus, ΔT_{peak} will be according to equation (5.6). The temperature of T_1 at time t of heating is according to equation (5.7). Consequently, the ratio between the local peak amplitude ΔT_{peak} and the increase of T_1 during the time t can be determined according to equation (5.8). For example if the temperature equalization time τ is 0.1 the temperature of the local heat generation peak will be significantly higher relative to its surrounding after 0.1 s of heating. However, after 10 seconds the temperature at the heat generation peak will account just for approximately 1% of the minimum temperature increase during the heating time. Consequently, during moderate heating rates, local temperature peaks will be insignificant although the heat generation peaks have high gradients. After the heating completion the temperature peak will equalize significantly within the time τ. The three-dimensional anisotropic case is of course more complex, but still the value τ provides a simple method to estimate the significance of internal temperature peaks or temperature variation within the composite structure at a certain heating time.

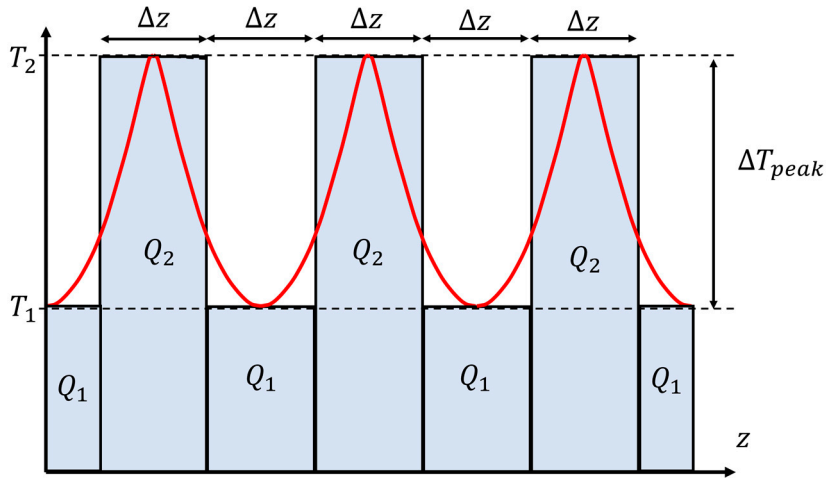

Figure 5.8. A periodic temperature curve is dicretized, defined by the peak temperature T_2 and the minimum temperature T_1. Each step has the width Δz, which consequently is also the distance between a maximum and minimum.

$$Q_1 = 2\lambda_Z \frac{\Delta T_{peak}}{\Delta z^2} \tag{5.3}$$

$$Q_2 = Q_{ind} - 2\lambda_Z \frac{\Delta T_{peak}}{\Delta z^2} = Q_{ind} - Q_1 \tag{5.4}$$

$$\mathrm{Q}_1 = Q_2 \;\Rightarrow Q_{ind} = 2Q_1 \Rightarrow Q_{ind} = 4\lambda_Z \frac{\Delta T_{peak}}{\Delta z^2} \Rightarrow \tag{5.5}$$

$$\Rightarrow \Delta T_{peak} = \frac{\Delta z^2 Q_{ind}}{4\lambda_Z} = \frac{\Delta z^2 Q_{ind}}{4\alpha_Z \rho c_p} = \tau \frac{Q_{ind}}{2\rho c_p} \tag{5.6}$$

$$T_1(t) = T_1(0) + t\frac{Q_1}{\rho c_p} \tag{5.7}$$

$$\frac{\Delta T_{peak}}{T_1(t) - T_1(0)} = \frac{\tau \frac{Q_{ind}}{2\rho c_p}}{t\frac{Q_1}{\rho c_p}} = \frac{\tau \frac{Q_{ind}}{2\rho c_p}}{t\frac{Q_{ind}}{2\rho c_p}} = \frac{\tau}{t} \tag{5.8}$$

To evaluate the models, the simulated surface temperatures were compared with the measured surface temperatures. Figure 5.9 shows how the front surface temperature distribution of the cross-ply plate 32-16 changes over time during induction heating. In the comparison at the 1 s timestamp both the simulation and measurement show a temperature pattern with four significant hot regions, but with a significant difference regarding peak temperature. The measurement also shows high local gradients which indicates a difference in the internal heat generation distribution between simulation and measurement. To understand the difference in pattern and temperature level the images of the fibre structure presented in Figure 4.1, should be recalled. The internal fibre structure of plate 32-16 is obviously not perfectly homogeneous, nor is the internal fibre structure of the other plates. This means that the measured induced power distribution will differ from the simulated one. However, some seconds after heating completion, the simulated and measured surface temperature distribution converges which indicates that the model provides a good prediction of the mean value of the through thickness temperature distribution. This model is not suited for prediction of local internal heat generation gradients but instead has its potential to effectively predict a macroscopic temperature distribution.

A systematic validation of the model for the different CFRP plates, using thermography, should therefore be performed in either of the mentioned cases; during long heating time or after heating completion. To minimize the influence from convection and temperature dependence the heating time was limited to 2 seconds and the input power limited to achieve a local temperature increase of 15 °C or lower. Due to the short heating time it was not a good option to do the systematic evaluation based on thermographic images captured during the heating phase. Instead, the evaluation was made based on recordings and simulated surface temperature distributions at the timestamp 6 s (i.e., 4 s after heating completion). Another reason for using the timestamp 6 s was to make it possible to evaluate the temperature distribution of the coil surface (the CFRP surface closest to the induction coil), since it can be recorded first when the coil has been removed.

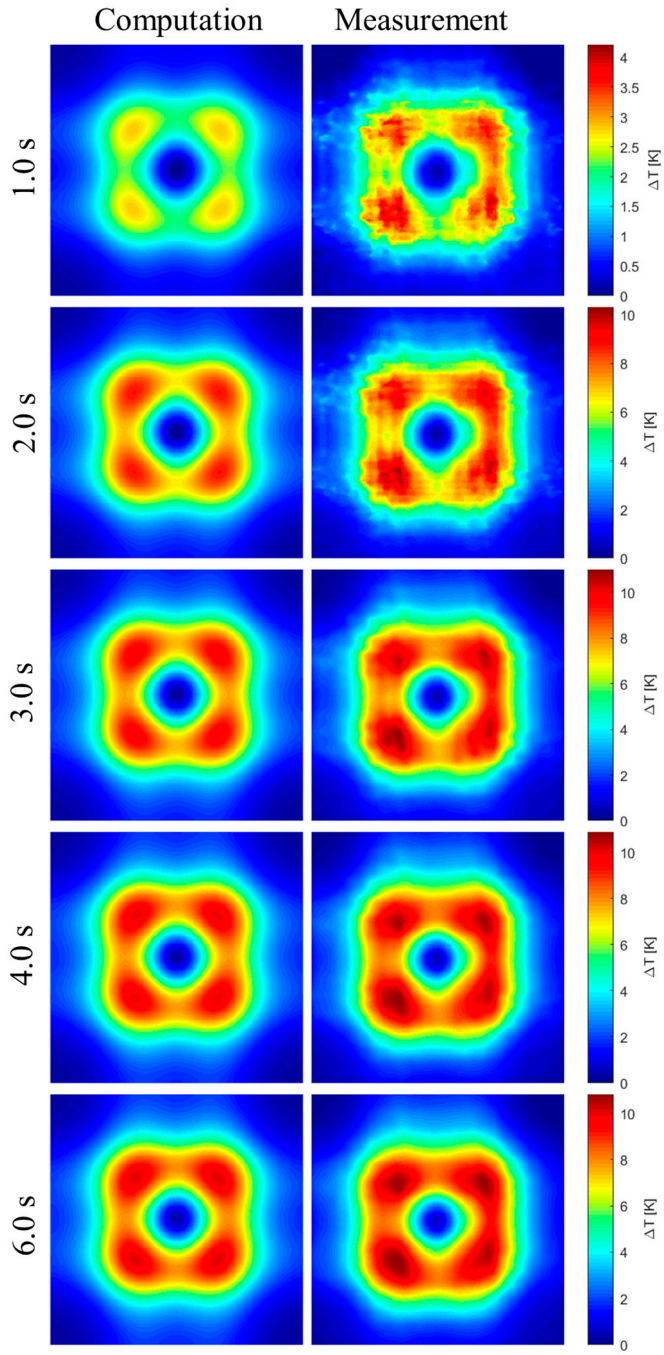

Figure 5.9. The figure shows the front surface temperature distribution for plate 32-16 at different times during induction heating and after induction heating completion. The induction heating time was 2 s. Adapted from Paper III.

Figure 5.10 and Figure 5.11 show the simulated and measured "front surface" and "coil surface" temperature distributions, respectively, for all cross-ply CFRP plates at the 6 s timestamp. The temperature distribution image pairs are arranged so that the rows represent plates with the same numbers of fabric plies, and therefore approximately the same fibre volume fractions, but with different unidirectional layer thicknesses. The rows are ordered from top to bottom with increasing number of plies. The farther right in the columns, the thinner the plate layer thickness. For each temperature distribution comparison also a value $\delta T_{\max}$ is presented which indicates the relative difference in surface peak temperature between simulation and measurement according to equation (5.2). It can be observed that the temperature distribution tends towards a more axisymmetric pattern as the fibre volume fraction increases and the layer thickness decreases which can be explained as follows. A reduced fibre volume fraction leads to higher resistance to the induced circulating current crossing the perpendicular layers (see the exponential relationship between fibre volume fraction and σ_Z in Figure 4.8 and Figure 4.9). Also, thicker layers result in a longer mean distance for the current to travel between perpendicular layers, thus in higher resistance. A higher contact resistance between layers results in a more square-shaped temperature distribution pattern due to the increasing heat generation when the current flows between perpendicular layers. The opposite case, i.e., decreasing layer thickness and increasing fibre volume fraction, leads to a more circular temperature distribution, henceforth referred to as "isotropic behaviour". For the case with an axisymmetric coil parallel to a CFRP plate, the isotropic behaviour means that the heating results in an approximately axisymmetric heat generation and thus axisymmetric temperature pattern.

Regarding the difference between front surface and coil surface it can be concluded that the difference is relatively small which is due to the fact that the electromagnetic skin depth is significantly larger than the thickness of the plates. The definition of the electromagnetic skin depth, equation (2.2), is for isotropic materials but based on Paper VI the value of the equivalent electrical conductivity will be not higher than 24 kS/m in any of the plates in this study (based on the fibre volume fraction). This results in a skin depth of minimum 13 mm which is significantly thicker than the plates.

The absolute difference between the simulated and measured temperature distributions is generally larger for plates with low fibre volume fractions and thick unidirectional layers. Regarding the fibre volume fraction, it can be observed in the microscopy images (Figure 4.1 and Figure 4.2) that a low fibre volume fraction results in a more heterogeneous structure with distinct fibre-rich and resin-rich regions, creating a significant difference from the homogeneous representation. The higher the fibre volume fraction, the better the electrical conductance between crossing layers, and thus

less distinctive local heating power peaks when the current travels between crossing layers. A higher fibre volume fraction also results in higher thermal diffusivity and thus faster equalization of local temperature peaks.

Another aspect of the layer thickness is that in the case with thick layers the induced heating power is concentrated to only a few interfaces while in the case with many thin layers the heating power will be distributed through the thickness in many interfaces between crossing layers. For example in the plates with only four layers (24-4, 32-4 and 40-4) the induced heat generation is concentrated to only two interfaces which means that the local non-homogeneous imperfections in these interfaces will have a huge impact on the resulting induced power distribution. On the other hand, during heating of plate 40-40 the heating is distributed to 38 interfaces distributed through the thickness, which means that local deviations will not have the same impact on the mean temperature after equalization of temperature peaks. In summary, the model provides a better prediction of the surface temperature distribution in plates with higher fibre volume fractions and thinner layers, both with respect to pattern and peak temperature.

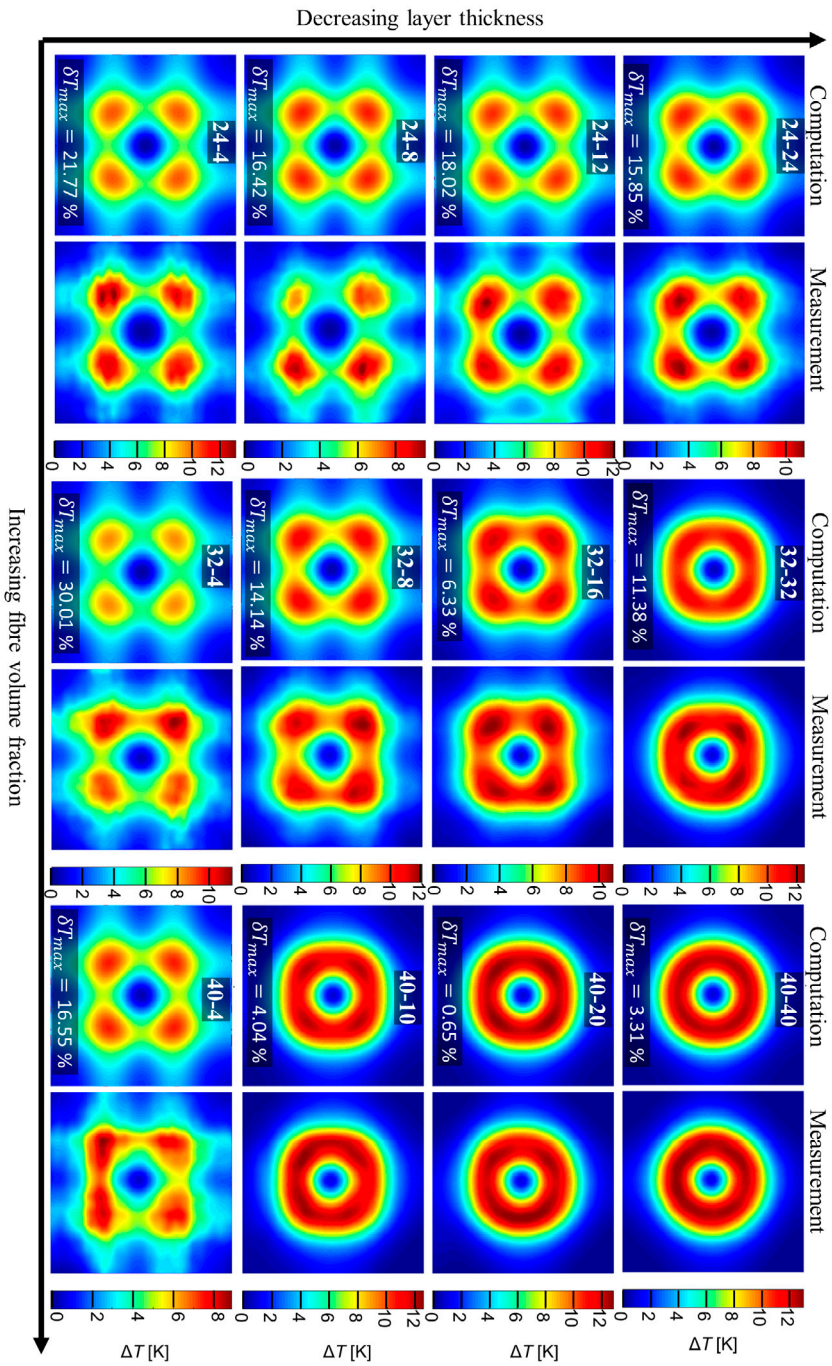

Figure 5.10. The front surface surface temperature distribution at the 6 s timestamp for the cross-ply CFRP plates. The figure is rotated 90° and the font size in the scales are increased compared to the orginal figure presented in Paper III. Adapted from Paper III.

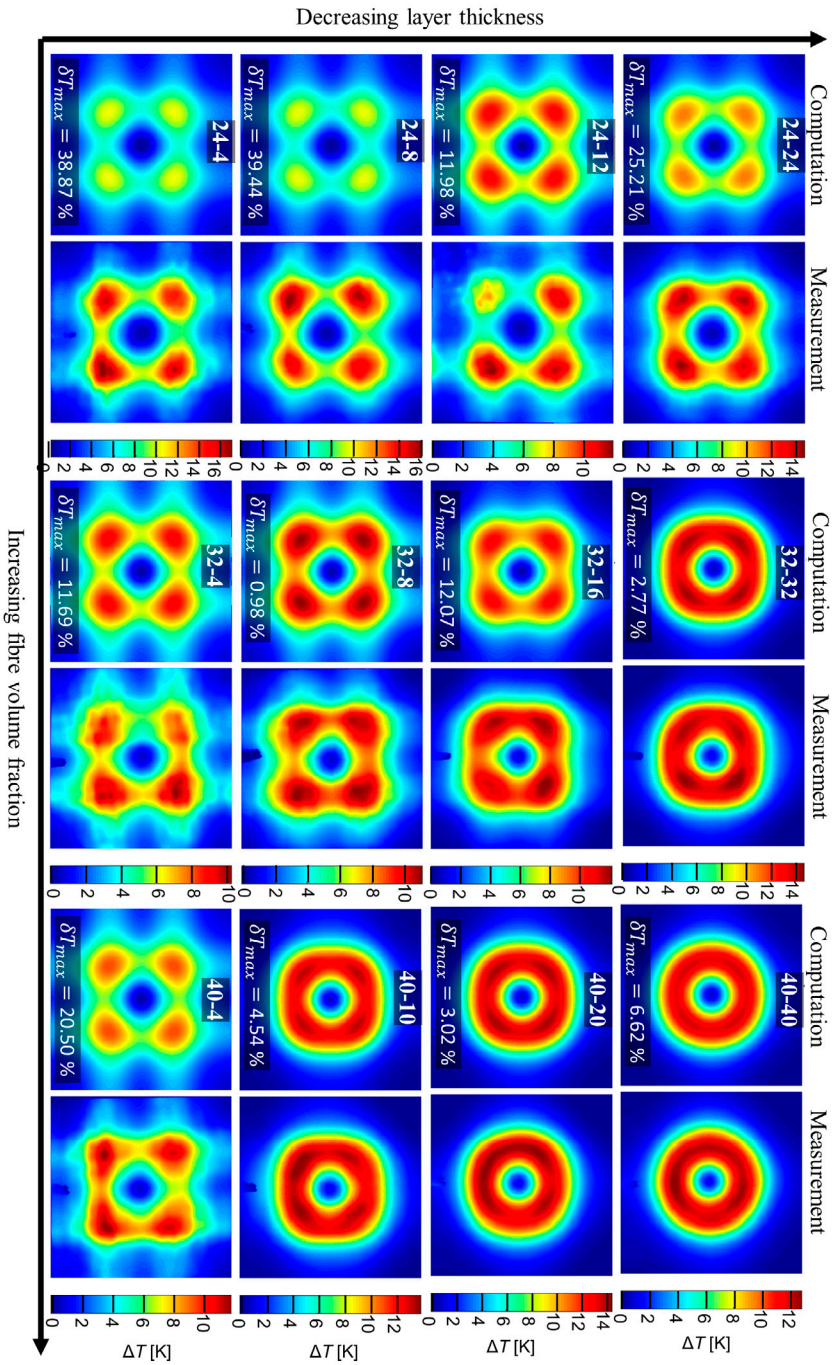

Figure 5.11. The coil surface temperature distribution at the 6 s timestamp for the cross-ply CFRP plates, The figure is rotated 90° and the font size in the scales are increased compared to the orginal figure presented in Paper III. Adapted from Paper III.

5.3.2 Woven CFRP

Model I was also used for predicting the temperature distribution in woven CFRP plates. Five woven CFRP plates were used to validate the model. Table 5.5 shows the current selected in each case to achieve a constant input power P_{CFRP} of about 400 W (same as for the experiments with the cross-ply plates). The frequency 60 kHz was used in all cases and the current was constant through the whole induction heating duration of 4 s.

Table 5.5. Effective coil current and heating power P_{CFRP}, according to equation (4.10), during the experiments with the twill woven CFRP plates. The coil current in each case was at a constant level during the whole heating.

Plate ID	Coil current [A]	P_{CFRP} [W]
Twill-4plies-1	33	426
Twill-5plies-1	29	437
Twill-6plies-1	27	424
Twill-7plies-1	25	429
Twill-8plies-1	23	389

Figure 5.12 shows a comparison between measurement and simulated front surface temperature distribution for plate Twill-6plies-1. Like for cross-ply plates the simulated and measured temperature distribution do not agree very well in the initial phase (0.5 s) of the heating but continuously converges. As discussed in the chapter 3 the usage of the cross-ply model for representing woven CFRP is based on a rapid temperature equalization between crossing plies. As presented in Table 5.4, the temperature equalization time τ between crossing tows in plate Twill-6plies-1 is approximately 0.09 s (maximum 0.30 s in a resin rich region) which is based on a mean distance $\Delta z = d_{UD}$. Therefore it is reasonable that the measured and simulated surface temperature distribution converges continuously during a heating time of 4 s. Image-times-series for the rest of the plates are presented in Paper IV. Figure 5.13 shows temperature distribution comparisons for five woven CFRP plates with different fibre volume fractions. The left column shows temperature image pairs representing the "front surface", and the right column shows temperature distribution pairs representing the "coil surface". For the plate with lowest fibre volume fraction (Twill-4plies-1) it is observed that the measured temperature peaks are higher than the simulated, but still provides a good prediction of the temperature distribution pattern. The tendency that a lower fibre volume fraction leads to worse agreement between simulation and measurement also agrees with the tendency observed for the cross-ply plates; lower fibre volume fraction leads to a more heterogeneous structure, thus agrees less well with a homogeneous representation. However, these results show that the cross-ply finite element model (Model I) provides as good a prediction of the temperature of woven CFRP as of cross-ply plates, in terms of both pattern and surface peak values.

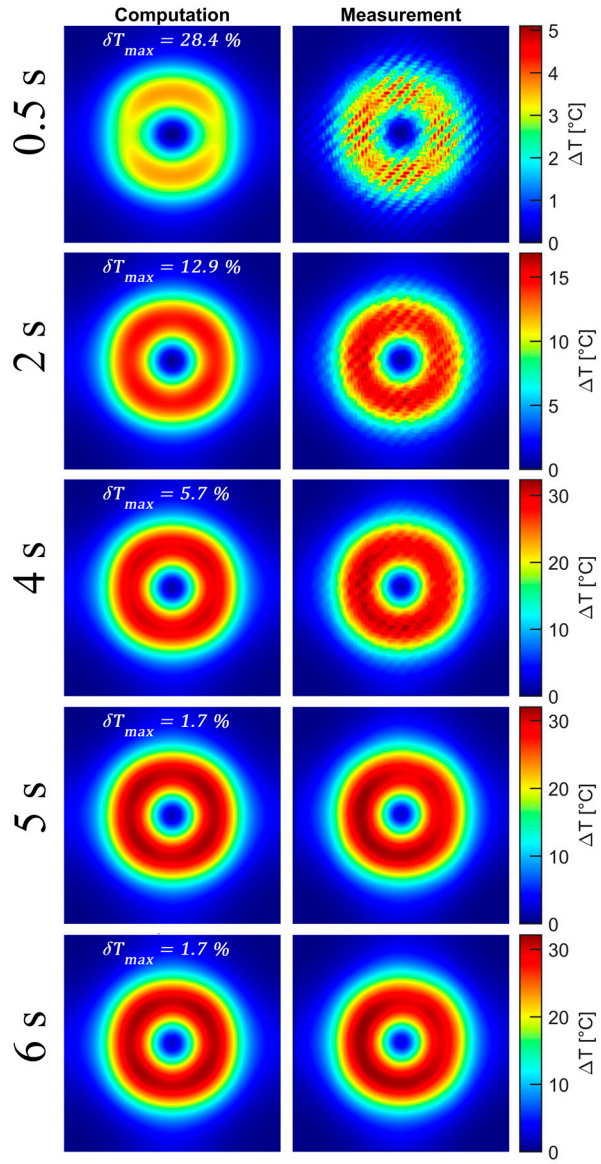

Figure 5.12. The front surface temperature of plate Twill-6plies-1 at different timestamps. Corresponiding time series for all the twill-plates are presented in Paper IV. Adapted from Paper IV.

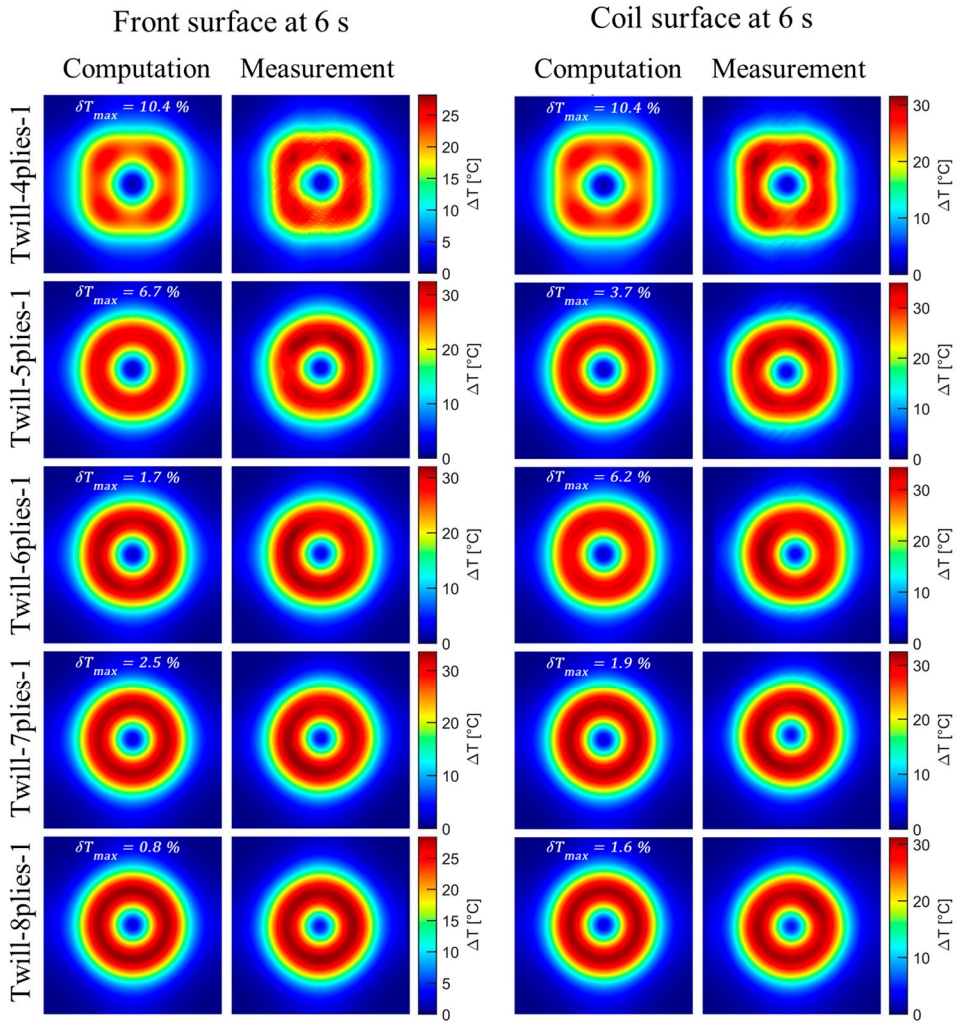

Figure 5.13. Temperature distribution of the front surface and coil surface at the timestamp 6 s. The induction heating duration was 4 s. Adapted from Paper IV.

5.3.3 Comparison between cross-ply and woven CFRP

The value of σ_Z at a certain fibre volume fraction is higher in woven CFRP than in cross-ply CFRP according to the comparison presented in Figure 4.9. This means that for a certain combination of fibre volume fraction and layer thickness (equivalent value for woven CFRP), more isotropic behaviour can be expected in woven CFRP than in cross-ply layup. However, to systematically investigate this, it is necessary to compare cross-ply plates and woven CFRP plates having approximately the same fibre volume

fraction and layer thickness. Figure 5.14 shows the position of the cross-ply plates and woven plates in a coordinate system with the fibre volume fraction on the *x*-axis and the layer thickness (equivalent UD-layer thickness d_{UD} for the woven CFRP) on the *y*-axis. Two combinations of woven and cross-ply plates with approximately the same fibre volume fraction and layer thickness are highlighted. The temperature distributions shown were measured at the 6 s timestamp. It should be noted that the induction heating duration was 2 s in the cross-ply study, Paper III, while it was 4 s in the woven study. However, the difference in temperature distribution pattern due to this time difference (2 s) is not significant and therefore it is reasonable to compare the temperature patterns from the cross-ply and woven plates. Figure 5.15 shows a comparison of the front surface temperature distributions for these plates, and it can be observed that for a low fibre volume fraction of approximately 0.35–0.4 (comparison 1), the difference in temperature distribution is significant, but that for a fibre volume fraction of approximately 0.45–0.5 (comparison 2), the difference in temperature distribution is less significant. The woven CFRP plate shows a more axisymmetric pattern although the fibre volume fraction of that plate is somewhat lower than the cross-ply plate in the comparison. This comparison clearly shows how the type of weave may affect the induction heating behaviour, although the fibre volume fraction is the same.

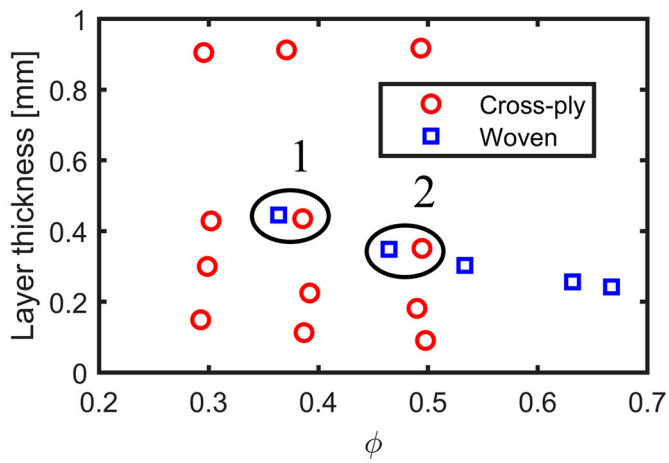

Figure 5.14. The positions of the cross-ply plates (red circles) and woven plates (blue squares) in a coordinate system with the fibre volume fraction on the *x*-axis and the layer thickness (equivalent value for woven plates) on the *y*-axis.

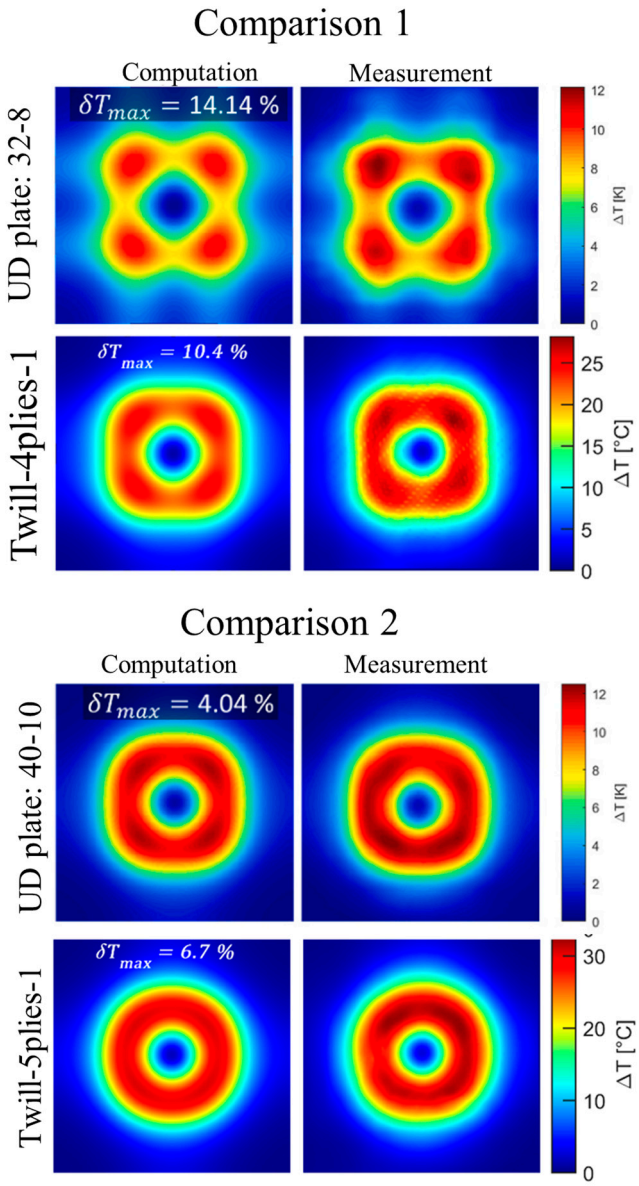

Figure 5.15. Comparison of front surface temperatures after induction heating completion. Each comparison is made between a cross-ply plate and a woven CFRP plate with approximately the same fibre volume fraction and approximately the same equivalent layer thickness

5.4 Axisymmetric finite element model (Model II)

For validation of the axisymmetric model (Model II) three woven CFRP plates with the same fibre volume fraction were used. For each plate, simulations and measurements at three different input power levels P_{CFRP} were performed; 400, 800 and 1600 W. The coil current levels and resulting input power are presented in Table 5.6. The values of P_{CFRP} presented here are based on the coil resistance ΔR_m at room temperature. As shown in Figure 4.10 the value of ΔR_m increases slightly with increasing temperature and thus the input power P_{CFRP} at a certain coil current will increase slightly with increasing temperature. All measurements are presented in Paper VI while in this section only the 800 W measurements for plate Twill-8plies-1 are presented. Figure 5.16 shows a time series of simulated and measured temperature distributions on the front surface. The left-hand subfigures show the simulated distributions, the centre column subfigures show the measured distributions, and the right-hand column of subfigures show the difference between the simulated and measured temperatures. The simulated and measured temperature distributions rapidly converges during the induction heating which can be explained by the fact that the approximate heat distribution time within layers, Table 4.5 (~0.1 s), is significantly shorter than the heating time of 10 s. This means that the amplitude of internal temperature peaks will be significantly lower than the reference temperature at the end of the heating according to equation (5.8). As observed in the right column, the edges of the square plates differ significantly more than the heated regions, which is a consequence of the axisymmetric geometry of the model; such deviations from the axisymmetric geometry cannot be modelled.

Table 5.6. Effictive coil current and resulting input power P_{CFRP} (in the CFRP) during the induction heating experiments, conducted to validate Model II.

Plate ID	Coil current [A]	P_{CFRP} [W]
Twill-8plies-1	24	424
	33	802
	46	1557
Twill-8plies-2	24	422
	33	798
	46	1551
Twill-8plies-3	24	422
	33	798
	46	1551

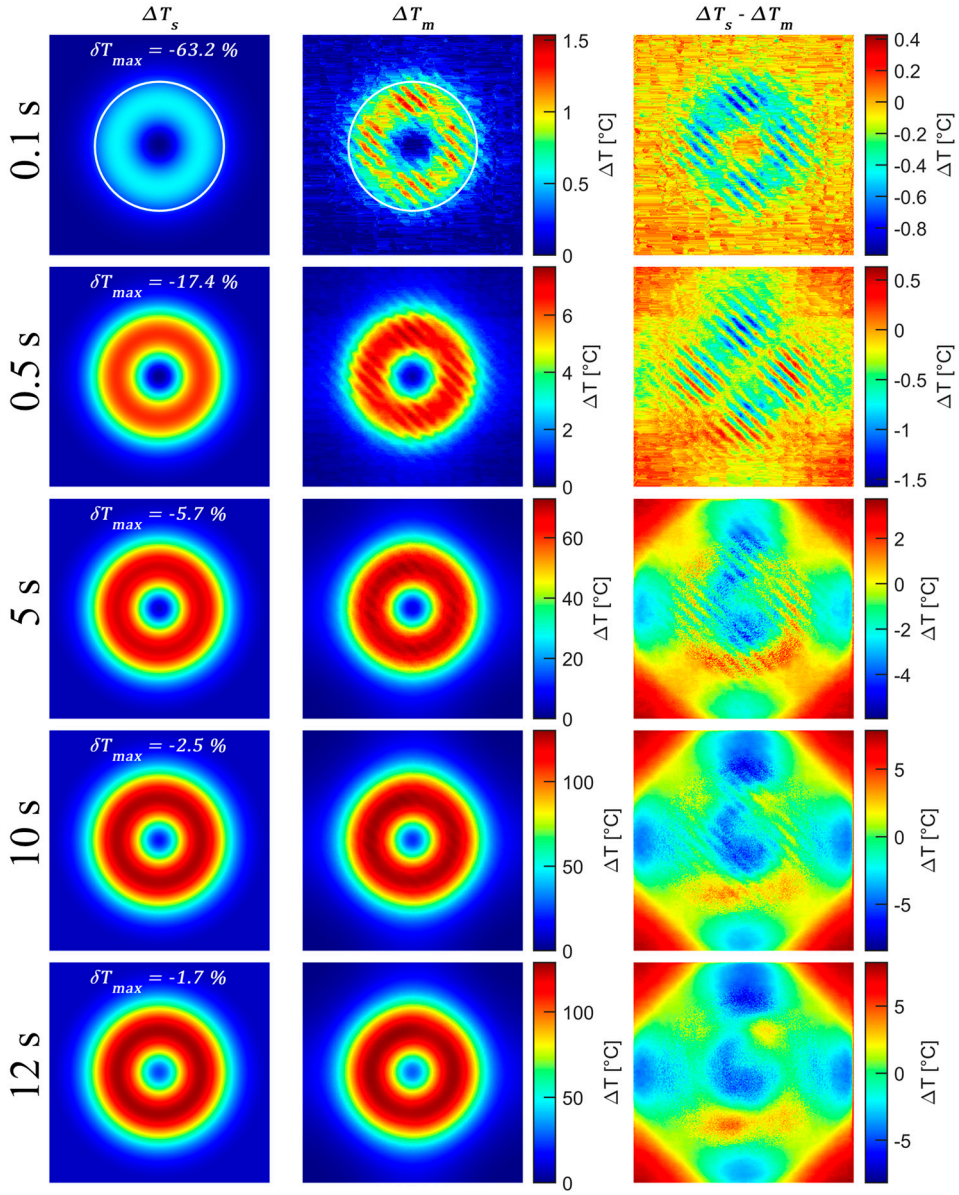

Figure 5.16. Comparison between simulated and thermographically measured front surface temperatures at different timestamps. The subfigures in the third column show the difference between the simulated and measured surface temperature distributions. The white circles on the 0.1 s images indicate the outer perimeter of the induction coil. Reprinted from Paper VI.

Figure 5.17 shows comparisons between the simulated and measured values of $\Delta T_{max}(t)$ for four different simulation cases. The same measured temperature curve is used in all cases, but the simulations were performed with different combinations of temperature dependent and non-temperature dependent material properties. The simulated and measured values agree best in simulation Case 1 in which all thermal and electrical properties are temperature dependent (diffusivity, specific heat capacity and electrical conductivity). Also, the result from Case 2 is acceptable, in which only the thermal properties are temperature dependent. This indicates that the measurement of temperature-dependent electrical conductivity could be omitted, reducing the need to characterize this parameter with respect to temperature. Case 3 and 4 when the temperature dependence of the thermal properties is not considered, result in simulated temperature curves significantly higher than the measured temperature curves. This is due to the significant increase of specific heat capacity within the investigated temperature range (Figure 4.22). For induction heating resulting in a small temperature increase, like $\Delta T_{max} \leq 30$°C used in Paper IV, it is enough to use material parameters measured at room temperature, but the error increases gradually with temperature and the limit for when temperature dependent measurements is needed must be assessed for each specific case.

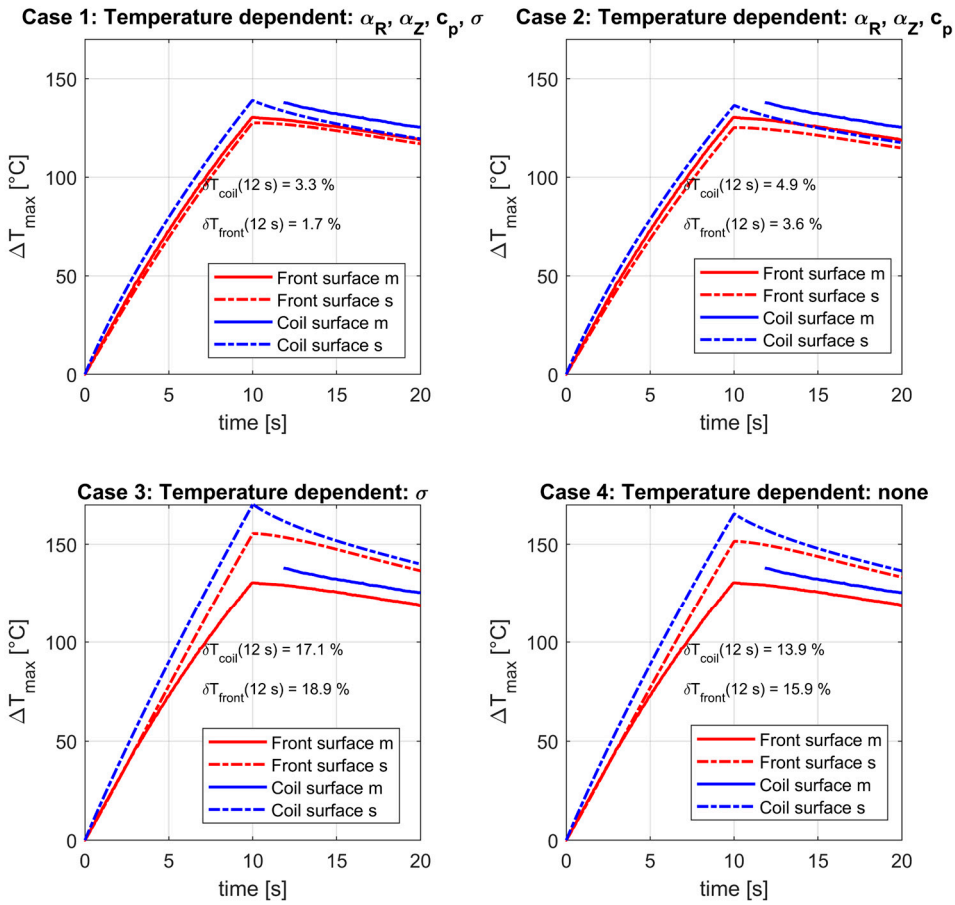

Figure 5.17. Comparison between the measured and simulated peak surface temperature ΔT_{max} for different cases of temperature-dependent material properties in the model. Reprinted from Paper VI. In the legends the letters m and s stands for measured temperature curve and simulated temperature curve.

5.5 Resistor network model (Model III)

The resistor network can be used to extract the power distribution within and between tows on woven CFRP. One example of simulated current and power distribution is shown in Figure 5.18. The CFRP plates Twill-4plies-1 and Twill-8plies-1 were used to validate the resistor network model. Figure 5.19 shows a time series of measured and simulated temperature distributions on the front surface during induction heating. The duration of the induction heating is 4 s (same measurements as presented in Paper IV). As for Model I and Model II, it is observed that the relative difference in peak

temperature decreases during and after the heating process. It is observed that for the plate with the highest fibre volume fraction, the agreement between simulated and measured results is the best, although the deviation is less than 10% even for the plate with the lowest fibre volume fraction. The current and resulting input power is the same as presented in Table 5.5. Figure 5.20 shows the measurements of the coil surface. As previously mentioned, it is impossible to measure this surface during induction heating, so the temperature distribution is only for the 6 s timestamp. In this model the heat generation is per definition uniformly distributed in the volume elements based on the power dissipated from the discrete resistor elements, unlike the FEM models where the heat generation becomes concentrated at the interface between crossing layers. However, based on the rapid temperature equalization through the thickness of the thin layers it is good simplification.

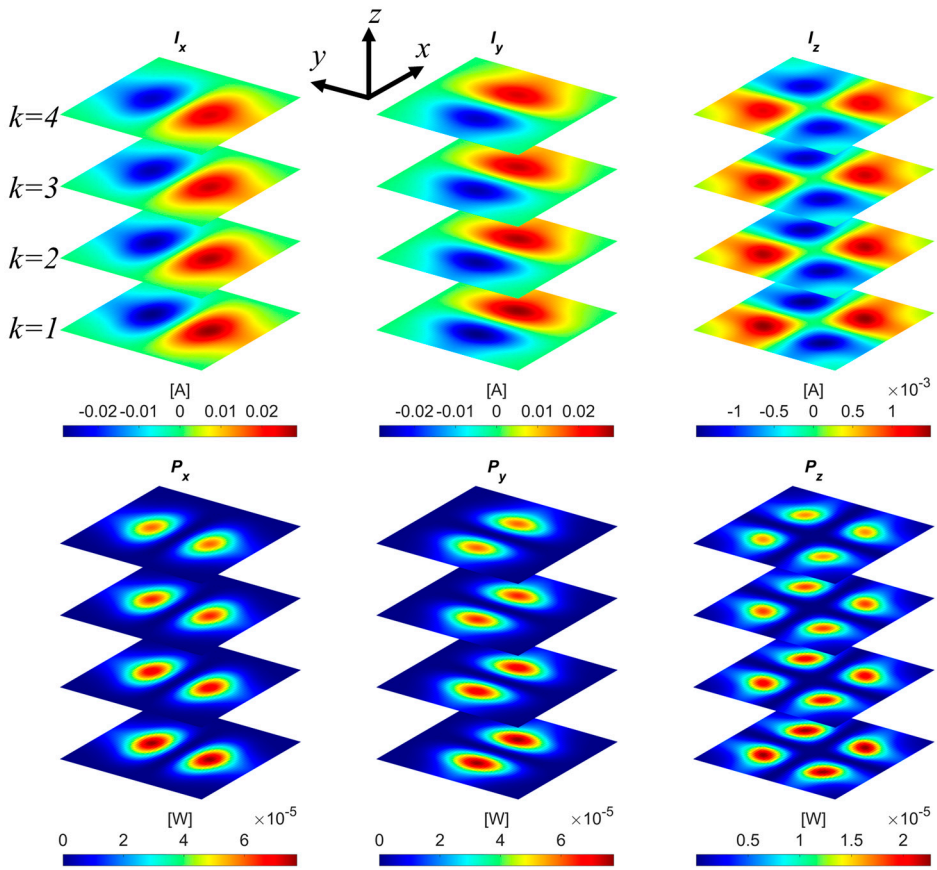

Figure 5.18. Simulated current and power distribution in a 4 ply woven plate when the coil current is 1 A. Current density distribution computed by the resistor network model. The first row shows the effective current level in each discrete resistor. Each pixel represent a resistor element. The second row shows the heating power developed in each resistor element. Reprinted from Paper VII.

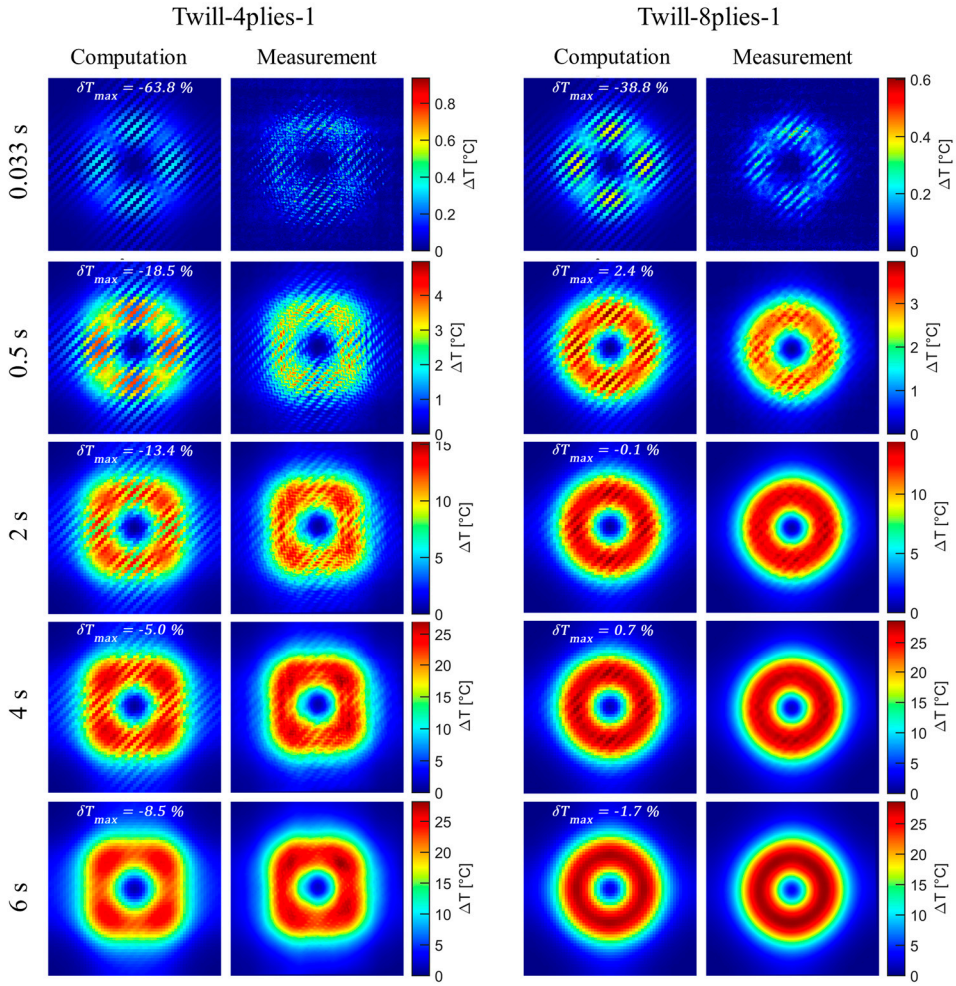

Figure 5.19. The left-hand subfigures show the comparison between simulated and measured front surface temperatures at different timestamps for the Twill-4plies-1 plate, and the right-hand subfigures show the same comparison but for the Twill-8plies-1 plate. The induction heating duration is 4 s in both cases. The effective coil current is 32.9 A for Twill-4plies-1 and 22.9 A for Twill-8plies-1 plates. Adapted from Paper VII.

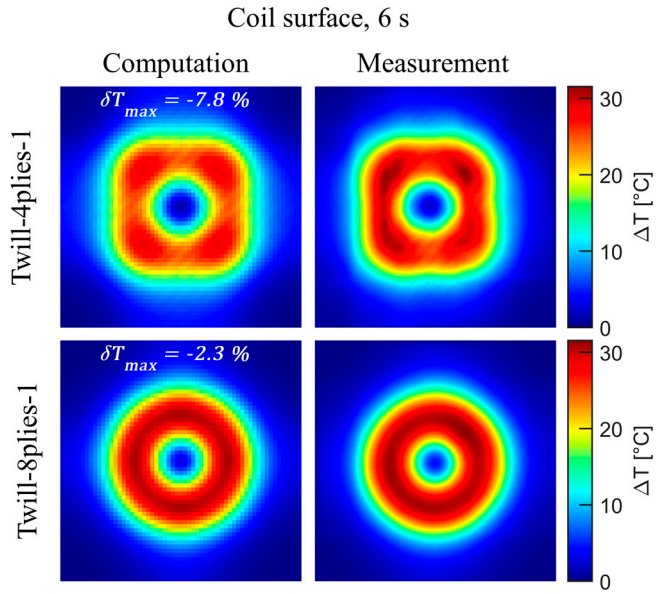

Figure 5.20. Temperature distribution on the coil surface at the 6 s timestamp, i.e. after completed induction. Adapted from Paper VII.

The model can also be used for predicting induced power distribution on the local tow size level. One way to measure the local heating pattern is to record the temperature pattern in the initial phase of induction heating, when no major heat conduction has yet occurred. In order to obtain measurable temperature increase levels within short transients the input power should be maximized. Table 5.7 shows the coil current and resulting input power P_{CFRP} during the high power experiments. Figure 5.21 shows the surface temperature distribution of the front surface at the initial phase of the heating. The heating time is shorter than the temperature equalization time presented for these plates in Table 5.4 and therefore it is obvious that the absolute temperature differs significantly. However, the pattern of the simulated and measured temperature distributions agree well.

Table 5.7. Effective coil current (rms) and heating power P_{CFRP} for the simulations and measurements presented in Figure 4.21.

Plate ID	Coil current [A]	P_{CFRP} [W]
Twill-4plies-1	190	14100
Twill-8plies-1	125	10600

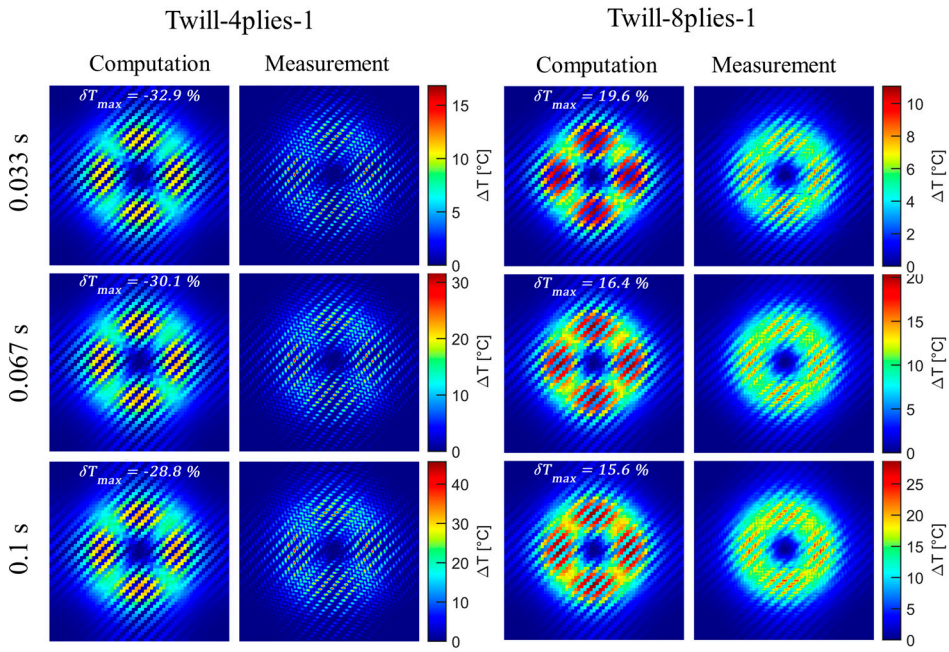

Figure 5.21. Comparison between computed and measured front surface temperature distributions. Adapted from Paper VII in which the plates are denoted plate 1 and plate 2.

6 Curing of epoxy-based CFRP using induction heating

6.1 Introduction

The study presented in this chapter has not been published elsewhere. The study was carried out together with Corebon AB as a LIGHTest-project financed by VINNOVA. The objective was to investigate the possibility of curing epoxy-based pre-preg CFRP by direct induction heating and to compare the results with those for CFRP manufactured using a heated metal moulding tool. The methods were compared with respect to the glass transition temperature T_g in relation to the curing temperature. The aim was to identify opportunities and challenges related to induction heating curing, rather than optimization of the process. In this chapter "Induction curing" denotes the curing of CFRP using the induction heating of the carbon fibres, and "reference curing" denotes the procedure when the heat is transferred to the CFRP by conduction from a metallic tool.

6.2 CFRP material and manufacturing process

Induction curing would be most advantageous for a quick curing thermoset since the temperature increase time of the tool or oven in a more traditional process accounts for a significant fraction of the total processing time. Therefore, a fast curing pre-preg, consisting of the fast-curing resin DT140RS from Deltapreg [58], and a 200-gsm twill-woven carbon fibre fabric with T300-type fibres from Toray [59] were used. The plies were automatically cut to shape and each CFRP plate consisted of 16 plies with the layup sequence [(0/90 ±45)4]S. This resulted in plates with a thickness of about 3.8 mm; resulting in a fibre volume fraction of about 50% according to equation (4.3), since the T300-type has a fibre density of 1760 kg/m^3.

The recommended curing cycle [58] is to place the pre-preg in a pre-heated tool at a temperature of 150°C for 3–5 minutes. However, during the induction curing process,

the pre-preg must be placed in the cavity before the temperature can be increased. The temperature was controlled to increase by 1°C/s. After the temperature increase, the reference temperature was kept at 150°C for five minutes and then the induction heating was turned off. The same temperature cycle was used in the reference tool. The cooling phase was more difficult to control. The direct-induction-heated tool cooled down by itself, driven by its thermal conductivity due to the non-heated thermal mass. To achieve approximately the same cooling rate in the reference tool, it was equipped with integrated cooling channels. The three plates produced with the direct induction heating method are denoted IH1, IH2, and IH3, whereas the plates produced with the reference tool are denoted REF1, REF2, and REF3.

6.3 Induction curing tool

6.3.1 Design of the induction curing tool

One challenge associated with induction heating is to achieve a uniform temperature distribution, due to the cancelation of circulating currents. As shown in Paper III, IV, and VI, the induction heating of CFRP using a circular coil can be approximated as an axisymmetric problem if the fibre volume fraction is high enough and the layers are thin enough. Therefore, to simplify the problem, it was decided to use prepreg plies cut to circular shape and circular coil geometry. A fabric with the low area weight (0.2 kg/m^2) was selected since it is equivalent to thin layers, resulting in a more isotropic behaviour, as described in Paper III and IV.

Since the induced heat is generated only within the carbon fibres, problems arise if there are large areas of epoxy with limited numbers of fibres, as these areas will not be properly cured unless heated from other sources. For both resin transfer moulding and compression moulding, there will be problems related to the induced temperature field. In the case of resin transfer moulding, there will be a problem related to the epoxy inlet tube and inlet channels in the tool where the epoxy will not be cured. A compression moulding tool does not need an inlet for the matrix material and the process can be designed so that fibres fill the entire volume, to ensure that all the matrix material reaches the same temperature. Therefore pre-preg compression moulding was selected.

A setup was built for the induction curing of pre-preg-based CFRP. Since the objective of the work was not to optimize a complex inductor to achieve uniform temperature throughout a challenging geometry, the CFRP geometry and thereby the coil geometry were designed to simplify the problem. An axisymmetric CFRP with a centred hole was

used due to the inevitable cancellation of eddy currents close to the centre when only one coil is used. Figure 6.1 shows an exploded three-dimensional view of the induction curing tool. To minimize the heating power gradient through the material thickness, a double-sided coil was used. To induce currents only in the carbon fibres the mould cavity and cover were made of the non-magnetic and electrically insulating glass fibre composite material G11. To prevent currents being induced in the press plates used to apply pressure to the material, magnetic flux concentrators were placed above and below the coil. Silicone gaskets were placed along the inner and outer radii of the cavity to seal the mould and prevent leakage. The red plates were also made of a glass fibre composite, machined to form the structural support for the embedded litz wire coils. The coil optimization, described later, was conducted prior to the manufacturing of these coil support structures.

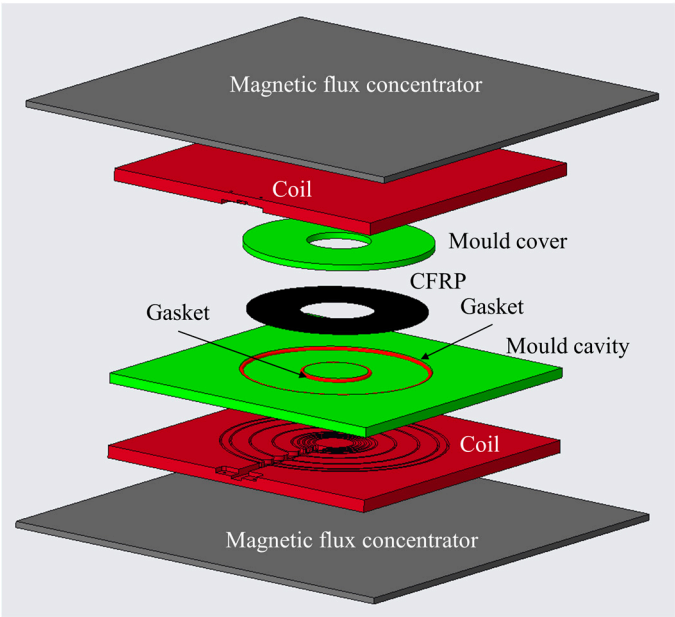

Figure 6.1: Exploded 3D view of the induction curing tool. The cavity has an inner diameter of 100 mm, an outer diameter of 300 mm, and a thickness of 6 mm (CFRP plates with a maximum thickness of 6 mm can be moulded).

To monitor the temperature of the curing pre-preg during induction heating, thermocouples were mounted in holes in the cover and cavity so that the tips of the thermocouples were aligned with the surface. The thermocouples were placed along three radial lines: two perpendicular, aligned with the fibre directions in the surface layer, and one aligned with one of the fibre directions of the ±45 directional layers. Figure 6.2 shows how the thermocouples were positioned in the cavity and the cover.

When the cover is mounted the thermocouple groups are aligned with the respective group of the cavity. Group 3 does not have any thermocouples in the cavity, only in the cover. The thermocouples in the cavity are denoted $T_{cavity}(n_g, n_r)$ and the thermocouples in the cover are denoted $T_{cover}(n_g, n_r)$, where n_g denotes the group number and n_r denotes the radial position number.

The induction heating process was controlled with respect to the peak temperature detected, i.e. independent of the position of the thermocouple detecting that temperature. The tool was placed in a hydraulic press to increase the cavity pressure during induction heating. The reference value for the cavity pressure was 60 bar. The pressure was calculated as the applied force divided by the pressure area, i.e., no pressure sensor was present in the cavity. The frequency range 50–60 kHz was used for the variable frequency drive. The mould cavity and mould cover surfaces were covered with a polyimide film treated with release agent to make it easy to release the CFRP part from the tool after curing completion, and to prevent the thermocouples from sticking to the CFRP surface. A side effect of this is reduced time response and accuracy of the temperature readings. Figure 6.3 shows the cavity prepared with polyimide film and how the pre-preg plies were stacked in the cavity. In order to investigate the influence from induction heating on the thermocouples the temperature signal was recorded while driving a coil current equal to the maximum coil current during curing, without any CFRP present in the cavity. It was found that no noticeable temperature change occurred due to induction heating of the thermocouples themselves.

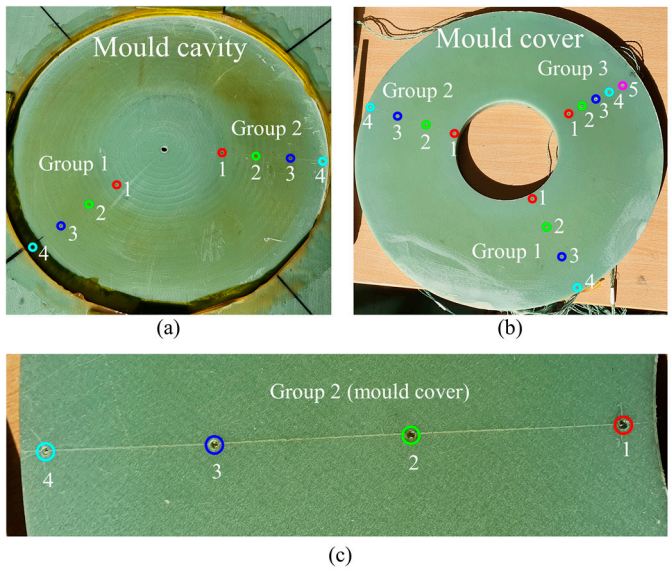

Figure 6.2. (a) Empty cavity with the thermocouple positions indicated. The same color coding is used in the temperature plots. This photograph was taken before the polyimide film, inner cylinder, and gaskets were mounted. (b) Cover with the thermocouple positions indicated. (c) Close-up image of thermocouples in group 2. In groups 1 and 2, the thermocouples were placed at radii of 55, 85, 115, and 145 mm and in group 3 the thermocouples were placed at radii of 70, 85, 100, 115, and 130 mm.

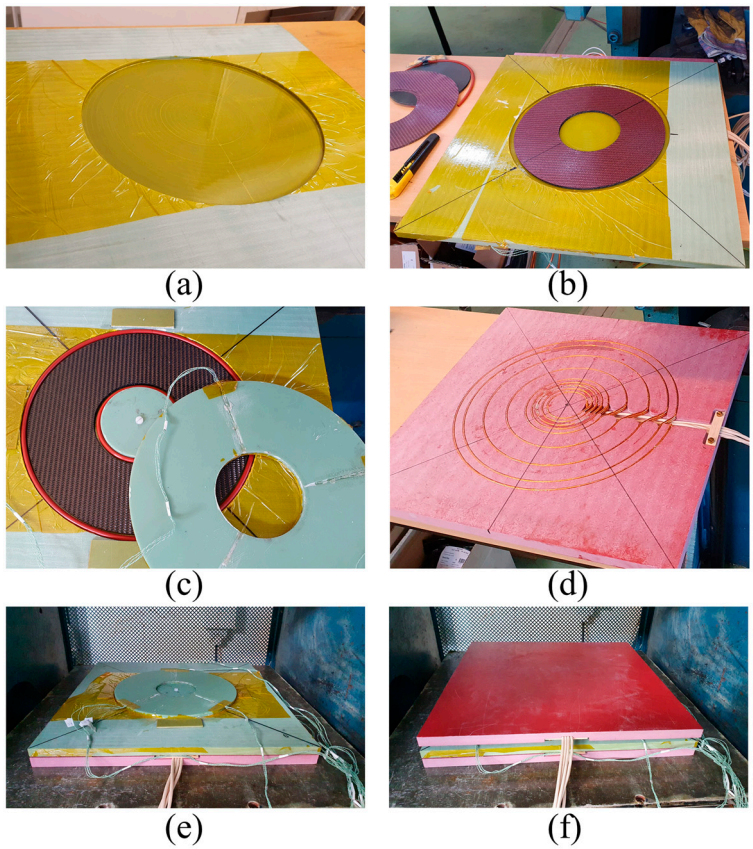

Figure 6.3. The different parts of the induction curing tool setup. (a) The mould cavity covered with release-agent-treated polyimide film (0.06 mm thick). (b) The pre-preg plies stacked in the cavity. The protective film has not yet been removed from the uppermost pre-preg ply, hence the purple colour of the surface. (c) The 6-mm-high central cylinder and the red gaskets have now been mounted. The cover is partially seen in the figure. (d) One of the coils. (e) Mould cavty and cover placed above one of the coils. (f) The coils stacked below and above the cavity and cover according to Figure 6.1 before applying pressure.

6.3.2 Coil optimization

Regarding the in-plane temperature distribution pattern the aim of this study was not to achieve a perfectly uniform temperature distribution. However to avoid large temperature variations, potentially with large uncured areas a simple optimization was conducted with respect to the distance between turns to improve the uniformity of the in-plane power distribution and resulting temperature distribution. Figure 6.4 shows the geometry of the axisymmetric electromagnetic finite element model representing the coil and the CFRP plate. The distance between the coil turns was optimized using MATLAB and the finite element software FEMM 4.2 [34]. Table 1 shows all the input

parameters to the optimization. The equivalent electrical conductivity was computed according to equation (4.15). The coil was modelled as a homogeneous litz domain.

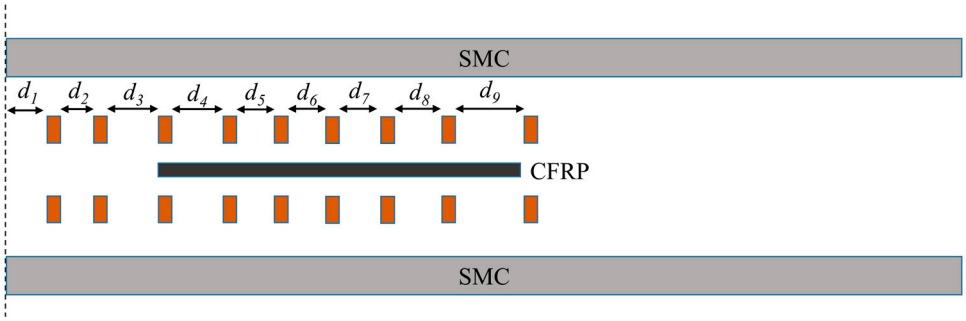

Figure 6.4. The axisymmetric geometry of the finite element model representing the coil and CFRP plate. The diistances between col turns in this illustration are not optimized. The coils are surrounded by magnetic flux concentrator plates above and below, denoted SMC – soft magnetic composite.

Table 1. Input parameters to the optimization process.

Property	Value
Number of coil turns	9
Frequency	55 kHz
Relative permeability of the magnetic flux concentrator (SMC)	16 (Paper I)
Electrical conductivity of the magnetic flux concentrator (SMC)	0 (Paper I)
Width of litz conductor	3.5 mm
Height of litz conductor	7 mm
Distance between coil and SMC	13 mm
Outer radius of CFRP	146 mm
Inner radius of CFRP	54 mm
Distance between coil and CFRP	10 mm
Electrical resistivity of Toray T300 (specified)	17 μΩm [59]
Fibre volume fraction, φ	0.5
Electrical conductivity of CFRP domain	According to equation (4.15)

Equation (6.1) presents the goal function to be minimized in order to achieve a uniform radial distribution of the heat generation Q [W/m^3]. This function gives the quadratic difference between the induced radial power distribution and the mean value of the radial heating distribution Q_{mean}. The radial distribution is based on the mean through thickness value $Q(r)$ at the radial position r according to equation (6.2) where $Q(r, z)$ is the heat generation at position (r, z). Q_{mean} is calculated according to equation (6.3). The variables r_i and r_y denotes the inner and outer radius of the CFRP domain. A minimum value of the goal function (6.1) was sought by iteratively adjusting the

distance between the coil turns. The MATLAB function *lsqnonlin* was used to conduct the optimization.

$$\int_{r=r_i}^{r_y} (Q(r) - Q_{mean})^2 \tag{6.1}$$

$$Q(r) = \frac{1}{d_{CFRP}} \int_{z=0}^{d_{CFRP}} Q(r,z) \tag{6.2}$$

$$Q_{mean} = \frac{1}{r_y - r_i} \int_{r=r_i}^{r_y} Q(r) \tag{6.3}$$

In Figure 6.5 the blue curve presents $Q(r)$ normalized against its peak value $max(Q(r))$ and the red curve presents the mean value Q_{mean} normalized against max($Q(r)$).

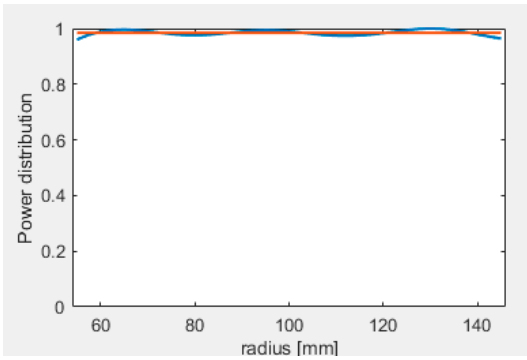

Figure 6.5. The blue curve presentes the simulated radial power distribution Q(r) after the optimization, and the red curve represents the mean value of Q(r) in the radial range from r_i to r_y. The values are normalized with respect to the peak power max(Q(r)), i.e., represented by a value from 0 to 1.

6.4 Reference curing tool

To evaluate the performance of the induction cured CFRP plates, it was necessary to compare them with a plate manufactured in a more traditional way, but still having a rapid thermal cycling capability. Therefore, a compression moulding tool was made in which the tool itself is heated and the heat is transferred conductively to the pre-preg. Figure 6.6 shows an exploded three-dimensional view of the reference tool. The reference tool consists of a cavity and a cover made of aluminium. The tool surface was treated with release agent before curing the CFRP. The cavity has a diameter of 200 mm. A silicone gasket is placed in the cavity to maintain the pressure during curing and to prevent leakage of liquid epoxy. Also, in heating the reference tool, induction heating is used as the heat source to enable rapid heating rates; in this case, however, it is the tool that is heated and then the heat is conductively transferred to the CFRP. Another pair of coils was used in this setup, but it did not need to be optimized as well due to the high thermal diffusivity of aluminium. This tool is further referred to as the reference tool. This approach is similar to the technology presented by Schaal [60]. To improve the energy efficiency of the induction heating, a ferromagnetic steel sheet is placed between each coil and the aluminium mould. Figure 6.7 shows the reference tool, with subfigure (a) showing the mounted tool and subfigure (b) showing the two tool halves separated after plate curing. The cured plate can be seen in the cavity surrounded by the silicone gasket The internal water-cooling channels were used to quickly cool down the cover and cavity. Water tubes are connected to the tool, as shown in Figure 6.7. The thermocouples are mounted in the cover and cavity 4 mm below the surfaces. The thermocouples in the cavity are denoted $T_{cavity}(n)$ and the thermocouples in the cover are denoted $T_{cover}(n)$, where n denotes the in-plane position indicated in Figure 6.8.

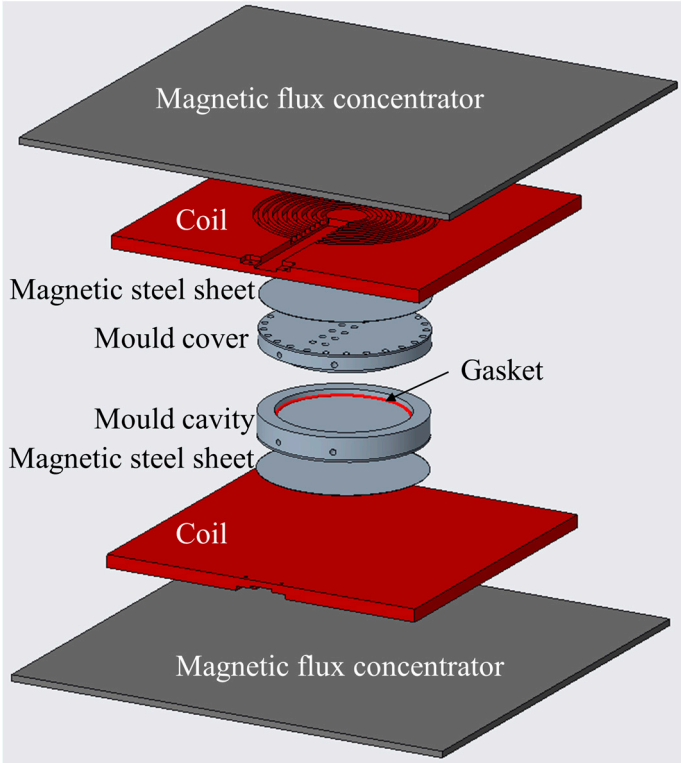

Figure 6.6. Exploded 3D view of the reference tool. The inner diameter of the cavity is 200 mm. The mould cover and cavity are made of aluminium. Due to the low heating efficiency of the induction heating of aluminium, thin magnetic steel sheets are placed above and below the tool during induction heating to improve energy efficiency during induction heating.

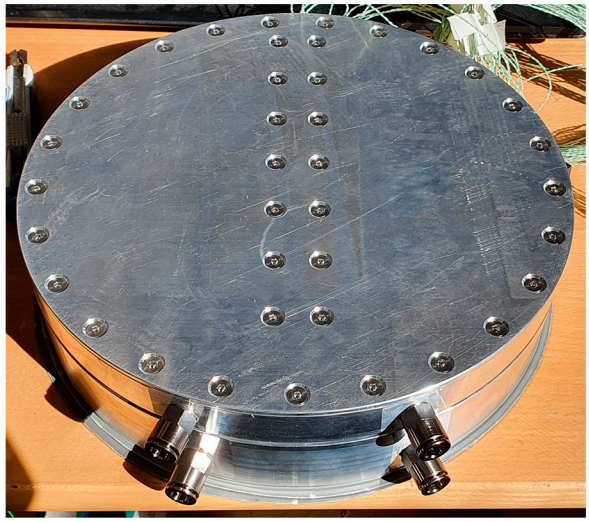

(a)

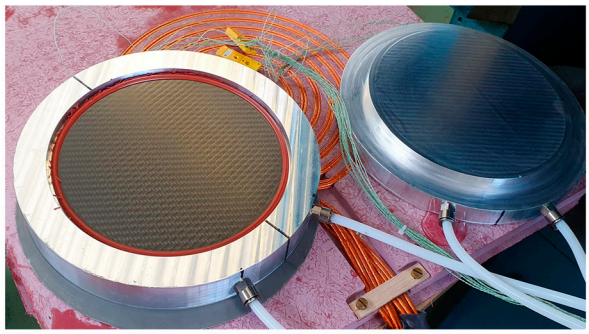

(b)

Figure 6.7. (a) Closed reference tool. (b) Open reference tool with a cured CFRP plate in the cavity The cooling water is supplied via the white tubes. The two tool halves are placed above one of the induction coils.

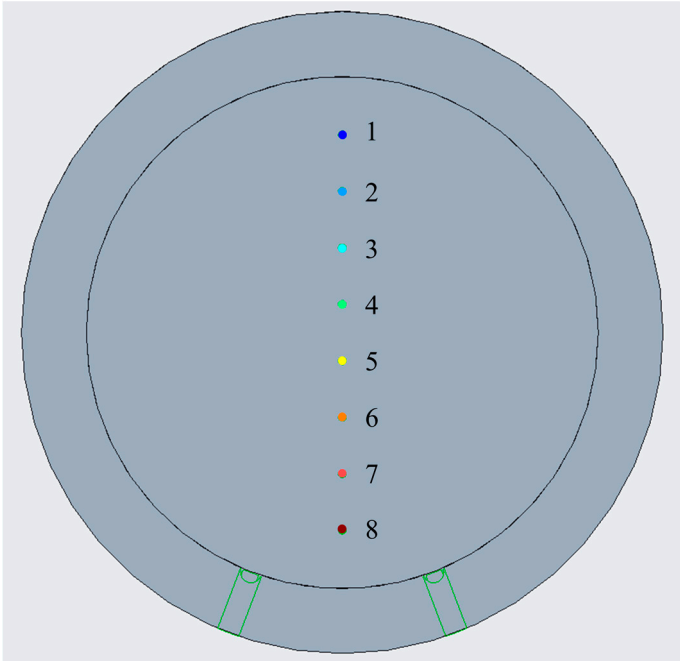

Figure 6.8. The in-plane placement of the thermocouples in the cavity and the cover. The distance between the thermocouples is 22 mm. The thermocouples are placed 4 mm below the surface in the cover and the cavity. The contours of the water cooling inlet and outlet are shown in green. The same colour coding is used when the temperature curves measured by the thermocouples are plotted.

6.5 Characterization methods

To characterise the glass transition temperature of the cured plates Dynamic mechanical analysis (DMA) and Differential scanning calorimetry (DSC) were used. The measurements were performed by RISE SICOMP AB, within the LIGHTest-project.

6.5.1.1 Dynamic mechanical analysis

Dynamic mechanical analysis (DMA) is a characterization method for measuring viscoelastic properties, including the glass transition temperature T_g. The measurements were conducted using a single-cantilever clamp. An oscillating strain is applied to the sample and the resulting stress is measured. By measuring stress σ , strain ε, and the phase lag δ between stress and strain, the storage modulus E' and the loss modulus E'' could be determined according to equations (6.6) and (6.7). The storage modulus E' accounts for the elastic energy stored in the system, and the loss modulus E'' accounts

for the energy that dissipates during oscillation. In this context, σ_0 represents the stress amplitude and ε_0 represents the strain amplitude. The relationship between the loss modulus and the storage modulus yields the value of tan(δ), so within the context of DMA this relationship is commonly called just tan(δ).

$$\sigma = \sigma_0 \sin(t\omega + \delta) \tag{6.4}$$

$$\varepsilon = \varepsilon_0 \sin(t\omega) \tag{6.5}$$

$$E' = \frac{\sigma_0}{\varepsilon_0} \cos\delta \tag{6.6}$$

$$E'' = \frac{\sigma_0}{\varepsilon_0} \sin\delta \tag{6.7}$$

$$\tan\delta = \frac{E''}{E'} \tag{6.8}$$

The DMA method can be used to determine the glass transition temperature T_g, which can be defined in different ways. In this study, two different definitions of T_g were used: the temperature at which the storage modulus E' starts to decrease rapidly, called the onset temperature, and the temperature at which tan(δ) has its peak value. Figure 6.9 shows the temperature-dependent modulus curves from the DMA measurement of the sample DMA90 from plate IH2. Figure 6.9 shows the onset value of T_g as 132.92°C and the peak tan(δ) value as 153.20°C.

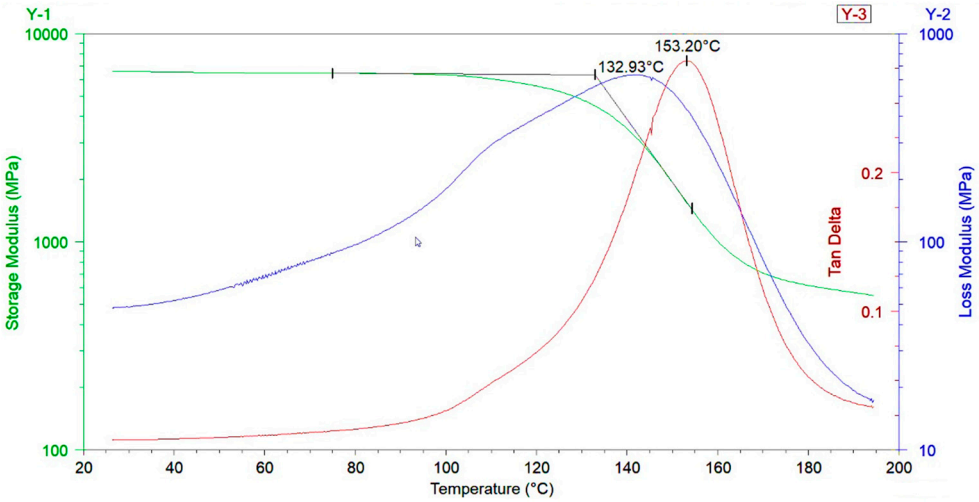

Figure 6.9. DMA measurement for the sample DMA90 from plate IH2. The value of T_g is indicated using two different definitions of T_g: the onset value of the storage modulus curve (132.93°C) and the peak value of tan(δ) (153.20°C).

The DMA measurements in this study were conducted following the standard ASTM D4065-12. A frequency of 1 Hz was used, with a temperature increase rate of 5°C /min. A strain amplitude ε_0 of 0.01% was used.

6.5.1.2 Differential scanning calorimetry

Differential scanning calorimetry (DSC) is a method for measuring the heat capacity of a material. The method can be used to detect the glass transition temperature T_g. By continuously increasing the temperature of a sample, exothermic and endothermic reactions can be detected at different temperatures. The power continuously absorbed by the sample is measured, and a phase transition from a rubbery state to a glassy state will appear as an endothermic reaction. Figure 6.10 shows the DSC measurement for one of the sample extracted from plate REF1. The heat flow continuously increases due to the fact that the specific heat capacity increases with increasing temperature. The glass transition temperature is detected as a step increase in this curve at 142°C, i.e. an endothermic reaction. However, for most of the samples the transition was vague and it was difficult to detect well-defined glass transition temperatures with this method.

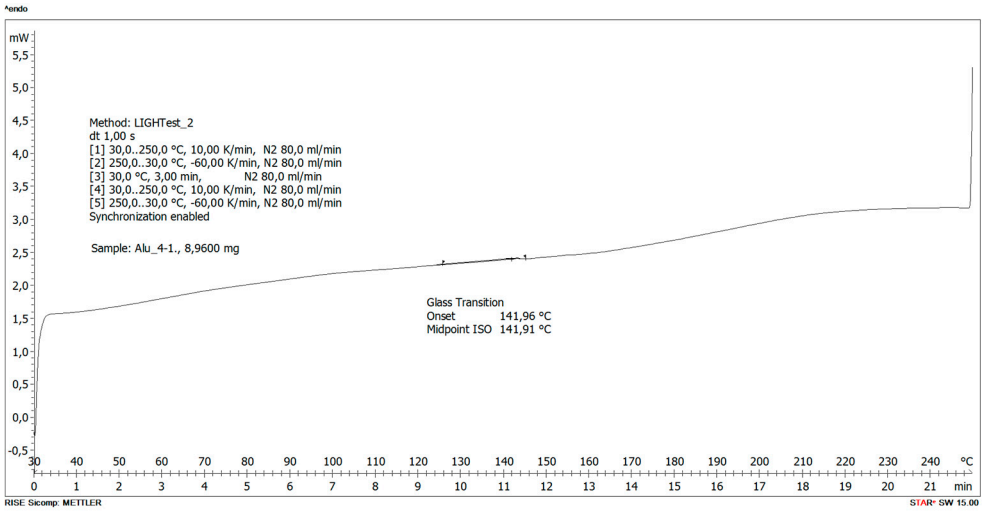

Figure 6.10. DSC curve from measuring one of the samples of plate REF1.

6.6 Extraction of samples

The DMA samples were extracted along the 0° fibre direction in group 1, along the 45° fibre direction in group 2, and along the 90° fibre direction in group 3. The same directions were used for both the REF samples and IH samples. The samples from the induction-cured plates were extracted according to Figure 6.11. The positions of the DSC samples were selected so that they overlapped the positions of the thermocouples, making it easy to compare the measured T_g with the measured curing temperature. The DMA samples were larger, so the average curing temperatures associated with these samples were based on the thermocouple measurements close to the sample. The average curing temperatures of the different samples were calculated according to equation (6.9), where $T_{meas}(i)$ is the i:th temperature measurement associated with that sample and N is the total number of temperature measurements associated whit the sample. For the DSC samples the associated curing temperature is based on two measurements while for the DMA samples at least four measurements are included. Table 6.1 presents the temperature measurements associated with each sample. The DSC samples were 8 mm in diameter and the DMA samples were 10 × 35 mm in size. The plates have thickness of approximately 3.8 mm.

$$T_{curing} = \frac{1}{N}\left(\sum_{i}^{N} T_{meas}(i)\right) \tag{6.9}$$

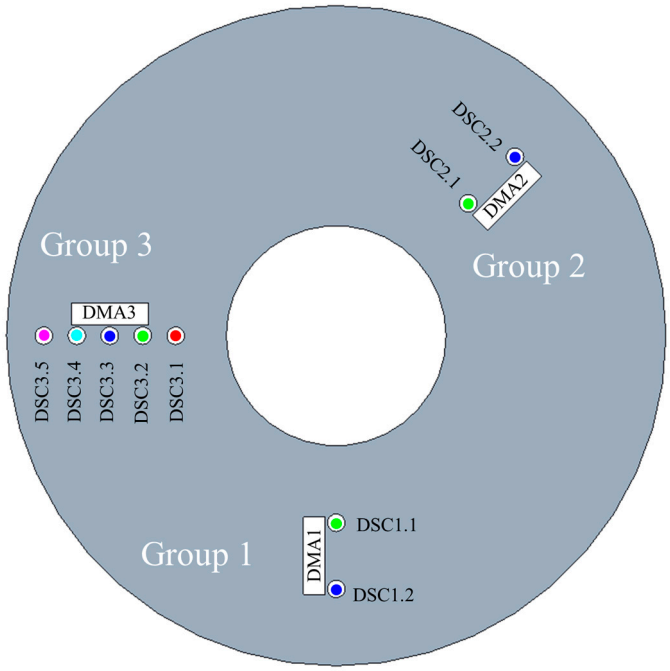

Figure 6.11. The positions where the DMA and DSC samples were extracted from the IH-plates, shown relative to the outer dimensions of the cavity; inner diameter 100 mm and outer diameter 300 mm.

Table 6.1. Temperature measurements used to compute the mean temperature of each IH plate sample.

T_{curing}	$T_{meas}(1)$	$T_{meas}(2)$	$T_{meas}(3)$	$T_{meas}(4)$	$T_{meas}(5)$	$T_{meas}(6)$
$T_{DSC1.1}$	$T_{cover}(1,2)$	$T_{cavity}(1,2)$				
$T_{DSC1.2}$	$T_{cover}(1,3)$	$T_{cavity}(1,3)$				
$T_{DSC2.1}$	$T_{cover}(2,2)$	$T_{cavity}(2,2)$				
$T_{DSC2.2}$	$T_{cover}(2,3)$	$T_{cavity}(2,3)$				
$T_{DSC3.1}$	$T_{cover}(3,1)$	$T_{cavity}(3,1)$				
$T_{DSC3.2}$	$T_{cover}(3,2)$	$T_{cavity}(3,2)$				
$T_{DSC3.3}$	$T_{cover}(3,3)$	$T_{cavity}(3,3)$				
$T_{DSC3.4}$	$T_{cover}(3,4)$	$T_{cavity}(3,4)$				
$T_{DSC3.5}$	$T_{cover}(3,5)$	$T_{cavity}(3,5)$				
T_{DMA1}	$T_{cover}(1,2)$	$T_{cavity}(1,2)$	$T_{cover}(1,3)$	$T_{cavity}(1,3)$		
T_{DMA2}	$T_{cover}(2,2)$	$T_{cavity}(2,2)$	$T_{cover}(2,3)$	$T_{cavity}(2,3)$		
T_{DMA3}	$T_{cover}(3,2)$	$T_{cavity}(3,2)$	$T_{cover}(3,3)$	$T_{cavity}(3,3)$	$T_{cover}(3,4)$	$T_{cavity}(3,4)$

The reference plate samples were extracted according to Figure 6.12. The curing temperature associated with each sample was calculated according to equation (6.9) using the temperature measurements from Table 6.2. As in the case of the induction-cured plates, the DMA samples from the reference plates were also extracted from three different fibre directions (0°, 45° and 90°).

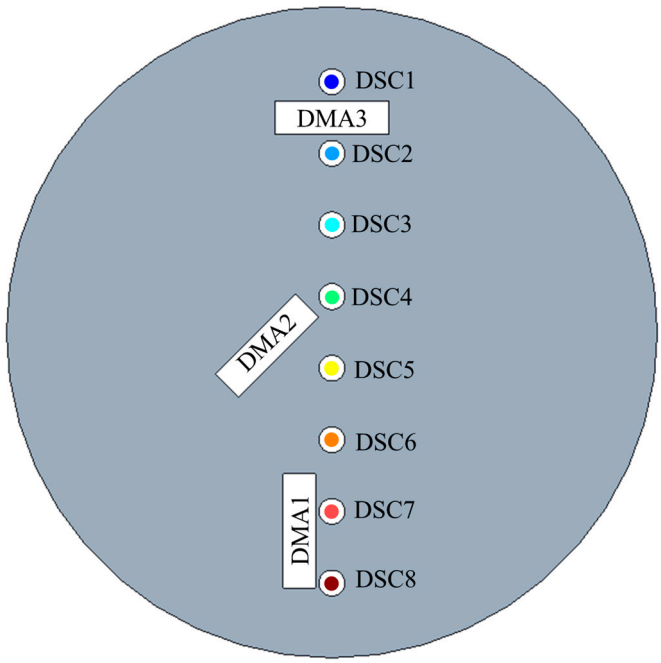

Figure 6.12. The positions where the DMA and DSC samples were extracted from the reference CFRP plates, shown relative to the outer dimensions of the cavity; diameter 200 mm.

Table 6.2. Temperature measurements used to compute the mean temperature of each reference plate sample.

T_{curing}	$T_{meas}(1)$	$T_{meas}(2)$	$T_{meas}(3)$	$T_{meas}(4)$	$T_{meas}(5)$	$T_{meas}(6)$
T_{DSC1}	$T_{cover}(1)$	$T_{cavity}(1)$				
T_{DSC2}	$T_{cover}(2)$	$T_{cavity}(2)$				
T_{DSC3}	$T_{cover}(3)$	$T_{cavity}(3)$				
T_{DSC4}	$T_{cover}(4)$	$T_{cavity}(4)$				
T_{DSC5}	$T_{cover}(5)$	$T_{cavity}(5)$				
T_{DSC6}	$T_{cover}(6)$	$T_{cavity}(6)$				
T_{DSC7}	$T_{cover}(7)$	$T_{cavity}(7)$				
T_{DSC8}	$T_{cover}(8)$	$T_{cavity}(8)$				
T_{DMA1}	$T_{cover}(6)$	$T_{cavity}(6)$	$T_{cover}(7)$	$T_{cavity}(7)$	$T_{cover}(8)$	$T_{cavity}(8)$
T_{DMA2}	$T_{cover}(4)$	$T_{cavity}(4)$	$T_{cover}(5)$	$T_{cavity}(5)$	$T_{cover}(6)$	$T_{cavity}(6)$
T_{DMA3}	$T_{cover}(1)$	$T_{cavity}(1)$	$T_{cover}(2)$	$T_{cavity}(2)$		

6.7 Results and discussion

DMA samples were extracted along three different fibre directions for both IH-samples and REF-samples. The three plates manufactured with the induction curing tool are denoted IH1, IH2, and IH3. The three plates manufactured with the reference tool are denoted REF1, REF2, and REF3. Figure 6.13 shows one of the induction-cured plates on which the positions of the temperature measurements are marked. Ocular inspection shows that much of the plate is cured but that the edges are problematic, with edge regions of up to 10 mm not being cured. This pattern indicates that that the induced power distribution and temperature distribution were fairly axisymmetric during the curing.

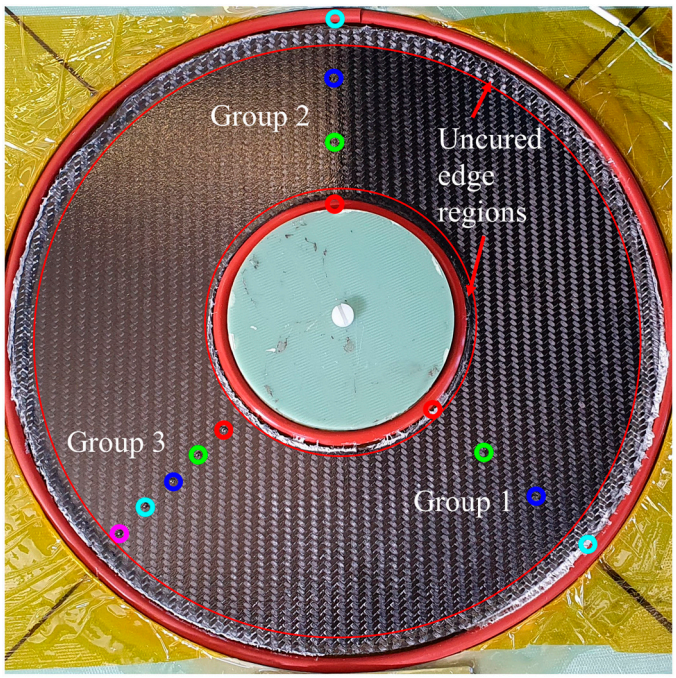

Figure 6.13. CFRP plate in the cavity after the induction curing process. The positions of the temperature measurements are indicated.

Figure 6.14 shows the temperatures recorded by the integrated thermocouples during the curing of plate IH1. A noticeable temperature difference between the measurement positions can be observed. In particular, significantly lower temperatures are measured at the edges than the rest of the plate, which correlates to the uncured edges observed in Figure 6.13. Since the tool is symmetrical along a horizontal plane, the temperature

distribution on both surfaces should be approximately equal. However, in some positions, a difference in temperature can be observed between the two surfaces. This may be due to non-uniformities in the applied pressure distribution, resulting in differences in the thermal contact between thermocouple and CFRP. The tool was designed to accommodate 21 potential measurement positions, but the measurement equipment could only handle 16 measurements at the same time. Therefore, some of the measurement points close to the inner and outer radii were omitted (although they are represented by legends in Figure 6.14) , i.e., $T_{cavity}(1,1)$, $T_{cavity}(1,4)$, $T_{cavity}(2,1)$, $T_{cavity}(2,4)$, and $T_{cover}(2,1)$.

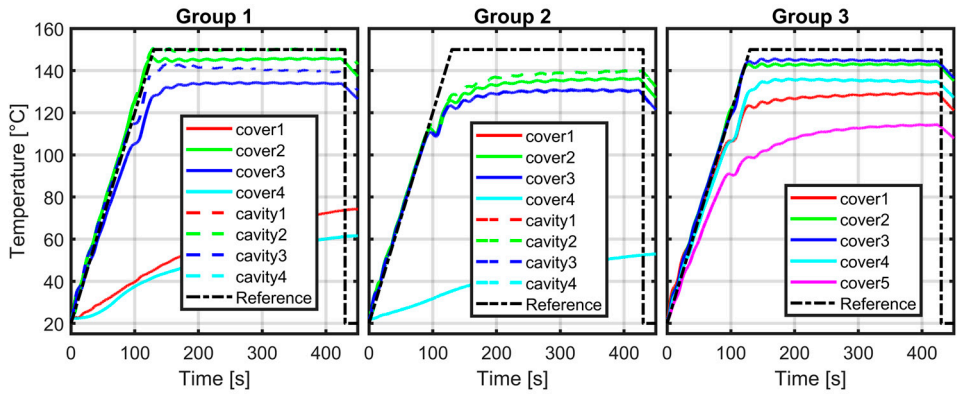

Figure 6.14. Temperature measurements made during curing with the induction curing tool. Each subfigure shows the temperature measurements for one of groups 1, 2, and 3. Measurements were made when manufacturing plate IH1. Legends are presented for all the measurement positions but the following were not measured: $T_{cavity}(1,1)$, $T_{cavity}(1,4)$, $T_{cavity}(2,1)$, $T_{cavity}(2,4)$, and $T_{cover}(2,1)$.

Figure 6.15 shows the temperature curves of the reference tool and it is clear that a more uniform in-plane temperature distribution is achieved compared to the induction curing tool.

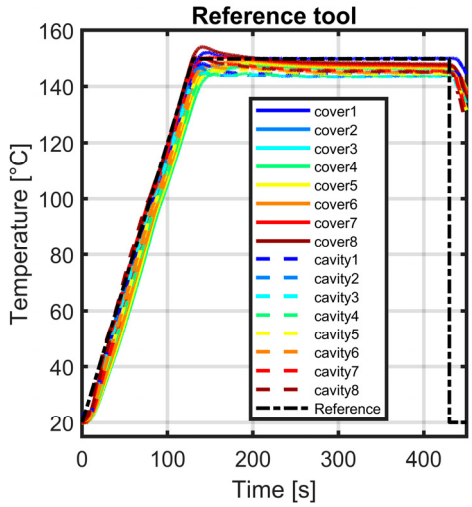

Figure 6.15. Temperature measurements made during the curing of plate REF1 using the reference tool.

From the DMA measurements, the values of T_g were extracted using two different definitions of the glass transition temperature: the onset temperature and the tan(δ) peak temperature. Figure 6.16 shows the measured values of T_g versus the curing temperature. In this figure, T_{curing} is based on the temperatures measured at the end of the induction heating process, at the 400-s timestamp, when most of the temperature curves have reached stationarity. The resulting T_g from the onset DMA measurements remains relatively constant independent of the measured curing temperature, and despite the fact that in some positions the temperature increased very slowly during the process. The tan(δ) measurements indicate that the T_g from the IH-samples decrease slightly with increasing temperature, which is difficult to interpret. These findings indicate that the actual temperature in the CFRP might be higher than that measured by the thermocouples. This can be explained by the placement of the thermocouples. Since the G11 material is not heated by the induction the thermocouples placement in the G11 material behind a polyimide film gives an indirect measurement of the temperature in the CFRP domain, resulting in a measured value that is lower than the internal temperature in the CFRP domain until there is no temperature gradient between G11 and CFRP. Regarding the temperature measurement in the reference tool, the measured temperature will, in contrast, result in a higher value than the actual internal temperature during the temperature increase transient, since the heat is transformed conductively from the aluminium-tool to the pre-preg. However, aluminium has a significantly higher thermal conductivity than does G11 (in the order of 100 times higher), meaning that it is much easier to achieve a uniform temperature

field in the reference tool than in the induction curing tool. The value of the glass transition temperature T_g obtained from the DSC measurement displays significantly higher dispersion. However, as previously discussed regarding the DSC method, it was difficult to observe any distinct T_g from the DSC measurements, so these measurements should be interpreted with care. The DMA values retrieved in this study are lower than the values reported by the manufacturer; i.e., 146.85°C onset and 165.20°C tan(δ).

Aside from the comparison of T_g, this study identified a number of other challenges. One of the major challenges identified is the difficulty of properly measuring the temperature of the pre-preg during curing. Since the tool itself is not cured the temperature sensors measuring the surface of the curing part will be cooled down by the mould and cavity. The usage of a protection film between the sensor and the prepreg also acts a delay for the temperature measurement. Instead the sensors could be placed directly onto the CFRP or within the CFRP structure but then there is a risk that the sensor will get stuck in the structure after curing. Internal sensors also may affect the induced power distribution. Another major challenge is that of achieving a uniform temperature field in the CFRP part to be cured. The cold inner and outer edges indicate that a higher power density is required in these areas. Instead of optimizing with respect to induced power distribution, the process should instead be optimized with respect to the temperature.

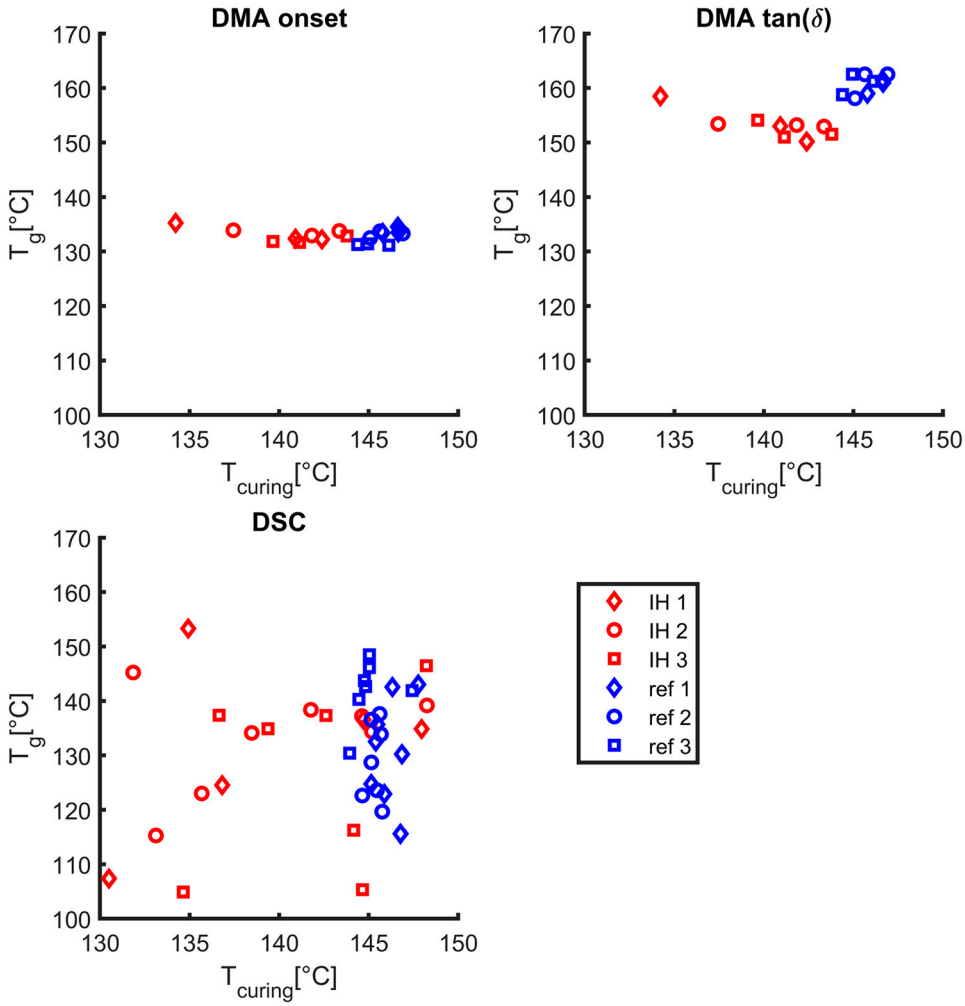

Figure 6.16. Glass transition temperature T_g versus the curing temperature measured using DMA and DSC. From the DMA measurements, the value of T_g is extracted based on two different definitions of the glass transition temperature T_g, i.e., the onset value and the tan(δ) value. In some of the samples, T_g could not be detected using the DSC method.

7 Summary of appended publications

Paper I: This article investigates how the heating energy efficiency of an ordinary pancake induction heating coil can be optimized by adding a flux concentration material and by replacing a traditional copper tube coil with a litz-wire-based coil. Thus, concentrating the magnetic field to the object to be heated and significantly reducing the joule losses in the coil conductor. It was shown that the proposed improvements may significantly increase the heating efficiency. Another benefit of using a flux concentrator is the reduced magnetic stray field.

Paper II: This article serves as a pre-study identifying composite parameters of importance during induction heating. CFRP plates made of different types of carbon fibre fabrics were manufactured, and then the differences in temperature distribution during induction heating were investigated. The results highlight the differences in induced temperature distribution as a consequence of different fibre types, fabric types, and fibre volume fractions. The differences in temperature equalization time between PAN- and pitch-based fibre fabrics are clear. It is also clear that an increasing fibre volume fraction makes the materials behave more like an isotropic material. The results served as a basis for the more systematic studies presented in the subsequent articles.

Paper III: This article characterizes and models the induction heating behaviour in cross-ply CFRP using a finite element model where each unidirectional layer is represented by a homogeneous and anisotropic domain. The heat capacity and density are represented by single scalar values and the electrical and thermal conductivities are represented by tensors. The paper proposes methods for characterizing the scalar and tensor values on the macroscopic level. The simulation results are compared with thermographic measurements made during induction heating. It is observed that the model provides the most accurate temperature predictions in the cases with high fibre volume fractions, 50%, and thin unidirectional layers, but in all cases the model provides good estimates of the relative in-plane temperature distribution.

Paper IV: This article investigates how the numerical model presented in Paper III can be used for modelling woven CFRP. It is described how a woven ply can be represented by two adjacent perpendicular unidirectional plies. It is observed that the agreement between measurements and simulations is as good as in the case of cross-ply CFRP.

Paper V: In this article it is proposed that the electrical conductivity in bidirectional woven CFRP can be approximated with a scalar value. The paper presents a method for measuring the equivalent electrical conductivity in non-consolidated dry-woven fabric.

Paper VI: This article proposes that CFRP with high fibre volume fraction can be modelled using an axisymmetric model. The model was validated with induction heating experiments on CFRP with a fibre volume fraction of about 66%, based on twill plies with an area weight of 600 g/m^2. The electrical conductivity is modelled as an equivalent scalar value (as in Paper II and V). It is shown that thermal properties should be modelled together with their temperature dependence, especially at high temperature levels, while the electrical conductivity can be regarded as a constant value, due to small variations with respect to varying temperature.

Paper VII: This article proposes a resistor network model for simulating the current and temperature distributions in CFRP during induction heating. An axisymmetric finite element model (see Paper V and VI) is employed to compute the induced electric field, and the current distribution is computed by solving a linear equation system based on Kirchhoff's circuit laws. This approach means that the three dimensional current distribution in a CFRP structure can be calculated based on simple 2D FEM simulation. The results of this work improve understanding of the induced power distribution in the joints versus in the fibres, depending on different fibre volume fractions.

8 Conclusions

8.1 Summary and conclusions

To explain and predict the heat generation and temperature distribution in CFRP during induction heating, simulation models were developed. Characterization methods were identified and developed to collect input data for the models. The developed models are based on different levels of macroscopic representation of the composite: either as anisotropic homogeneous layers or tow-elements, or as an isotropic homogenization of the whole structure. Conclusions from evaluating the models and characterizing the input parameters are presented below.

Model I: This 3D finite-element model was developed for predicting the temperature distribution in cross-ply CFRP during induction heating. The layers are modelled as homogeneous anisotropic domains. The simulation results show a high concentration of induced heating power near the interface between crossing layers. Temperature gradients of the same magnitude would be a severe issue but due to the thin unidirectional layers resulting in a short distance between the heat generation peaks it can be concluded that an even temperature distribution through the thickness will be generated during typical temperature increasing rates. For example in a cross-ply plate with a fibre volume fraction of 50%, consisting of unidirectional layers with an area weight of 100 g/m^2, the local internal temperature peaks will be insignificant after just a few seconds of heating. The rapid temperature equalisation within layers in combination with a large electromagnetic skin depth results in an almost even temperature distribution through the thickness of thin walled CFRP plates. This is beneficial in various applications such as thermoset curing and also means that the simulation model can be evaluated based on the measured surface temperature distribution.

For the cross-ply plates with the highest fibre volume fractions (above 50%) and thinnest layer thicknesses, the surface temperature distribution agrees almost perfectly between simulation and measurements, displaying “isotropic induction heating behaviour”. Isotropic induction heating behaviour means that the induction heating of CFRP results in a temperature distribution similar to that in an isotropic material with the same equivalent electrical conductivity. When the fibre volume fraction decreases

and the layer thickness increases, the difference between simulation and measurements increases with respect to both the pattern and the relative temperature difference. This is not just because of the low fibre volume fraction itself but also because a lower fibre volume fraction often results in a less uniform fibre distribution. For example, the through-thickness electrical conductivity (σ_Z), which is a homogeneous representation of the contact resistance between fibres through the thickness, will be less representative of the contact resistance between crossing layers as the uniformity decreases. However, although the model may not predict the temperature level perfectly for plates with low fibre volume fraction and very thick layers it still provides a good prediction of the temperature pattern, i.e. whether an isotropic behaviour can be expected or not, as well as the location of expected temperature peaks. The severeness of the temperature peaks can be predicted, as proposed, using a 1D- discretization of the heat equation.

It was also shown that this model works well for predicting the temperature distribution in woven CFRP. The equivalent value of σ_Z is higher in woven than cross-ply CFRP, resulting in more isotropic behaviour at a specific fibre volume fraction and equivalent layer thickness.

Model II: This finite-element model uses a 2D axisymmetric representation to predict the temperature distribution in CFRP during induction heating. More isotropic behaviour appears as the fibre volume fraction increases and the layer thickness decreases. It was therefore proposed that for CFRP that exhibits isotropic behaviour, the induction heating process may be modelled as axisymmetric in the case of a circular coil. This behaviour could be clearly observed in both twill-woven CFRP plates with a fibre volume fraction of about 50% and above, and in cross-ply plates with a fibre volume fraction of approximately 50% and layers with a thickness of 0.09 mm. This is because the good electrical conductance between crossing fibres and the rapid temperature equalization of local temperature peaks make the material behave like an isotropic material. Due to the significant reduction of computational cost when going from 3D to a 2D representation, this approach provides an effective modelling tool in the case of high fibre volume fraction and axisymmetric coils. Both the in-plane temperature distribution for the surfaces and the difference between the coil surface and front surface agree well with the simulation results, proving that the axisymmetric model is applicable.

Model III: This model, a hybrid of an axisymmetric model and a resistor network, computes the current distribution based on the induced electric field computed using the axisymmetric model. Based on the electric field computed using the 2D finite-element model, the current distribution in each woven ply can be solved separately using Kirchhoff's circuit laws. Each resistor element is associated with a volume element

when solving the temperature distribution using the finite-difference problem. The representation with uniformly heated volume elements is a valid simplification due to the rapid temperature equalization, as discussed previously. This model can be used to obtain a detailed view of the power distribution on the tow-size level during induction heating of woven CFRP, based on a 2D computation of the electromagnetic problem, and solving the 3D problem using Kirchhoff's equations.

Material characterization: To predict temperature distribution it is necessary to provide the simulation models with material input data. The following material properties were therefore characterized: density, specific heat capacity, the thermal conductivity tensor, and the electrical conductivity tensor (or an equivalent isotropic value of the in-plane electrical conductivity).

The density was measured based on the apparent weight of the CFRP samples when immersed in water. To measure the thermal conductivity and heat capacity on a macroscopic level, the LFA method was used. With this method it was possible to measure the thermal diffusivity in different directions of the composite on a macroscopic level, and then extract the specific heat capacity and thermal conductivity.

The electrical conductivity was characterized using different approaches. The electrical conductivity along the fibre direction was determined by measuring the resistance of fibre tows with known cross-sectional areas, using four-terminal sensing. The electrical conductivity of the composite was then calculated based on the rule of mixtures. Characterizing the electrical conductivity in the transverse-fibre direction, however, was more challenging due to the difficulty of attaching samples properly and of distinguishing between sample resistance and probe contact resistance. Instead, the through-thickness electrical conductivity, or contact resistance between crossing layers, was measured using an inductive method. Based on the coil resistance at a certain frequency, the value of the through-thickness electrical conductivity, or resistance between crossing tows, was determined by comparing the measured and simulated coil resistance at the heating frequency of interest. This approach was also used to determine an equivalent isotropic electrical conductivity in the axisymmetric model.

The temperature dependence of the electrical and thermal properties of woven CFRP was measured and used in the axisymmetric model. It is important to consider the temperature dependence of the specific heat capacity, while the room temperature value of the electrical conductivity might be used due to limited temperature influence.

Good agreement between the simulated and measured temperature distribution implies that the characterized macroscopic representations of the electrical conductivity and resistance are valid, since the induced current path, causing the power distribution, depends on the electrical conductivity tensor. The agreement of

temperature level between simulation and measurement proves that the measured specific heat capacity is reliable.

Major conclusions:

- The fibre volume fraction and the layer thickness in CFRP have a major impact on the induced power distribution. A higher fibre volume fraction and thinner layers lead to lower resistance between crossing fibre directions, making it easier to induce circulating currents, which results in more isotropic behaviour during induction heating.
- For prediction of heat generation and temperature pattern, three different simulations models were developed, using different levels of simplification. A 3D finite element model, representing the CFRP with anisotropic homogeneous layers provides a general simulation tool valid for prediction of the induced temperature pattern in both cross-ply and woven CFRP, over a wide range of fibre volume fractions, and for a wide range of layer thicknesses. For the special cases with CFRP possessing an isotropic behaviour and when an axisymmetric coil setup is used, a 2D axisymmetric finite element model based on equivalent in-plane electrical conductivity was proven to be valid, reducing the computational cost significantly compared to the 3D case. In the third model the CFRP is represented with a network of discrete resistors, solving the currents as a linear equation system based on Kirchhoff's circuit laws. The instantaneous heat generation pattern and temperature pattern on a tow size level in woven CFRP can be predicted based on the electromagnetic solution obtained from a 2D FEM model. This approach gives a more detailed prediction of the heat generation pattern in a woven CFRP, using a significantly lower number of nodes, compared to the continuum representation in the 3D FEM model. From this model it is easy to extract how much current that is going in individual tows and to understand how much of the heat that is generated in the fibres versus in the joints between fibres.
- Methods for characterizing electrical conductivity and thermal properties were identified and developed to provide the simulation models with proper material input parameters. Electrical properties were measured using both four-probe measurements and newly developed inductive methods for the non-contact measurement of electrical tensor components. For induction heating resulting in a small temperature increase, like $\Delta T_{max} \leq 30°C$ used in Paper IV, it is enough to use material parameters measured at room temperature, whereas during a larger temperature increase, it is highly beneficial to use temperature-dependent thermal properties. The relative error

increases gradually with the temperature increase and the limit for when temperature dependence is needed must be assessed for each specific case based on the requirements. However, a constant value of the electrical conductivity can be used in a wider temperature range due to the significantly weaker temperature dependence. All parameters were measured at different fibre volume fractions and regressions were extracted with respect to both the fibre volume fraction and temperature. Most notable is the strong exponential relationship between electrical conductivity in the transverse-fibre direction and the fibre volume fraction, explaining the strong relationship between the fibre volume fraction and the temperature pattern observed in simulations and via thermographic measurements.

- A study was performed to explore the possibilities of processing CFRP using the direct induction heating of carbon fibres. From this study it can be concluded that it is possible to use induction heating to cure thermoset-based CFRP. The advantages of induction heating is high potential energy efficiency and high heating rate. The most obvious challenges are the difficulty of achieving a uniform temperature distribution and of performing temperature measurements during the curing process, further emphasizing the need for reliable simulation models.

8.2 Future work

The characterization and models presented in this work are limited to a resistive representation of the contact between crossing fibres and plies. However, at high frequencies, especially in CFRP with low fibre volume fraction, the dielectric coupling and dielectric heating may be significant, and in CFRP with thermoplastic matrix, a resistive model may be very limiting. Thermoplastic composites have not been studied in this thesis, but the same models could likely be applied to them, constituting a matter that merits investigation.

The measurement and control of local temperature distribution is another matter that needs further study and development. One of the major challenges encountered during the induction heating of CFRP is to establish a uniform temperature distribution for the purpose of uniform curing. Although the relatively low electrical conductivity of CFRP enables volumetric heating due to the large skin depth, the anisotropy and the nature of induction heating make achieving uniform temperature distribution a challenge.

References

[1] Lee WI, Springer GS. Microwave Curing of Composites. Journal of Composite Materials. 1984;18(4):387-409.

[2] Thostenson ET, Chou TW. Microwave processing: fundamentals and applications. Compos Part a-Appl S. 1999;30(9):1055-71.

[3] Li N, Li Y, Hang X, Gao J. Analysis and optimization of temperature distribution in carbon fiber reinforced composite materials during microwave curing process. Journal of Materials Processing Technology. 2014;214(3):544-50.

[4] Li N, Li Y, Jelonnek J, Link G, Gao J. A new process control method for microwave curing of carbon fibre reinforced composites in aerospace applications. Composites Part B: Engineering. 2017;122:61-70.

[5] Kwak M, Robinson P, Bismarck A, Wise R. Microwave curing of carbon–epoxy composites: Penetration depth and material characterisation. Composites Part A: Applied Science and Manufacturing. 2015;75:18-27.

[6] Kim M, Sung DH, Kong K, Kim N, Kim B-J, Park HW, et al. Characterization of resistive heating and thermoelectric behavior of discontinuous carbon fiber-epoxy composites. Composites Part B: Engineering. 2016;90:37-44.

[7] Athanasopoulos N, Kostopoulos V. Resistive heating of multidirectional and unidirectional dry carbon fibre preforms. Composites Science and Technology. 2012;72(11):1273-82.

[8] Athanasopoulos N, Koutsoukis G, Vlachos D, Kostopoulos V. Temperature uniformity analysis and development of open lightweight composite molds using carbon fibers as heating elements. Composites Part B: Engineering. 2013;50:279-89.

[9] Miller AK, Chang C, Payne A, Gur M, Menzel E, Peled A. The nature of induction heating in graphite-fiber, polymer-matrix composite-materials. Sampe J. 1990;26(4):37-54.

[10] Fink BK, Mccullough RL, Gillespie JW. A local theory of heating in cross-ply carbon-fiber thermoplastic composites by magnetic induction. Polym Eng Sci. 1992;32(5):357-69.

[11] Yarlagadda S, Kim HJ, Gillespie JW, Shevchenko NB, Fink BK. A study on the induction heating of conductive fiber reinforced composites. J Compos Mater. 2002;36(4):401-21.

[12] Song MC, Moon YH. Coupled electromagnetic and thermal analysis of induction heating for the forging of marine crankshafts. Applied Thermal Engineering. 2016;98:98-109.

[13] Rudnev V, Loveless D, Cook R, Black M. Handbook of induction heating. New York: Marcel Dekker; 2003.

[14] Cernela J, Heyd B, Broyart B. Evaluation of heating performances and associated variability of domestic cooking appliances (oven-baking and pan-frying). Applied Thermal Engineering. 2014;62(2):758-65.

[15] Sanz-Serrano F, Sagues C, Llorente S. Inverse modeling of pan heating in domestic cookers. Applied Thermal Engineering. 2016;92:137-48.

[16] Yu H, Heider D, Advani S. A 3D microstructure based resistor network model for the electrical resistivity of unidirectional carbon composites. Composite Structures. 2015;134:740-9.

[17] Bayerl T, Duhovic M, Mitschang P, Bhattacharyya D. The heating of polymer composites by electromagnetic induction – A review. Composites Part A: Applied Science and Manufacturing. 2014;57:27-40.

[18] Rudolf R, Mitschang P, Neitzel M. Induction heating of continuous carbon-fibre-reinforced thermoplastics. Compos Part a-Appl S. 2000;31(11):1191-202.

[19] Becker S, Mitschang P. Influence of laminate parameters on the induction heating behavior of CFRPC. ECCM18 – 18th European Conference on Composite Materials. Athens, Greece, June, 2018.

[20] Becker S, Mitschang P. Influences of textile parameters on the induction heating behavior of CFRPC. 21st International Conference on Composite Materials. Xi'an, June, 2017.

[21] Becker S, Mitschang P. Influence of thread count of carbon twill textile-reinforced polyamide 66 laminates on the inductive heating behavior. Journal of Thermoplastic Composite Materials. 2019.

[22] Grouve W, Vruggink E, Sacchetti F, Akkerman R. Induction heating of UD C/PEKK cross-ply laminates. 23rd International Conference on Material Forming: Procedia Manufacturing; 2020.

[23] Grouve W, Sacchetti F, Vruggink EJ, Akkerman R. Simulating the induction heating of cross-ply C/PEKK laminates – sensitivity and effect of material variability. Advanced Composite Materials. 2020:1-22.

[24] Moser L. Experimental analysis and modeling of susceptorless induction welding of high performance thermoplastic polymer composites. 2012.

[25] Bettelli MA. Effect of Induction-Heat Post-Curing on Residual Stresses in Fast-Curing Carbon Fibre Reinforced Composites: Luleå University of Technology; 2020.

[26] Frauenhofer M, Kunz H, Dilger K. Fast Curing of Adhesives in the Field of CFRP. J Adhesion. 2012;88(4-6):406-17.

[27] The Induction Heating Process [cited 2021-12-21]; Available from: https://www.comsol.com/multiphysics/induction-heating.

[28] Siesing L, Lundström F, Frogner K, Cedell T, Andersson M. Towards energy efficient heating in industrial processes - Three steps to achieve maximized efficiency in an induction heating system. Procedia Manufacturing. 2018;25(Proceedings of the 8th Swedish Production Symposium (SPS 2018)):404-11.

[29] Lundström F, Frogner K, Wiberg O, Cedell T, Andersson M. Induction heating of carbon fiber composites: Investigation of electrical and thermal properties. International Journal of Applied Electromagnetics and Mechanics. 2017;53:S21-S30.

[30] Lundström F, Frogner K, Andersson M. A numerical model to analyse the temperature distribution in cross-ply CFRP during induction heating. Composites Part B: Engineering. 2020;202.

[31] Lundström F, Frogner K, Andersson M. Analysis of the temperature distribution in weave-based CFRP during induction heating using a simplified numerical model with a cross-ply representation. Composites Part B: Engineering. 2021;223.

[32] Lundström F, Frogner K, Andersson M. A method for inductive measurement of equivalent electrical conductivity in thin non-consolidated multilayer carbon fibre fabrics. Composites Part B: Engineering. 2018;140:204-13.

[33] Lundström F, Frogner K, Andersson M. Numerical modelling of CFRP induction heating using temperature-dependent material properties. Composites Part B: Engineering. 2021;220.

[34] Meeker D. Finite Element Method Magnetics; Available from: https://www.femm.info/wiki/HomePage.

[35] Wasselynck G, Trichet D, Ramdane B, Fouldagar J. Interaction Between Electromagnetic Field and CFRP Materials: A New Multiscale Homogenization Approach. IEEE T Magn. 2010;46(8):3277-80.

[36] Al-Arabi M, El-Riedy M. Natural convection heat transfer from isothermal horizontal plates of different shapes. International Journal of Heat and Mass Transfer. 1976;19(12):1399-404.

[37] Khalifa A-JN. Natural convective heat transfer coefficient – a review I. Isolated vertical and horizontal surfaces. Energy Conversion and Management. 2001;42(4):491-504.

[38] Khalifa A-JN. Natural convective heat transfer coefficient – a review II. Surfaces in two- and three-dimensional enclosures. Energy Conversion and Management. 2001;42(4):505-17.

[39] Becker S, Michel M, Mitschang P, Duhovic M. Influence of polymer matrix on the induction heating behavior of CFRPC laminates. Composites Part B: Engineering. 2022;231.

[40] Fu T, Xu J, Hui Z. Analysis of Induction Heating Temperature Field of Plain Weave CFRP Based on Finite Element Meso Model. Applied Composite Materials. 2021.

[41] Grafil Inc, Pyrofil TR50S 12K, 2008.

[42] Hexcel Corporation, HexTow AS4 Carbon Fiber Product data sheet, 2020.

[43] Toray Carbon Fibers America Inc. Torayca T700S Data sheet No. CFA-005.

[44] Mizukami K, Watanabe Y. A simple inverse analysis method for eddy current-based measurement of through-thickness conductivity of carbon fiber composites. Polym Test. 2018;69:320-4.

[45] Acero J, Alonso R, Burdio JM, Barragan LA, Carretero C. A model of losses in twisted-multistranded wires for planar windings used in domestic induction heating appliances. Appl Power Elect Co. 2007:1247-53.

[46] Acero J, Alonso R, Burdio JM, Barragan LA, Puyal D. Frequency-Dependent Resistance in Litz-Wire Planar Windings for Domestic Induction Heating Appliances. IEEE Transactions on Power Electronics. 2006;21(4):856-66.

[47] Xu X, Ji H, Qiu J, Cheng J, Wu Y, Takagi T. Interlaminar contact resistivity and its influence on eddy currents in carbon fiber reinforced polymer laminates. NDT & E International. 2018;94:79-91.

[48] Bouloudenine A, Feliachi M, Latreche MEH. Development of circular arrayed eddy current sensor for detecting fibers orientation and in-plane fiber waviness in unidirectional CFRP. NDT & E International. 2017;92:30-7.

[49] Naidjate M, Helifa B, Feliachi M, Lefkaier IK, Heuer H, Schulze M. A Smart Eddy Current Sensor Dedicated to the Nondestructive Evaluation of Carbon Fibers Reinforced Polymers. Sensors (Basel). 2017;17(9).

[50] Senghor FD, Wasselynck G, Bui HK, Branchu S, Trichet D, Berthiau G. Electrical conductivity tensor modeling of stratified woven-fabric carbon fiber reinforced polymer composite materials. Ieee Transactions on Magnetics. 2017;53(6).

[51] Parker WJ, Jenkins RJ, Butler CP, Abbott GL. Flash Method of Determining Thermal Diffusivity, Heat Capacity, and Thermal Conductivity. J Applied Phys. 1961;32(9):1679-84.

[52] The Induction Heating Process [cited 2021-12-01]; Available from: https://www.netzsch-thermal-analysis.com/en/contract-testing/methods/laser-flash-technique-lfa/.

[53] Joven R, Minaie B. Thermal properties of autoclave and out-of-autoclave carbon fiber-epoxy composites with different fiber weave configurations. J Composite Mat. 2018;52(29):4075-85.

[54] Rolfes R, Hammerschmidt U. Transverse thermal conductivity of CFRP laminates: A numerical and experimental validation of approximation formulae. Composites Science and Technology. 1995(54):45-54.

[55] Pietrak K, Wisniewski TS. A review of models for effective thermal conductivity of composite materials. J Power Technol. 2015;95(1):14-24.

[56] Bard S, Schonl F, Demleitner M, Altstadt V. Influence of Fiber Volume Content on Thermal Conductivity in Transverse and Fiber Direction of Carbon Fiber-Reinforced Epoxy Laminates. Materials (Basel). 2019;12(7).

[57] Zhang H, Wu K, Xiao G, Du Y, Tang G. Experimental study of the anisotropic thermal conductivity of 2D carbon-fiber/epoxy woven composites. Composite Structures. 2021;267.

[58] Toray Group, Delta tech DT140RS, Matrix DS - Data sheet, May 2019.

[59] Toray Carbon Fibers America Inc, Torayca T300 Data sheet No. CFA-001.

[60] Schaal L. RocTool launches an innovative composites process: Light Induction Tooling. Reinforced Plastics. 2017;61(3):173-5.

Printed by Media-Tryck, Lund 2022 NORDIC SWAN ECOLABEL 3041 0903

Faculty of Engineering
Department of Mechanical Engineering Sciences
Division of Production and Materials Engineering

ISBN 978-91-8039-199-3